



**NATIONAL TECHNICAL UNIVERSITY OF ATHENS**

School of Applied Mathematical & Physical Sciences



Conseil Européen pour la Recherche Nucléaire



CompactLight Project

# Space charge studies for the CompactLight Project & Radiation Studies in the CHARM facility

DIPLOMA THESIS  
OF

RAFAELLA ELENI KOTITSA

*Supervisor professor:*  
Prof. Evangelos Gazis,  
NTUA

*Supervisor researcher of Part I:*  
Dr. Andrea Latina, CERN

*Supervisor researcher of Part II:*  
Dr. Robert Froeschl, CERN





**ΕΘΝΙΚΟ ΜΕΤΣΟΒΙΟ ΠΟΛΥΤΕΧΝΕΙΟ**  
Σχολή Εφαρμοσμένων Μαθηματικών και Φυσικών  
Επιστημών



Conseil Européen pour la Recherche Nucléaire



CompactLight Project

Μελέτες χωρικού φορτίου για το CompactLight  
Project & Μελέτες ακτινοβολίας στην εγκατάσταση  
CHARM

ΔΙΠΛΩΜΑΤΙΚΗ ΕΡΓΑΣΙΑ  
ΤΗΣ

ΡΑΦΑΕΛΛΑ ΕΛΕΝΗ ΚΟΤΙΤΣΑ

Επιβλέπων:  
Ευάγγελος Γαζής, Ε.Μ.Π.

Υπεύθυνος Ερευνητής του Μέρους I  
Dr. Andrea Latina, CERN

Υπεύθυνος Ερευνητής του Μέρους II:  
Dr. Robert Froeschl, CERN







**ΕΘΝΙΚΟ ΜΕΤΣΟΒΙΟ ΠΟΛΥΤΕΧΝΕΙΟ**  
Σχολή Εφαρμοσμένων Μαθηματικών και Φυσικών  
Επιστημών

**Μελέτες χωρικού φορτίου για το CompactLight  
Project & Μελέτες ακτινοβολίας στην εγκατάσταση  
CHARM**

**ΔΙΠΛΩΜΑΤΙΚΗ ΕΡΓΑΣΙΑ  
ΤΗΣ**

**ΡΑΦΑΕΛΛΑ ΕΛΕΝΗ ΚΟΤΙΤΣΑ**

*Επιβλέπων:*  
Ευάγγελος Γαζής, Ε.Μ.Π.

*Υπεύθυνος Ερευνητής του Μέρους I*  
*Dr. Andrea Latina, CERN*

*Υπεύθυνος Ερευνητής του Μέρους II:*  
*Dr. Robert Froeschl, CERN*

**ΤΡΙΜΕΛΗΣ ΕΠΙΤΡΟΠΗ**

.....  
Ευάγγελος Γαζής,  
Καθηγητής Ε.Μ.Π.

(Evangelos Gazis,  
Professor NTUA)

.....  
Σταύρος Μαλτέζος,  
Καθηγητής Ε.Μ.Π.

(Stavros Maltezos,  
Professor NTUA)

.....  
Θεόδωρος Αλεξόπουλος,  
Καθηγητής Ε.Μ.Π.

(Theodoros Alexopoulos,  
Professor NTUA)



# Introduction

## PART I

CompactLight is a project in which take part 24 institutes (21 European +3 extra Europeans), gathering the world-leading experts both in the domains of X-band acceleration and undulator design. More specifically, *H2020 CompactLight* Project aims at designing the next generation of compact hard X-Rays Free-Electron Lasers, relying on very high accelerating gradients and on novel undulator concepts. In the framework of that project I performed bench-marking of space charge forces between the RF-Track software against ASTRA. This included the implementations of analytical forms in Octave as well.

## PART II

The CERN High energy AcceleRator Mixed field (CHARM) facility has been constructed in 2014 in the CERN East Experimental Area to study radiation effects on electronic components. It receives a primary proton beam from the CERN Proton Synchrotron at a beam momentum of  $24\text{GeV}/c$  and a maximum average beam intensity of  $6.7E10$  *protons/second* with a maximum pulse intensity of  $5E11$  *protons/pulse* and a respective pulse length of  $350\text{ms}$ . The beam impinges on one out of a set of dedicated targets to produce the desired radiation fields at several experimental positions. The beam operation of the CHARM facility leads to activation of the facility itself, including the targets, walls, floors and other support structures. The correct prediction of the residual ambient dose equivalent rates is important for the optimization of the design of such a facility as well as for the

---

planning of accesses to the facility. The fact that the facility configuration during beam operation is different in the CHARM facility compared to the facility configuration during access, e.g. the irradiated targets are moved to a dedicated alcove that is closed during access, makes this prediction even more challenging for the CHARM facility. A dedicated residual ambient dose equivalent rate measurement campaign with several mobile devices as well as permanently installed devices has been performed at the end of the 2015 beam period in the CHARM facility starting from 1 hour after beam stop collecting data for 1 week. These data are compared to predictions for the residual ambient dose equivalent rates in the CHARM facility performed with the FLUKA Monte Carlo code, coupled to the DORIAN code for the various facility configurations, as a function of the cool-down time taking the operational parameters of the CHARM facility in 2015 into account. This includes the characteristics of the beam delivered to the CHARM facility as well as the CHARM target settings.

# Εισαγωγή

## ΜΕΡΟΣ Ι

Το *CompactLight* είναι ένα έργο στο οποίο συμμετέχουν 24 ιδρύματα, συγκεντρώνοντας τους κορυφαίους εμπειρογνώμονες στον κόσμο τόσο στους τομείς των *X – band acceleration* όσο και του σχεδιασμού των *undulator*. Πιο συγκεκριμένα, το H2020 CompactLight Project στοχεύει στο σχεδιασμό της επόμενης γενιάς compact hard X-Rays Free-Electron. Τις τελευταίες δεκαετίες οι εγκαταστάσεις ακτινοβολίας Synchrotron έχουν δει μια ορμή ανάπτυξη ως θεμελιώδες εργαλείο για τη μελέτη υλικών σε ένα ευρύ φάσμα επιστημών, τεχνολογιών και εφαρμογών. Η τελευταία γενιά πηγών φωτός, τα λέιζερ Free Electron, είναι ικανά να παρέχουν υψηλής έντασης φωτονικές ακτίνες πρωτοφανούς λαμπρότητας και ποιότητας, παρέχουν έναν ουσιαστικά νέο τρόπο ανίχνευσης της ύλης και έχουν πολύ υψηλές, σε μεγάλο βαθμό ανεξερεύνητες δυνατότητες για την επιστήμη και την καινοτομία. Επί του παρόντος, τα *FEL* που λειτουργούν στην ΕΕ είναι πέντε: Τα *FERMI*, *FLASH* και *FLASHII*, και τα *SwissFEL* και *EuroXFEL* που άρχισαν να λειτουργούν πρόσφατα. Ενώ τα περισσότερα από τα παγκόσμια υπάρχοντα *FEL* χρησιμοποιούν συμβατικές κανονικές αγωγές *Sband 3GHz*, άλλοι χρησιμοποιούν νεότερα σχέδια με βάση την τεχνολογία *C – band 6GHz*, αυξάνοντας την επιταχυνόμενη κλίση με συνολική μείωση του μήκους και του κόστους *linac*. Στα πλαίσια λοιπόν αυτού του προγράμματος, έγινε σύγκριση των δυνάμεων χωρικού φορτίου μεταξύ του λογισμικού *RF – Track* ενάντια στην *ASTRA*. Αυτό περιελάμβανε τις υλοποιήσεις αναλυτικών μορφών στην *Octave*. Οι δυνάμεις του χωρικού φορτίου είναι οι δυνάμεις αλληλεπίδρασης μεταξύ των σωματιδίων της δέσμης. Αυτές οι

---

εσωτερικές δυνάμεις συχνά παραμελούνται στους υπολογισμούς. Ωστόσο, για μια καλύτερη μοντελοποίηση της εξέλιξης της δέσμης στον επιταχυντή, αυτές οι δυνάμεις πρέπει να ληφθούν υπόψη. Το λογισμικό *RF – Track* αποδείχτηκε να είναι ένα ισχυρό εργαλείο για τέτοιου είδους υπολογισμούς.

## ΜΕΡΟΣ II

Η εγκατάσταση του (CHARM) CERN High Energy Accelerator κατασκευάστηκε το 2014 στην *EastArea* του *CERN* για τη μελέτη των επιδράσεων της ακτινοβολίας σε ηλεκτρονικά εξαρτήματα. Λαμβάνει μια πρωτεύουσα δέσμη πρωτονίων από το CERN Proton Synchrotron. Η δέσμη προσκρούει σε ένα σύνολο ειδικών στόχων για την παραγωγή των επιθυμητών πεδίων ακτινοβολίας σε διάφορες πειραματικές θέσεις. Η λειτουργία δέσμης της εγκατάστασης *CHARM* οδηγεί σε ενεργοποίηση της ίδιας της εγκατάστασης, συμπεριλαμβανομένων των στόχων, των τοίχων, των δαπέδων και άλλων δομών στήριξης. Η σωστή πρόβλεψη των residual ambient dose equivalent rate είναι σημαντική για τη βελτιστοποίηση του σχεδιασμού μιας τέτοιας εγκατάστασης καθώς και για τον προγραμματισμό των εισόδων στην εγκατάσταση. Μια ειδική καμπάνια μέτρησης των residual ambient dose equivalent rate με αρκετές κινητές συσκευές καθώς και μόνιμα εγκατεστημένες συσκευές έχει εκτελεστεί στο τέλος της περιόδου δέσμης του 2015 στην εγκατάσταση *CHARM* ξεκινώντας από 1 ώρα μετά τη διακοπή της συλλογής δεδομένων για 1 την εβδομάδα από τη δέσμη. Αυτά τα δεδομένα συγκρίνονται με προβλέψεις για τις υπόλοιπες μετρήσεις των residual ambient dose equivalent rate στην εγκατάσταση *CHARM* που εκτελούνται με το πρόγραμμα FLUKA Monte Carlo, σε συνδυασμό με τον κωδικό *DORIAN* για τις διάφορες διαμορφώσεις της εγκατάστασης, ως συνάρτηση του χρόνου ψύξης λαμβάνοντας τις λειτουργικές παραμέτρους του *CHARM* το 2015. Αυτό περιλαμβάνει τα χαρακτηριστικά της δέσμης που παραδίδεται στην εγκατάσταση *CHARM* καθώς και τις ρυθμίσεις στόχου *CHARM*.

# Acknowledgements

This thesis wouldn't be possible without the contribution of my supervisors Dr. Robert Froeschl and Dr. Andrea Latina.

I am deeply thankful to my supervisor Dr. Robert Froeschl for giving me the opportunity to join CERN, and for his continuous guidance and support throughout my technical internship and my time at CERN.

I would like also to express my gratitude to my supervisor Dr. Andrea Latina, for his support, his willingness to guide and motivate me, his teachings and for his useful suggestions throughout the work we have done. They are both great scientists, kind people and exceptional mentors.

Moreover I want to thank my professor Evangelos Gazis for his valuable advises, his help and support whenever needed.

The list of people that I should mention at CERN is too long for just one page, therefore I have to limit myself to say thank you for the endless professional and personal conversations we had and the numerous pleasant moments we shared. Furthermore, I owe special thanks to all my friends in Greece who supported me despite the distance and their thoughts were always with me. I am deeply grateful to Nodas for his advice and encouragement all this time and for always being there for me.

Last but not least, a special acknowledgement should be addressed to my family. I thank my father George, my mother Andri and my siblings Sotiris and Panagiota who guided me with love during my education and my life, encouraging me to pursue my interests.





# PART I



# Contents

<b>1</b>	<b>CompactLight Project</b>	<b>5</b>
1.1	Project Overview . . . . .	7
1.1.1	CompactLight Objectives . . . . .	7
1.1.2	Concepts and Approach . . . . .	7
1.2	FEL Performance and Accelerator Layout . . . . .	9
<b>2</b>	<b>Accelerators &amp; beam physics</b>	<b>13</b>
2.1	Accelerators . . . . .	13
2.2	Space-charge forces . . . . .	17
2.2.1	EM equations . . . . .	17
2.2.2	Coulomb's law . . . . .	18
2.2.3	The Dirac delta function. . . . .	20
2.2.4	Gauss's Law . . . . .	20
2.3	Charged particle motion . . . . .	23
2.3.1	Lorentz force . . . . .	23
2.4	Equations of motion . . . . .	24
2.5	Relativity . . . . .	27
2.6	Codes: RF-Track, ASTRA . . . . .	29
2.6.1	RF-Track . . . . .	29
2.6.2	Bunch6d . . . . .	30
2.6.3	Bunch6dT . . . . .	30
2.6.4	ASTRA . . . . .	32

---

<b>3</b>	<b>Numerical implementation</b>	<b>33</b>
3.1	Particle-to-Particle force . . . . .	33
3.2	Particle in cell and FFT . . . . .	34
3.3	Particle-in-cell (FFT) approach . . . . .	35
3.3.1	The Green's function for the Laplacian . . . . .	38
3.3.2	FFT and Green's function . . . . .	39
3.3.3	FFT Mesh . . . . .	40
<b>4</b>	<b>Case Studies</b>	<b>45</b>
4.1	Uniformly charged sphere . . . . .	45
4.2	Cylindrical distribution . . . . .	53
<b>5</b>	<b>Conclusions</b>	<b>61</b>

# Chapter 1

## CompactLight Project

CompactLight is a project in which take part 24 institutes (21 European +3 extra Europeans), gathering the world-leading experts both in the domains of X-band acceleration and undulator design. More specifically, *H2020* CompactLight Project aims at designing the next generation of compact hard X-Rays Free-Electron Lasers, relying on very high accelerating gradients and on novel undulator concepts. During the past decades Synchrotron Radiation facilities have seen an impetuous growth as a fundamental tool for the study of materials in a wide spectrum of sciences, technologies, and applications. The latest generation of light sources, the Free Electron Lasers, capable of delivering high-intensity photon beams of unprecedented brilliance and quality, provide a substantially novel way to probe matter and have very high, largely unexplored, potential for science and innovation. Currently, the FELs operating in EU are five: FERMI, FLASH and FLASH II are operating in the soft X-ray range, SwissFEL and EuroXFEL are hard X-ray FELs that started operation recently. While most of the worldwide existing FELs use conventional normal conducting 3 GHz S-band linacs, others use newer designs based on 6 GHz C-band technology, increasing the accelerating gradient with an overall reduction of the linac length and cost. [12]

CompactLight intends to design a compact Hard X-ray FEL facility based on very high-gradient acceleration in the X band of frequencies, on a very

## 1. CompactLight Project

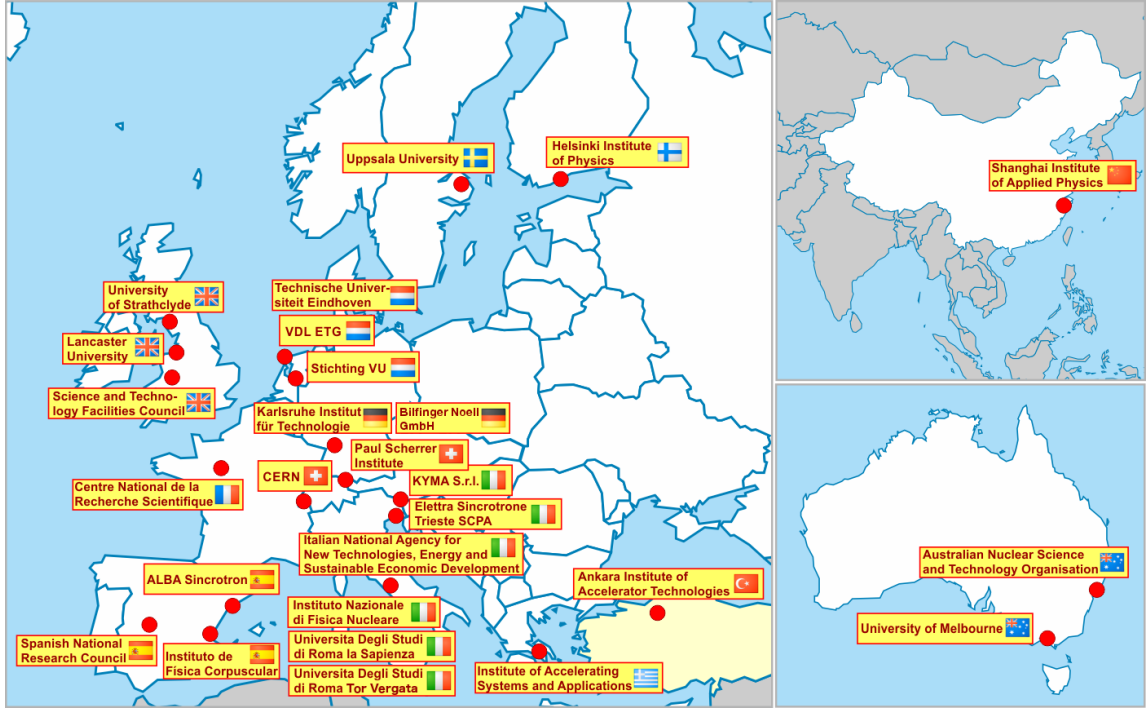


**Figure 1.1:** The participants of the CompactLight project

bright photoinjector, and on short-period/superconductive undulators to enable smaller electron beam energy. If compared to existing facilities, the proposed facility will benefit from a lower electron beam energy, due to the enhanced undulators performance, be significantly more compact, as a consequence both of the lower energy and of the high-gradient X-band structures, have lower electrical power demand and a smaller footprint.

The goal of the project is to disseminate X-band technology as a new standard for accelerator-based facilities and advance undulators to the next generation of compact photon sources, with the aim of facilitating the widespread development of X-ray FEL facilities across and beyond Europe by making them more affordable to build and to operate.

## 1.1 Project Overview

### 1.1.1 CompactLight Objectives

The key objective of the CompactLight Design Study is to demonstrate, through a conceptual design, the feasibility of an innovative, compact and cost effective FEL facility suited for user demands identified in the science case. In order to achieve this, the high-level objectives are to specify the user demands and design parameters for a compact and cost effective FEL driven hard X-ray facility, to advance innovative designs for X-band and undulator technology as new standards for accelerator based compact photon sources and to present a flexible design that can be adapted to local implementation demands with photon source options for soft and hard X-rays as well as Compton light.

### 1.1.2 Concepts and Approach

The overall concept underlying this proposal is to bring together recent advances in many of the important technical systems which make up an XFEL injector, linac and undulator to produce the design of a next-generation facility with significantly lower cost and size than existing facilities. The goal is to make XFELs feasible for smaller countries, regions and universities. There are a number of new (and imminent) XFEL facilities around the world including the superconducting European XFEL, FLASH and LCLS-2 and the normal conducting SACLA, the PAL-XFEL and the SwissFEL as well as older facilities such as the LCLS and FERMI. All of these facilities have designs that were fixed, and technological choices made, at least five years ago and in some case many more. In the intervening period there has been intense electron-accelerator development driven by the XFEL community itself, the linear-collider community as well as by other applications such as Compton scattering sources. Relevant advances include the lower emittance and higher repetition-rate photo-injectors, high-gradient

linacs (gradients in excess of 100 MV/m are now routinely achieved), high-efficiency klystrons, advanced concept undulators, improved diagnostics including X-band deflectors for longitudinal bunch dynamics, better beam dynamics and optimization tools including those developed for linear colliders. The belief of the members of the CompactLight project is that these developments, will allow to design a facility with significantly lower cost and size than existing facilities. [\[12\]](#)



## 1.2 FEL Performance and Accelerator Layout

Based on user-driven scientific requirements, the CompactLight collaboration has determined the ideal wavelength range, beam structure, pulse duration, synchronisation to external laser, pulse energy, polarisation, etc., that should be achieved by an X-band-driven hard X-ray FEL. The resulting design includes also options for soft X-ray operation, external seeding schemes to produce longitudinally coherent x-ray pulses, and double pulse operation for FEL-pump FEL-probe experiments.

The proposed FEL features great flexibility in order to satisfy the variety of user requirements. The FEL tuning range is achieved by operating the machine in different modes at each of the three presented scenarios. The common features of the three configurations are the twin bunches from the photo-injector sitting in near-consecutive RF buckets, separated by hundred's of ps, for the simultaneous operation of two FEL lines, thus driving either FEL-pump FEL probe experiments at a single end-station, or experiments at two distinct end-stations. Moreover the acceleration in X-band linacs and double magnetic bunch length compression, the emission of soft x-rays from a low energy ( $< 2\text{GeV}$ ) electron beam at high repetition rate, either 250 Hz or 1 kHz, and emission of hard x-rays from high energy ( $> 2.8\text{GeV}$ ) electron beam at low repetition rate (100Hz) and the temporal separation of the two FEL pulses goes from perfect synchronization to  $\pm 100$  fs, at the end-station.

The baseline layout is able to generate two synchronized either soft or hard x-ray photon pulses in Self-Amplified Spontaneous Emission (SASE) mode. The soft x-rays are emitted at 250 Hz repetition rate. Upgrade-1 increases the soft x-rays repetition rate to 1 kHz by virtue of additional klystron power supplying the accelerating structures, in order to keep the average RF power in the structures constant. Upgrade-2 adds two features to Upgrade-1. The soft x-rays can be produced in Echo-Enabled Harmonic Generation (EEHG) mode providing full longitudinal coherence, and hard x-rays

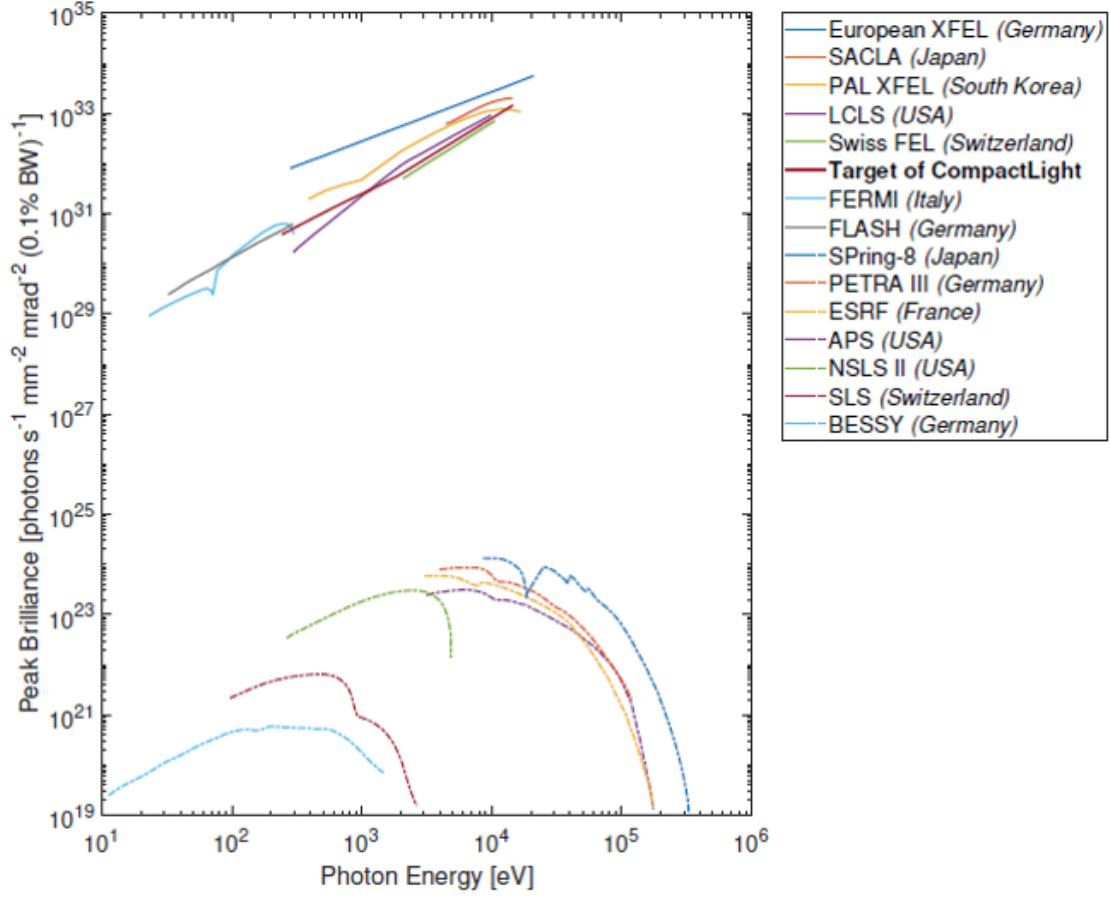


**Figure 1.2:** The peak photon brightness targeted by CompactLight in the framework of the present short-wavelength FEL facilities.

in self-seeding mode for much-improved longitudinal coherence compared to SASE and the soft and hard x-ray pulses can be produced simultaneously and transmitted at the sampling rate of 100 Hz to the same end-station for FEL-pump FEL-probe experiments which implies both soft and hard x-rays can be transported to laser same stations as requested by users. [12] In the frame of being part of the CompactLight Project I was tasked Benchmarking of space charge forces between RF-Track software against ASTRA. Implementation of the same calculations for the analytical model, in Octave to serve as reference (i.e. calculation of the electric field with the green function). For this validation of the space charge algorithm, the comparisons

<b>Parameter</b>	<b>Unit</b>	<b>Soft X-ray</b>	<b>Hard X-ray</b>
Max. repetition rate	kHz	1	0.1
Photon energy	keV	0.25 – 2.0	2.0 – 16.0
Wavelength	nm	5.0 – 0.6	0.6 – 0.08
FEL tuning range at fixed energy		$\times 2$	$\times 2$
Peak brilliance @16 keV	(*)	$10^{31}$	$10^{33}$
Pulse duration	fs	0.1 – 50	1 – 50
Polarization		variable, selectable	
Two-pulse delay	fs	$\pm 100$	$\pm 100$
Two-colour separation	%	20	10
Synchronization	fs	$< 10$	$< 10$

**Figure 1.3:** The user requirements for CompactLight have been established by interacting with existing and potential FEL users in a variety of formats. All of these inputs into a comprehensive photon output specifications, summarised in the following table

have been done for cylindrical and spherical distributions.

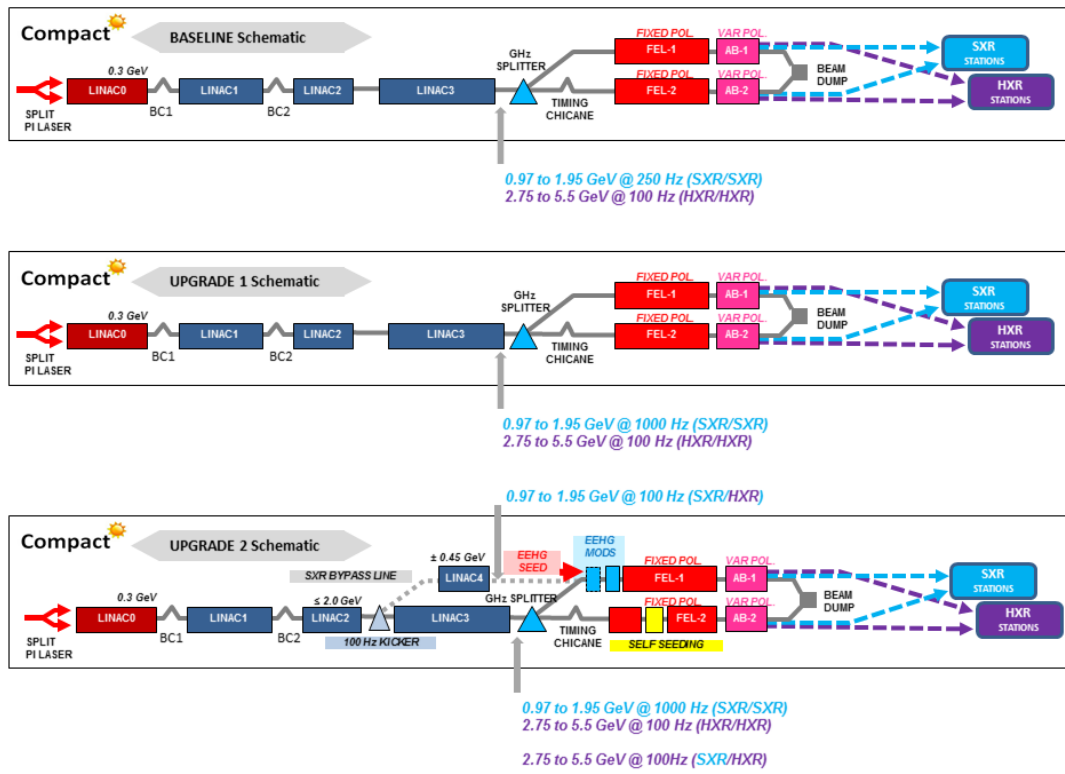


**Figure 1.4:** The facility baseline layout and its foreseen two upgrade stages.

# Chapter 2

## A quick introduction to accelerators and beam physics

### 2.1 Accelerators

Accelerators were invented in the 1930s, in order to provide energetic particles to investigate the structure of the atomic nucleus, investigating until now many aspects of particle physics. They speed up and increase the energy of a beam of particles by generating electric fields that accelerate the particles, and magnetic fields that steer and focus them. An accelerator comes either in the form of a ring (a circular accelerator), where a beam of particles travels repeatedly round a loop, or in a straight line (a linear accelerator), where the particle beam travels from one end to the other. At CERN a number of accelerators are joined together in sequence to reach successively higher energies. Particle accelerators use electric fields to speed up and increase the energy of a beam of particles, which are steered and focused by magnetic fields. The particle source provides the particles, such as protons or electrons, that are to be accelerated. The beam of particles travels inside a vacuum in the metal beam pipe. The vacuum is crucial to maintaining an air and dust free environment for the beam of particles to travel unobstructed. Electromagnets steer and focus the beam of particles

while it travels through the vacuum tube. Electric fields spaced around the

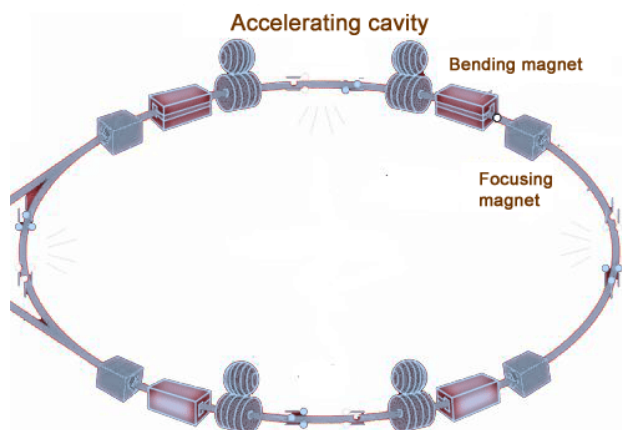


**Figure 2.1:** An example of a circular accelerator.

accelerator switch from positive to negative at a given frequency, creating radio waves that accelerate particles in bunches. Particles can be directed at a fixed target, such as a thin piece of metal foil, or two beams of particles can be collided. Particle detectors record and reveal the particles and radiation that are produced by the collision between a beam of particles and the target. Accelerators at CERN boost particles to high energies before they are

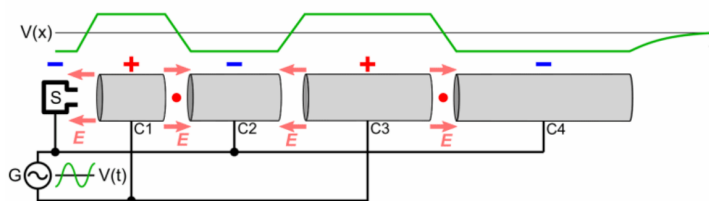


**Figure 2.2:** An example of a linear accelerator.

made to collide inside detectors. The detectors determine the identity of particles, by characterizing their speed, mass and charge. This process requires accelerators, powerful electromagnets, and layer upon layer of complex sub-detectors. Particles that are produced in collisions normally travel in straight lines, but applying magnetic field their paths become curved. Electromagnets around particle detectors generate magnetic fields to make this effect

happen. Through this procedure we can calculate the momentum of from the curvature of its path. At CERN in LHC, there are thousands of lattice magnets that bend and tighten the particles trajectory. They are responsible for keeping the beams stable and precisely aligned. Dipole magnets are one of the most complex parts of the LHC. These magnets used to bend the paths of the particles. There are 1232 main dipoles, each 15 meters long and weighing 35 tons. Powerful magnetic fields generated by the dipole magnets allow the beam to handle tighter turns. When particles are bunched together, they are more likely to collide in greater numbers when they reach the LHC detectors. Quadrupoles help to keep the particles in a tight beam. They have four magnetic poles arranged symmetrically around the beam pipe to squeeze the beam either vertically or horizontally. In addition there are sextupole, octupole and decapole magnets, which correct for small imperfections in the magnetic field at the extremities of the dipoles. After the beams collide in the detector, enormous magnets aid the measurement of particles. Other magnets minimize the spread of the particles from the collisions. When it is time to dispose of the particles, they are deflected from the LHC along a straight line towards the two beam dumps. A “dilution” magnet reduces the beam intensity by a factor of 100'000 before the beam collides with a block of concrete and graphite composite for its final stop. Insertion magnets are also responsible for beam cleaning, which ensures that stray particles do not come in contact with the LHC's most sensitive components. Luminosity is an important indicator of the performance of an accelerator. The higher the luminosity, the more data the experiments can gather to allow them to observe rare processes. It gives a measure of how many collisions are happening in a particle accelerator. To accelerate particles, the accelerators are fitted with metallic chambers containing an electromagnetic field known as radiofrequency (RF) cavities. Charged particles injected into this field receive an electrical impulse that accelerates them. During this process the physics is complex and in order to understand better the beam dynamics in the accelerators we use computer models. In this thesis we elaborate these

models.

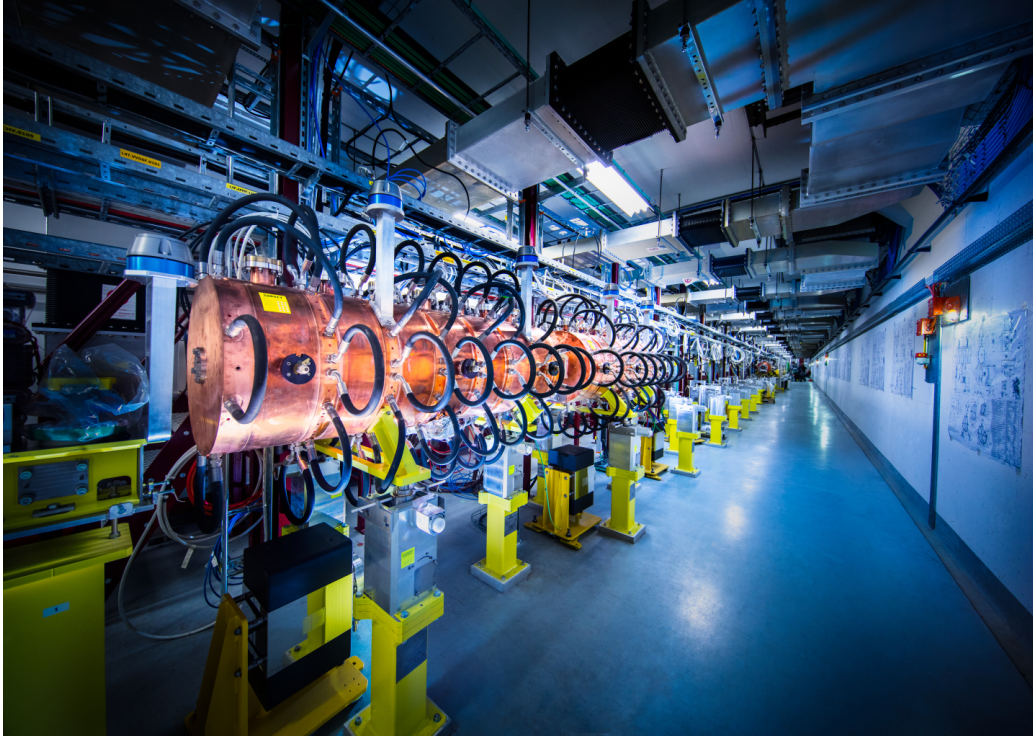


**Figure 2.3:** The linear accelerator, Linac 4 is the newest accelerator to join CERN's complex (Image: Andrew Hara/CERN)



## 2.2 Space-charge forces

### 2.2.1 EM equations

#### Maxwell Equations in Vacuum, Fields, and Sources

As a first step, in this chapter we will be referred to the Maxwell equations. These equations provide a mathematical model for describing how electric and magnetic fields are generated by charges, currents, and changes of the fields. The Maxwell equations are

$$\nabla \cdot \mathbf{D} = \rho \quad (2.1)$$

$$\nabla \times \mathbf{H} - \frac{\partial \mathbf{D}}{\partial t} = \mathbf{J} \quad (2.2)$$

$$\nabla \times \mathbf{E} - \frac{\partial \mathbf{B}}{\partial t} = 0 \quad (2.3)$$

$$\nabla \cdot \mathbf{B} = 0 \quad (2.4)$$

where for external sources in vacuum  $\mathbf{D} = \epsilon_0 \mathbf{E}$  and  $\mathbf{B} = \mu_0 \mathbf{H}$

$$\nabla \cdot \mathbf{E} = \frac{\rho}{\epsilon_0} \quad (2.5)$$

$$\nabla \times \mathbf{B} - \frac{\partial \mathbf{E}}{c^2 \partial t} = \mu_0 \mathbf{J} \quad (2.6)$$

Implicit in the Maxwell equations is the continuity equation for the charge density and current density,

$$\frac{\partial \rho}{\partial t} + \nabla \cdot \mathbf{J} = 0 \quad (2.7)$$

Furthermore essential for the motion of a charged particle is the Lorentz force equation below. This equation gives the force acting on a point charge  $q$  in

the presence of electromagnetic fields

$$\mathbf{F} = q(\mathbf{E} + \nu \times \mathbf{B}) \quad (2.8)$$

All these equations above have been written in SI units. Furthermore important for electrodynamics is the speed of light in vacuum,  $c$ . The electric and magnetic fields  $\mathbf{E}$  and  $\mathbf{B}$  were introduced in the equation of the Lorentz force.

### 2.2.2 Coulomb's law

Coulomb's law states that the electrostatic force  $\mathbf{F}_1$  experienced by a charge,  $q_1$  at position  $\mathbf{r}_1$ , in the vicinity of another charge,  $q_2$  at position  $\mathbf{r}_2$ , in a vacuum is equal to:

$$\mathbf{F}_1 = \frac{q_1 q_2}{4\pi\epsilon_0} \frac{\mathbf{r}_1 - \mathbf{r}_2}{|\mathbf{r}_1 - \mathbf{r}_2|^3} = \frac{q_1 q_2}{4\pi\epsilon_0} \frac{\hat{\mathbf{r}}_{12}}{|\mathbf{r}_{12}|^2} \quad (2.9)$$

where  $r_{12} = r_1 - r_2$ , the unit vector  $\hat{\mathbf{r}}_{12} = \frac{\mathbf{r}_{12}}{|\mathbf{r}_{12}|}$ . Coulomb, showed experimentally that the force between two small charged bodies separated in air a distance large compared to their dimensions, varied directly as the magnitude of each charge, varies inversely as the square of the distance between them, is directed along the line joining the charges and is attractive if the bodies have the same type of charge. Moreover it was shown experimentally that the total force produced on one small charged bodies placed around it is the vector sum of the individual two-body forces of Coulomb.

### Electric field

The electric field can be defined as the force per unit charge acting at a given point. It is a vector function of position, denoted by  $\mathbf{E}$ . Experimentally, the ratio and the direction of the force will become constant as the amount of test charge is made smaller and smaller. This limiting values of magnitude and direction define the magnitude and direction of the electric field  $\mathbf{E}$  at

the point in question. This can be expressed by the equation below

$$\mathbf{F} = q\mathbf{E} \quad (2.10)$$

where  $\mathbf{F}$  is the force,  $\mathbf{E}$  the electric field and  $q$  the charge. In this equation we assumed that the charge  $q$  is located at a point, and the force and the electric field are evaluated at that point. Now let's write Coulomb's law with a similar way. If  $\mathbf{F}$  is the force on a point charge  $q_1$ , that is located at  $\mathbf{x}_1$ , due to another point charge  $q_2$  at the point  $\mathbf{x}_2$  can be obtained directly:

$$\mathbf{F} = kq_1q_2 \frac{\mathbf{x}_1 - \mathbf{x}_2}{|\mathbf{x}_1 - \mathbf{x}_2|^3} \quad (2.11)$$

$q_1$  and  $q_2$  are algebraic quantities, which can be both positive and negative. The constant of proportionality  $k$  depends on the system of units used. The electric field at the point  $\mathbf{x}$  due to a point charge  $q_1$  at the point  $\mathbf{x}_1$  can be obtained directly by

$$\mathbf{E}(\mathbf{x}) = kq_1 \frac{\mathbf{x} - \mathbf{x}_1}{|\mathbf{x} - \mathbf{x}_1|^3} \quad (2.12)$$

The constant  $k$  differs in different systems of units. In electrostatic units (esu),  $k = 1$  and unit charge is chosen as that charge that exerts a force of one dyne on an equal point charge located one centimeter away. The esu unit of charge is called statcoulomb, and the electric field is measured in statvolts per centimeter. In the SI system which we use here as it is well known we have  $k = (e\pi\epsilon_0)^{-1}$ , where  $\epsilon_0 \approx 8.8554 \times 10^{-12}$  farad per meter and is called permittivity of free space. Of course the SI unit of charge is Coulomb (C), and the electric field is measured in volts per meter (V/m). The experimentally observed linear superposition of forces due to many charges means that we can write the electric field at  $\mathbf{x}$  due to a system of point charges  $q_i$ , located at  $\mathbf{x}_i$ ,  $i = 1, 2, \dots, n$  as the vector sum

$$\mathbf{E}(\mathbf{x}) = \frac{1}{4\pi\epsilon_0} \sum_{i=1}^n q_i \frac{\mathbf{x} - \mathbf{x}_i}{|\mathbf{x} - \mathbf{x}_i|^3} \quad (2.13)$$

If the charges are so small and so numerous that they can be described by a charge of density  $\rho(\mathbf{x}')$ , meaning that of  $\Delta q$  is the charge in a small volume  $\Delta x \Delta y \Delta z$  at the point  $\mathbf{x}'$ , then  $\Delta q = \rho(\mathbf{x}') \Delta x \Delta y \Delta z$ , the sum can be replaced by an integral:

$$\mathbf{E}(\mathbf{x}) = \frac{1}{4\pi\epsilon_0} \int \rho(\mathbf{x}') \frac{\mathbf{x} - \mathbf{x}_i}{|\mathbf{x} - \mathbf{x}_i|^3} d^3x \quad (2.14)$$

where  $d^3x = dx' dy' dz'$  is a three dimensional volume element at  $\mathbf{x}'$ .

### 2.2.3 The Dirac delta function.

In one direction the Delta function is written as  $\delta(x - a)$ . The Dirac delta function is a mathematically improper function and some of its properties are that  $\delta(x - a) = 0$  for  $x \neq a$  and  $\int \delta(x - a) dx = 1$  if the region of integration includes  $x = a$ , but is zero otherwise. The delta function can be given an intuitive, but nonrigorous, meaning as the limit of a peaked curve such as Gaussian that becomes narrower, but higher and higher, in such a way that the area under the curve is always constant. Schwartz's theory of distributions is a comprehensive rigorous mathematical approach to delta functions and manipulations. A discrete set of point charges can be described with a charge density by means of delta functions. For example

$$\rho(\mathbf{x}) = \sum_{i=1}^n q_i \delta(\mathbf{x} - \mathbf{x}_i) \quad (2.15)$$

represents a distribution of  $n$  point charges  $q_i$ , located at the points  $\mathbf{x}_i$ .

### 2.2.4 Gauss's Law

Gauss law is another integral result, which is sometimes more useful and lead to a differential equation for  $\mathbf{E}(\mathbf{x})$ . Consider a point charge  $q$  and a closed surface  $S$ . The distance from the charge to a point on the surface is  $r$ . Moreover  $\mathbf{n}$  is the outwardly directed unit normal to the surface at that point and  $da$  is an element of the surface area. If the electric field  $\mathbf{E}$  at the point on the surface due to the charge  $q$  makes an angle  $\theta$  with the unit normal,

then the normal component of  $\mathbf{E}$  times the element area is:

$$\mathbf{E} \cdot \mathbf{n} da = \frac{q}{4\pi\epsilon_0} \frac{\cos\theta}{r^2} da \quad (2.16)$$

Since  $\mathbf{E}$  is directed along the line from the surface element to the charge  $q$ ,  $\cos\theta da = r^2 d\Omega$ , where  $d\Omega$  is the element of solid angle subtended by  $da$  at the position of the charge. Therefore

$$\mathbf{E} \cdot \mathbf{n} da = \frac{q}{4\pi\epsilon_0} d\Omega \quad (2.17)$$

If we now integrate the normal component of  $\mathbf{E}$  over the whole surface, it is easy to see that

$$\oint_S \mathbf{E} \cdot \mathbf{n} da = \begin{cases} q/\epsilon_0 \\ 0 \end{cases} \quad (2.18)$$

This result is Gauss's law for a single point charge. For a discrete set of charges, we have that

$$\oint_S \mathbf{E} \cdot \mathbf{n} da = \frac{1}{\epsilon_0} \sum_i q_i \quad (2.19)$$

where the sum is over only those charges inside the surface  $S$ . For a continuous charge density  $\rho(\mathbf{x})$ , Gauss's law becomes

$$\oint_S \mathbf{E} \cdot \mathbf{n} da = \frac{1}{\epsilon_0} \int_V \rho(\mathbf{x}) d^3x \quad (2.20)$$

where  $V$  is the volume enclosed by  $S$ . The equation above depends upon the inverse square law for the force between charges, the central nature of the force and the linear superposition of the effects of different charges. As a result it is clear that the Gauss law holds for Newtonian gravitational force fields, with matter density replacing charge density.

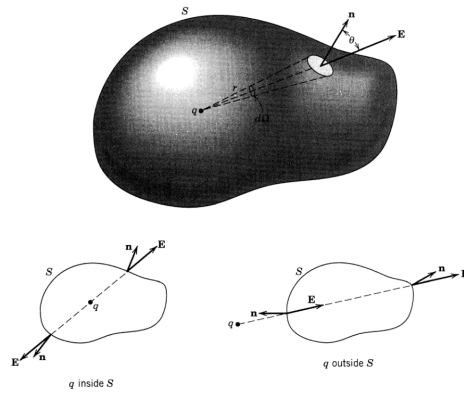


**Figure 2.4:** Gauss's law. The normal component of electric field is integrated over the closed surface  $S$ . If the charge is inside (outside)  $S$ , the total solid angle subtended at the charge by the inner side of the surface is  $4\pi$  (zero).

## 2.3 Charged particle motion

### 2.3.1 Lorentz force

Charged particles moving in a linear or circular accelerator are guided, confined and accelerated by external electromagnetic fields. More specific, the electric field in RF cavities is responsible of acceleration and the magnetic fields guide and focus the particles. This happens through the bending magnets, which guide the charges on the reference trajectory (orbit), the solenoids or quadrupoles for the transverse confinement, and the sextupoles for the chromaticity correction. The motion of a charged particle in a beam transport channel or in a circular accelerator is governed by the Lorentz force equation

$$\mathbf{F} = q(\mathbf{E} + \mathbf{v} \times \mathbf{B}) \quad (2.21)$$

where  $\mathbf{E}$  and  $\mathbf{B}$  are the electric and magnetic fields,  $\mathbf{v}$  is the particle velocity, and  $e$  is the electric charge of the particle. Or

$$\frac{d(m_0\gamma\mathbf{u})}{dt} = \mathbf{F}^{ext} = e(\mathbf{E} + \mathbf{v} \times \mathbf{B}) \quad (2.22)$$

where  $m_0$  is the rest mass,  $\gamma$  is the relativistic factor,  $\mathbf{v}$  is the particle velocity and  $e$  the charge of the particle. With the above equation we are able to calculate the trajectory of the charge moving through any electromagnetic field. The external forces  $\mathbf{F}^{ext}$  used for the beam transport and do not depend on the beam current. In a real accelerator, however, there is another important source of electromagnetic fields to be considered, the beam itself, which, circulating inside the pipe, produces additional electromagnetic fields called "self-fields". These fields, which depend on the intensity of the beam current and on the charge distribution, perturb the external guiding fields. The self-fields are responsible for a number of unwanted phenomena related to beam dynamics, such as energy loss, shift of the synchronous phase and frequency, shift of the betatron frequencies, and instabilities. The study of

self-fields can be divided into space charge fields and wakefields. The space charge forces are those generated directly by the charge distribution, with the inclusion of the image charges and currents. Using the first equation of this chapter, the Lorentz forces are applied as bending forces to guide the particles along a predefined ideal path, the design orbit, on which all particles should move, and as focusing forces to confine the particles in the vicinity of the ideal path, from which most particles will unavoidably deviate. In terms of cartesian components, we have:

$$F_x = q(E_x + v_y B_z - v_z B_y), \quad (2.23)$$

$$F_y = q(E_y + v_z B_x - v_x B_z), \quad (2.24)$$

$$F_z = q(E_z + v_x B_y - v_y B_x). \quad (2.25)$$

The electric and magnetic fields are functions of the position and time. For this reason the Lorentz force can be written as:

$$\mathbf{F}(\mathbf{r}, \dot{\mathbf{r}}, t, q) = q[\mathbf{E}(\mathbf{r}, t) + \dot{\mathbf{r}} \times \mathbf{B}(\mathbf{r}, t)] \quad (2.26)$$

$\mathbf{r}$  is the position vector of the charged particle,  $t$  is time.

## 2.4 Equations of motion

### Newton's second law

In classical non relativistic mechanics, and at low energies, the velocity of the particle increases with the square root of the kinetic energy. This is Newton's second law

$$\mathbf{F} = m\mathbf{a} \quad (2.27)$$

At relativistic energies, the velocity increases very slowly asymptotically approaching that of light. As we mentioned before, the charged particle dynamics starts from the problem of classical mechanics, whenever relativistic



effects can be neglected. In this approach, the motion of charged particles under the influence of electromagnetic fields is governed by Newton's second law, described via the Lorentz force and considered in three dimensional space. For a particle of rest mass  $m$  and charge  $q$ , the equations of motion are three (coupled) second-order ordinary differential equation

$$m\gamma \ddot{\mathbf{x}} = q(\dot{\mathbf{x}} \times \mathbf{B} + \mathbf{E}) \quad (2.28)$$

where  $\gamma$  is the relativistic factor,  $\mathbf{x}$  is the position of the particle as a function of time  $t$ ,  $\mathbf{B}$  and  $\mathbf{E}$  are the magnetic and electric fields, respectively, which may depend on both  $\mathbf{x}$  and  $t$  in general. This system correlate with the Maxwell's equations that describe the source and time evolution of the electromagnetic field. From the perspective of the single particle model, the electromagnetic field produced by the motion of the particle in turn is negligible compared to the solutions  $B$  and  $E$  of Maxwell's equations. However when we study, large numbers of particles this can no longer be the case. That is because ideally one would have to determine the total charge and current coming from the particles, insert them into Maxwell's equations, solve the latter all over again to find the modified electromagnetic fields, then replace the new solutions in the equations of motion and continue like this. Any dynamical system can be analyzed as a collection of particles, having mutual interactions, therefore in principle Newton's laws can provide a description of the motion developing from an initial configuration of positions and velocities. Nevertheless, the problem is that the equations may be intractable and unable to be analysed mathematically. It is evident that the Cartesian coordinate positions and velocities might not be the best choice of parameters to specify the system's configuration. After the reformulation of the Newton's laws in terms of more useful coordinates, the result is the Lagrange's equations. The Irish mathematician Hamiltonian then established that these improved dynamical equations could be derived using the calculus of variations to minimize an integral of a function, the Lagrangian, along a path in the system's configuration space. This integral is called the action,

so the rule is that the system follows the path of least action from the initial to the final configuration.

### Hamilton's equation

In general, there are only two steps in the analysis of any dynamical system. The first step is to write down the equations of motion and the second step is to solve them. In Hamiltonian mechanics, we describe the motion of a particle by at first compute the Hamiltonian in generalised coordinates  $(q, p)$  and then plug that into Hamilton's equations and then get 2 first order differential equations to solve. In an accelerator, magnets and rf cavities are generally defined along a trajectory. The motion of particles in electromagnetic fields is conservative, and similar to a harmonic oscillator with perturbations. If we know the Hamiltonian and Hamilton's equations, we can find the equations of motion for a dynamical system. Our first goal is find out the Hamiltonian

As we have already mentioned the Newton's law and Lorentz force

$$\frac{d\mathbf{p}}{dt} = \mathbf{F} \quad (2.29)$$

$$\mathbf{F} = q(\mathbf{E} + \mathbf{v} \times \mathbf{B}) \quad (2.30)$$

The Hamiltonian represents the total energy of the particle. The

$$H = c\sqrt{(\mathbf{p} - q\mathbf{A})^2 + m^2c^2} + q\phi \quad (2.31)$$

is the Hamiltonian for a relativistic charged particle moving in an electromagnetic field. This Hamiltonian is in a straight beam line. The Hamiltonian equations are

$$\frac{dx_i}{dt} = \frac{\partial H}{\partial p_i} \quad (2.32)$$

$$\frac{dp_i}{dt} = -\frac{\partial H}{\partial x_i} \quad (2.33)$$

In the equation (1.31), if we change the independent variable to  $z$  the distance

along the beamline  $(x, p_x), (y, p_y), (t, -E)$ . The Hamiltonian is

$$H = -p_z = -\sqrt{\frac{(E - q\phi)^2}{c^2} - (p_x - qA_x)^2 - (p_y - qA_y)^2 - m^2c^2} - qA_z \quad (2.34)$$

Later, we choose new (canonical) variables for the position and momentum that stay small as the particle moves along the beam line and scale by reference momentum  $P_0$  and We define new (canonical) longitudinal variables. Eventually, our Hamiltonian with independent variable  $s$  along the beamline, becomes

$$H = \frac{\delta}{\beta_0} - \sqrt{\left(\delta + \frac{1}{\beta_0} - \frac{q\phi}{cP_0}\right)^2 - (p_x - a_x)^2 - (p_y - a_y)^2 - \frac{1}{\beta_0^2\gamma_0^2}} - \alpha_z \quad (2.35)$$

$\delta = \frac{E}{cP_0} - \frac{1}{\beta_0}$  is the energy deviation.  $\mathbf{a} = \frac{q}{P_0}\mathbf{A}$  is the scaled vector potential and  $(x, p_x, y, p_y, z, \delta)$  are the coordinates and momenta. Using the Hamiltonian, we can get the equations of motion for a particle in a (straight) beam line. The Hamiltonian in a curved beam line is more complicated and we want to measure  $s$  along a path which curves with the trajectory of a particle on a curved orbit, which we call the reference trajectory and it turns out as a factor in front of the straight line Hamiltonian. In the physics of accelerator, relativistic definition of the momentum is used.

## 2.5 Useful formulas and relativity parameters

The definition of the relativistic momentum is expressed as a function of the rest mass  $m_0$ , which for an electron is about  $9.10938 \times 10^{-31}$  kg (or  $0.511$  MeV/ $c^2$ ),

$$\mathbf{p} = m_0\gamma \mathbf{u} \quad (2.36)$$

The relativistic factor  $\gamma$  is

$$\gamma = \frac{1}{\sqrt{1 - \beta^2}} \quad (2.37)$$

The relativistic velocity  $\beta$  is  $\beta = \frac{\mathbf{u}}{c}$ . The energy of a particle of rest mass  $m_0$  travelling at  $\mathbf{u}$  is

$$\mathbf{E} = m_0 \gamma c^2 \quad (2.38)$$

The basic unit of energy used is the energy of a particle of charge  $e$  would gain while being accelerated between two conducting plates at a potential difference of one Volt: one electron volt (eV). Now we have the following expression for energy

$$\mathbf{E}^2 = c^2 p^2 + m_0^2 c^4 \quad (2.39)$$

The following expression is for the momentum in the unit  $eV/c$  instead of the classic mechanics one, which is  $kg \cdot m/s$ . In the case of a conserved linear momentum, without external forces we can write

$$\mathbf{u} = \frac{d\mathbf{r}}{dt} = \frac{c^2 \mathbf{p}}{\mathbf{E}} \quad (2.40)$$

$$\mathbf{r} = cst + \frac{c^2 \mathbf{p}}{\mathbf{E}} \cdot t \quad (2.41)$$

**Longitudinal field and pure longitudinal momentum** In the common situation where  $\beta = \beta \mathbf{e}_z$ , the field in the laboratory frame will be reduced to

$$\mathbf{E}_z = \frac{\gamma + \gamma^2(1 - \beta^2)}{\gamma + 1} \cdot E'_z = E'_z \quad (2.42)$$

## 2.6 Codes: RF-Track, ASTRA

Space charge forces are the interaction forces between the particles of the bunch. These internal forces are often neglected as their amplitude might be small compared to the external fields applied to the particles. Nevertheless, for a better modelization of the bunch evolution in the accelerator, these forces should be taken into account. This thesis elaborates the benchmark of Space Charge forces between two tracking codes RF-Track and ASTRA. Both of them unlike many of the other particle tracking programs available, RF-Track and ASTRA accounts for space charge.

### 2.6.1 RF-Track

RF-Track is a minimalist multipurpose tracking code by Andrea Latina, which features space-charge. It is fully relativistic and able to handle Complex 3-D field maps of electromagnetic fields, implementing the simulation of RF backward/forward travelling waves as well as static fields. More specifically no assumptions are made, like  $\beta \ll 1$  or  $\gamma \gg 1$  and it has already been successfully tested with electrons, positrons, protons, anti protons and ions at various energies. It is flexible, fast, and tracks mixed-species beams, implementing high-order integration algorithms. RF-Track is a C++ library, which not only takes full advantage of modern C++ 11, but also is a fast optimised, fully parallel code, with great numerical stability. It is loadable from Octave and Python. RF-Track is able to perform full 6d tracking both in time or in space and uses macro particles to sample the phase space. There are two different bunch types in RF-Track software. The **Bunch6d**, for tracking the beam *in space*, and the **Bunch6dT** for tracking the beam *in time*. It is also possible to switch dynamically from one type to the other. These two beam models use different sets of phase-space coordinates for the internal representation of the beam. First of all it is important to say that, in both beam models of RF-Track, each macro particle carries three properties. the mass of the particle is expressed in  $\text{MeV}/c^2$ ,  $m$ , the particle's charge state is

expressed in  $e^+$ ,  $q$ , and the number of real particles carried by each macro particle,  $N$ . This feature enables the simulation of multiple species within the same bunch.

### 2.6.2 Bunch6d

When one uses `Bunch6d`, the integration is performed in space. Each particle's phase-space is the 6d vector  $(x, x', y, y', t, P)$  and the integration is performed over  $S$ , which is the beam longitudinal position along the accelerator. Furthermore, the object `Bunch6d` maintains a global coordinate  $S$  to track the longitudinal position of the bunch along the accelerator, which is updated element by element. The six phase-space coordinates utilised to describe each macro particle. Several constructors in the C++ source code exist to create a beam of type `Bunch6d`:

- `Bunch6d(mass, population, charge, [x x' y y' t P] $\times N_{\text{particles}}$ );`
- `Bunch6d(mass, population, charge, twiss, N, sigma_cut=3);`
- `Bunch6d(Bunch6dT);`
- `Bunch6d([x x' y y' t P m Q n] $\times N_{\text{particles}}$ );`

Although the internal representation of the beam is in time, as said, it is possible to inquire RF-Track and obtain the particles distribution in space. The two sets of phase space coordinates are indicated, respectively, with small and large case,  $(x, y, z)$  and  $(X, Y, Z)$ , as summarised in Tab. ?? together with their reciprocal relations.

### 2.6.3 Bunch6dT

When one uses the `Bunch6dT` the equations of motion are integrated in time. The 6d phase-space coordinates of each particle are  $(x, y, S, P_x, P_y, P_z)$ , and the object `Bunch6dT` maintains a global clock common to all particles,  $t$ , which is updated at each integration step. Additionally, `Bunch6dT` allows one to specify also the creation time of each particle, something that facilitates, for example, the simulation of cathodes and field emission. [7], [6] Several constructors also exist to create a bunch of type `Bunch6dT`

- Bunch6dT(*mass, population, charge,*  
 $\left[ x \text{ [mm]} \quad P_x \text{ [MeV/c]} \quad y \text{ [mm]} \quad P_z \text{ [MeV/c]} \quad S \text{ [mm]} \quad P_z \text{ [MeV/c]} \right]_{\times N_{\text{particles}}}$ );
- Bunch6dT(*mass, population, charge, twiss, N, sigma\_cut=3*);
- Bunch6dT(Bunch6d);
- Bunch6dT  
 $([x \text{ [mm]} P_x \text{ [MeV/c]} y \text{ [mm]} P_z \text{ [MeV/c]} S \text{ [mm]} P_z \text{ [MeV/c]} m \text{ [MeV/c}^2] Q \text{ [e]} n \text{ [e]}]_{\times N_{\text{particles}}})$ ;
- Bunch6dT  
 $([x \text{ [mm]} P_x \text{ [MeV/c]} y \text{ [mm]} P_z \text{ [MeV/c]} S \text{ [mm]} P_z \text{ [MeV/c]} m \text{ [MeV/c}^2] Q \text{ [e]} n \text{ [e]} t_0 \text{ [mm/c]}]_{\times N_{\text{particles}}})$ ;

$$\begin{aligned}
 x &= \text{horizontal position [mm]} & x' &= \frac{P_x}{P_z} \text{ horizontal angle [mrad]} \\
 y &= \text{vertical position [mm]} & y' &= \frac{P_y}{P_z} \text{ vertical angle [mrad]} \\
 t &= \text{time at which particle is at position } S \text{ [mm/c]} & P &= \text{total momentum [MeV/c]}
 \end{aligned}$$

**Figure 2.5:** The phase-space coordinates used by Bunch6d.

$$\begin{aligned}
 x &= \text{horizontal position [mm]} & P_x &= \text{horizontal momentum [MeV/c]} \\
 y &= \text{vertical position [mm]} & P_y &= \text{vertical momentum [MeV/c]} \\
 S &= \text{longitudinal position [mm]} & P_z &= \text{longitudinal momentum [MeV/c]}
 \end{aligned}$$

**Figure 2.6:** The phase-space coordinates used by Bunch6dT.

### 2.6.4 ASTRA

Astra (A Space Charge Tracking Algorithm) program package consists of the four parts. The program generator, which may be used to generate an initial particle distribution. The program Astra, which tracks the particles under the influence of external and internal fields. The graphic program field-plot, which is used to display electromagnetic fields of beam line elements and space charge fields of particle distributions. The graphic program post-pro, which is used to display phase space plots of particle distributions and allows a detailed analysis of the phase space distribution. And last but not least, the graphic program lineplot, which is used to display the beam size, emittance, bunch length etc. versus the longitudinal beam line position or versus a scanned parameter, respectively. Astra is written in Fortran 90 and runs on different platforms. The input files for the programs generator and Astra are organized in form of Fortran 90 namelists. Each namelist starts with an ampersand (&) followed by the name of the namelist and ends with a slash (/). Below are some more important and useful references: [9], [2], [5].



## Chapter 3

# Numerical implementation of Space-Charge forces

In a classical numerical code, the beam is represented by  $N$  macro-particles ( $N$  is normally less than the actual particle number in the beam) that can be considered as a statistical sample of the beam with the same dynamics as the real particles. The macro-particles are transported through the accelerator step by step and at each time step  $dt$  the following happens. The external forces acting on each macro-particle are calculated, the space-charge fields and the resulting forces are calculated, and the equation of motion is solved for each macro-particle. The space-charge electric field can be computed by a particle-particle interaction (PPI) method or a particles-in-cells (PIC) method.

### 3.1 Particle-to-Particle force

In this method for each macro-particle  $i$  of charge  $q$ , it is assumed that the applied space-charge electrostatic field,  $\mathbf{E}_i$  is the sum of all the fields induced by all the other macro-particles:

$$\mathbf{E}_i = \frac{q}{4\pi\epsilon_0} \sum_{j \neq i} \frac{\mathbf{r}_j - \mathbf{r}_i}{||\mathbf{r}_j - \mathbf{r}_i||^3} \quad (3.1)$$

The advantages of this method are that it is easy to code and the electric field is directly computed on the macro-particles. The main disadvantages are that the method is time-consuming for calculation (proportional to the square of the number of macro-particles) and the obtained space-charge field map is not smooth (the lower the macro-particle number, the more granularity), which can lead to non-physical emittance growth. As we mentioned in this approach the goal is to compute the particle-to-particle force. More specifically, if one has  $N$  particles, this method requires that  $N \cdot (N - 1) \sim N^2$  computations. For instance, if one has  $N = 100'000$  macroparticles, then one needs  $10^{10}$  computations.

### 3.2 Particle in cell and FFT

In this case, the physical simulated space is meshed. The meshing can be in one, two or three dimensions, depending on the symmetry of the simulated geometry and the beam. The average beam density at each node of the mesh is obtained by counting the number of particles that are located close to it. Once the density function is obtained, the field at each node is computed by solving the Poisson equation. There are several techniques, that can be used to solve this equation at each node of the mesh. One of these techniques is a direct method, in which the field is directly calculated at each node of the mesh. The calculation time is proportional to the square of the mesh number. Another technique is the fast Fourier transform (FFT) method. The field at one node is given by the convolution product of the density and a Green's function. This can be solved by using the fact that a Fourier transform of a convolution product is equal to the product of the Fourier transforms. If  $N$  is the mesh number, the calculation time is proportional to  $N \cdot \log(N)$ . Another method is the relaxation method, which is an iterative method. If  $n$  is the mesh number, the calculation time is  $N^2$ . Once the field at each node is known, the field at the macro-particle location is calculated by interpolation from the closest nodes. After the evaluation of the beam

density and the field for each particle, the computing time is proportional to the macro-particle number. The PIC codes are the most commonly used for space-charge calculations, as they are the fastest and the most efficient. A compromise has to be found between the mesh size and the particle number in order to reach a sufficient resolution while avoiding some numerical noise that can lead to non-physical effects. As an example let's consider a mesh that has  $32 \times 32 \times 32$  points, this algorithm requires  $N \cdot \log(N)$  computations. If  $N = 32 \times 32 \times 32$ ,  $N \cdot \log(N) \sim 150 \times 10^3$  computations (which is 700000 times smaller than particle-particle approach).

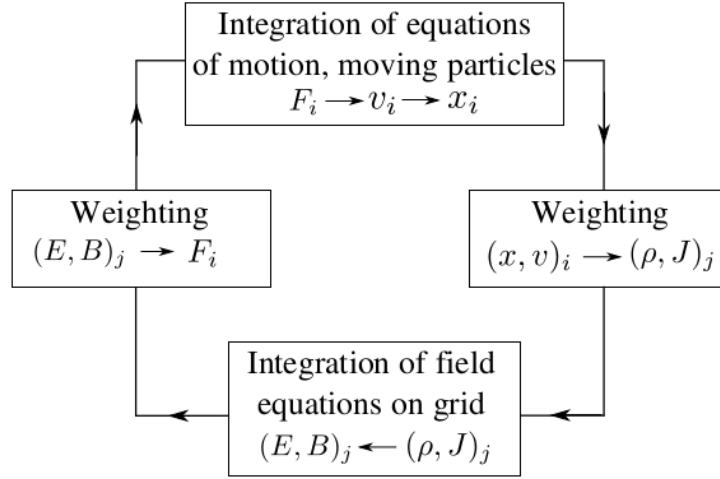


**Figure 3.1:** Algorithm of a PIC code dedicated to particle transport with space charge. The particles are numbered as  $i$ , the grid indices are  $j$ .

### 3.3 Particle-in-cell (FFT) approach

As we mentioned in the PIC, FFT method the field at one node is given by the convolution product of the density and a Green's function and this can be solved by using the fact that a Fourier transform of a convolution product is equal to the product of the Fourier transforms. Let's start with the Green theorem.

### Green's Theorem

If electrostatic problems always involved localized discrete or continuous distributions of charge with no boundary surfaces, the general solution would be the most convenient and straightforward solution to any problem. There would be no need of the Poisson or Laplace equation. In actual fact, many of the problems of electrostatics involve finite regions of space, with or without charge inside, and with prescribed boundary conditions on the bounding surfaces. These boundary conditions may be simulated by an appropriate distribution of charges outside the region of interest (perhaps at infinity), but becomes inconvenient as a means of calculating the potential, except in simple cases (e.g., method of images). To handle the boundary conditions it is necessary to develop some new mathematical tools, such as the identities or theorems due to Green's. The divergence theorem, is the following

$$\int_V \nabla \cdot \mathbf{A} d^3x = \oint_S \mathbf{A} \cdot \mathbf{n} da \quad (3.2)$$

applies to any vector field  $\mathbf{A}$  defined in the volume  $V$  bounded by the closed surface  $S$ . Let  $\mathbf{A} = \phi \nabla \psi$ , where  $\phi$  and  $\psi$  are arbitrary scalar fields. Now

$$\nabla \cdot (\phi \nabla \psi) = \phi \nabla^2 \psi + \nabla \phi \cdot \nabla \psi \quad (3.3)$$

and

$$\phi \nabla \psi \cdot \mathbf{n} = \phi \frac{\partial \psi}{\partial n} \quad (3.4)$$

where  $\partial/\partial n$  is the normal derivative at the surface  $S$  (directed outward from inside the volume  $V$ ). When the previous equations are substituted into the divergence theorem, there results Green's first identity:

$$\int_V (\phi \nabla^2 \psi + \nabla \phi \cdot \nabla \psi) d^3x = \oint_S \phi \frac{\partial \psi}{\partial n} da \quad (3.5)$$

If we write the equation again with  $\phi$  and  $\psi$  interchanged, and then subtract it, we obtain Green's second identity or Green's theorem:

$$\int_V (\phi \nabla^2 \psi + \psi \nabla^2 \phi) d^3x = \oint_S [\phi \frac{\partial \psi}{\partial n} - \psi \frac{\partial \phi}{\partial n}] da \quad (3.6)$$

The Poisson differential equation for the potential can be converted into an integral equation if we choose a particular  $\psi$ , namely  $1/R \equiv 1/|\mathbf{x} - \mathbf{x}'|$ , where  $\mathbf{x}$  is the observation point and  $\mathbf{x}'$  is the integration variable. Further, we put  $\phi = \Phi$ , the scalar potential, and make use of  $\nabla^2 \Phi = -\rho/\epsilon_0$ . From previous equation we know that  $\nabla^2(1/R) = -4\pi\delta(\mathbf{x} - \mathbf{x}')$ , so the previous equation becomes

$$\int_V [-4\pi\Phi(\mathbf{x}')\delta(\mathbf{x} - \mathbf{x}') + \frac{1}{\epsilon_0 R}\rho(\mathbf{x}')] d^3x' = \oint_S [\Phi \frac{\partial}{\partial n'}(\frac{1}{R}) - \frac{1}{R} \frac{\partial \Phi}{\partial n}] da' \quad (3.7)$$

If the point  $\mathbf{x}$  lies within the volume  $V$ , we obtain:

$$\Phi(\mathbf{x}) = \frac{1}{4\pi\epsilon_0} \int_V \frac{\rho(\mathbf{x}')}{R} d^3x' + \frac{1}{4\pi} \oint_S [\frac{1}{R} \frac{\partial \Phi}{\partial n'} - \Phi \frac{\partial}{\partial n'}(\frac{1}{R})] da' \quad (3.8)$$

The solution of the Poisson or Laplace equation in a finite volume  $V$  with either Dirichlet or Neumann boundary conditions on the bounding surface  $S$  can be obtained by means of the Green's functions. We choose the function  $\psi$  to be  $\frac{1}{|\mathbf{x} - \mathbf{x}'|}$ , it being the potential of a unit point source, satisfying the equation:

$$\nabla'^2(\frac{1}{|\mathbf{x} - \mathbf{x}'|}) = -4\pi\delta(\mathbf{x} - \mathbf{x}') \quad (3.9)$$

The function  $\frac{1}{|\mathbf{x} - \mathbf{x}'|}$  is only one of a class of functions depending on the variables  $\mathbf{x}$  and  $\mathbf{x}'$ , and called Green's functions. In general,

$$\nabla'^2 \mathbf{G}(\mathbf{x}, \mathbf{x}') = -4\pi\delta(\mathbf{x} - \mathbf{x}') \quad (3.10)$$

where

$$\mathbf{G}(\mathbf{x}, \mathbf{x}') = \frac{1}{|\mathbf{x} - \mathbf{x}'|} + F(\mathbf{x}, \mathbf{x}') \quad (3.11)$$

with the function  $F$  satisfying the Laplace equation inside the volume  $V$ :

$$\nabla'^2 F(x, x') = 0 \quad (3.12)$$

### 3.3.1 The Green's function for the Laplacian

If we have the problem to solve for the  $\phi(x)$  inside the desirable region. Then the integral  $\int_V \phi(x') \delta(x - x') d^3x'$  reduces to simply  $\phi(x)$ , because of the defining property of the Dirac delta function, that we mentioned before. As a result we have that

$$\phi(x) = - \int_V G(x, x') \rho(x') d^3x' + \int_S [\phi(x') \nabla' G(x, x') - G(x, x') \nabla' \phi(x')] \cdot d\hat{\sigma}' \quad (3.13)$$

This form expresses the harmonic functions. In electrostatics it has already mentioned,  $\phi(x)$  is interpreted as the electric potential and  $\rho(x)$  is the electric charge density. The normal derivative  $\nabla \phi(x') \cdot d\hat{\sigma}'$  is the normal component of the electric field. The normal derivative of  $G(x, x')$  cannot vanish on the surface, since it must integrate to 1 on the surface, because the application of Gauss's theorem to the differential equation defining the Green's function yields

$$\int_S \nabla' G(x, x') \cdot d\hat{\sigma}' = \int_V \nabla'^2 G(x, x') d^3x' = \int_V \delta(x - x') d^3x' = 1 \quad (3.14)$$

The simplest form the normal derivative can take is that of a constant, namely  $1/S$ , where  $S$  is the surface area of the surface. The surface term in the solution becomes

$$\int_S \phi(x') \nabla' G(x, x') \cdot d\hat{\sigma}' = \langle \phi \rangle_S \quad (3.15)$$

$\langle \phi \rangle_S$  is the average value of the potential on the surface. So with no boundary conditions, the Green's function for the Laplacian is

$$G(\mathbf{x}, \mathbf{x}') = -\frac{1}{4\pi|\mathbf{x} - \mathbf{x}'|} \quad (3.16)$$

where we have as  $\mathbf{x}$  the standard Cartesian coordinates in a three-dimensional space and of course

$$\frac{1}{|\mathbf{x} - \mathbf{x}'|} = [(x - x')^2 + (y - y')^2 + (z - z')^2]^{-\frac{1}{2}} \quad (3.17)$$

Supposing that the bounding surface goes out to infinity and plugging in this expression for the Green's function finally yields the standard expression for electric potential in terms of electric charge density as

$$\phi(x) = \int_V \frac{\rho(x')}{4\pi\epsilon|\mathbf{x} - \mathbf{x}'|} d^3x' \quad (3.18)$$

Which is for a general charge distribution. From the above we realize that the Green's function is used to describe the response of a particular type of physical system to a point source. One physical system is a charge distribution in electrostatics. The convolution of the Green's function and the electric charge density is implemented inside the source code of RF-Track, but also in the mathematical model in Matlab, in order to compare the results better.

### 3.3.2 FFT and Green's function

Since FFT accelerates the numerical computation within an acceptable amount of time, Fourier transform has been widely used for convolution computations. The FFT convolution routine, is the basic and the simplest routine for the numerical convolution implementation. Space charge effects are included in the simulations. This reduces the computational time significantly, which is something very important. The space charge forces are calculated by solving the 3D Poisson equation with open boundary conditions using a standard or integrated Green's function method.

### 3.3.3 FFT Mesh

If we define a mesh, this introduces us to a discretization of space. For example this rectangular computation domain  $[-L_x, L_x] \times [-L_y, L_y] \times [-L_t, L_t]$ , which can include all particles, is segmented into a regular mesh of  $M = M_x \times M_y \times M_t$  grid points. We can assume that  $N = M_x = M_y = M_t$ . If we assume that, where  $N_p$  is the number of macro-particles we can compute  $N_p^2$  point-to-point interactions. Instead of this, the potential can be also calculated on a grid of size  $(2N)^d$ , where  $N$  is the number of grid points in each dimension of the physical mesh containing the charge, and where  $d$  is the dimension of the problem. This calculation can be performed using Fast Fourier Transform (FFT) techniques. Once again let's start with the solution of the Poisson equation,

$$\nabla^2 \phi = -\rho/\epsilon_0, \quad (3.19)$$

If we take the appropriate boundary conditions, the scalar potential,  $\phi$ , can be written as,

$$\phi(x, y, z) = \iiint dx' dy' dz' \rho(\mathbf{x}', \mathbf{y}', \mathbf{z}') G(x - x', y - y', z - z'), \quad (3.20)$$

where  $G(x - x', y - y', z - z')$  is the Green's function, from the previous chapter, now written more analytical rather than  $G(x, x')$ . The Green's function in the appropriate boundary conditions, describes the contribution of a source charge at location  $(x', y', z')$  to the potential at an observation location  $(x, y, z)$ . For an isolated distribution of charge this can be written as

$$\phi(x, y, z) = \iiint dx' dy' dz' \rho(\mathbf{x}', \mathbf{y}', \mathbf{z}') G(x - x', y - y', z - z') \quad (3.21)$$



A discretization of on a Cartesian grid with cell size  $(h_x, h_y, h_z)$  leads to,

$$\phi_{i,j,k} = h_x h_y h_z \sum_{i'=1}^{M_x} \sum_{j'=1}^{M_y} \sum_{k'=1}^{M_t} \rho_{i',j',k'} G_{i-i',j-j',k-k'}, \quad (3.22)$$

where  $\rho_{i,j,k}$  and  $G_{i-i',j-j',k-k'}$  denote the values of the charge density and the Green's function, respectively, defined on the grid  $M$ .

### FFT Convolutions and Zero Padding

FFT's can be used to compute convolutions by appropriate zero-padding of the sequences.

$$\bar{\phi}_j = \sum_{k=0}^{K-1} \bar{\rho}_k \bar{G}_{j-k} \quad , \quad \begin{array}{l} j = 0, \dots, J-1 \\ k = 0, \dots, K-1 \\ j-k = -(K-1), \dots, J-1 \end{array} \quad (3.23)$$

$\bar{G}$  is the free space Green's function,  $\bar{\rho}$  is the charge density, and  $\bar{\phi}$  is the scalar potential. The sequence  $\bar{\phi}_j$  has  $J$  elements,  $\bar{\rho}_k$  has  $K$  elements, and  $\bar{G}_m$  has  $M = J + K - 1$  elements. If someone zero-pads the sequences to a length  $N \geq M$  and use FFT's to efficiently obtain the  $\bar{\phi}_j$  in the unpadded region. This defines a zero-padded charge density,  $\rho$ ,

$$\rho_k = \begin{cases} \bar{\rho}_k & \text{if } k = 0, \dots, K-1 \\ 0 & \text{if } k = K, \dots, N-1. \end{cases} \quad (3.24)$$

Now the periodic Green's function,  $G_m$  is

$$G_m = \begin{cases} \bar{G}_m & \text{if } m = -(K-1), \dots, J-1 \\ 0 & \text{if } m = J, \dots, N-K, \\ G_{m+iN} = G_m & \text{for } i \text{ integer} . \end{cases} \quad G \quad (3.25)$$

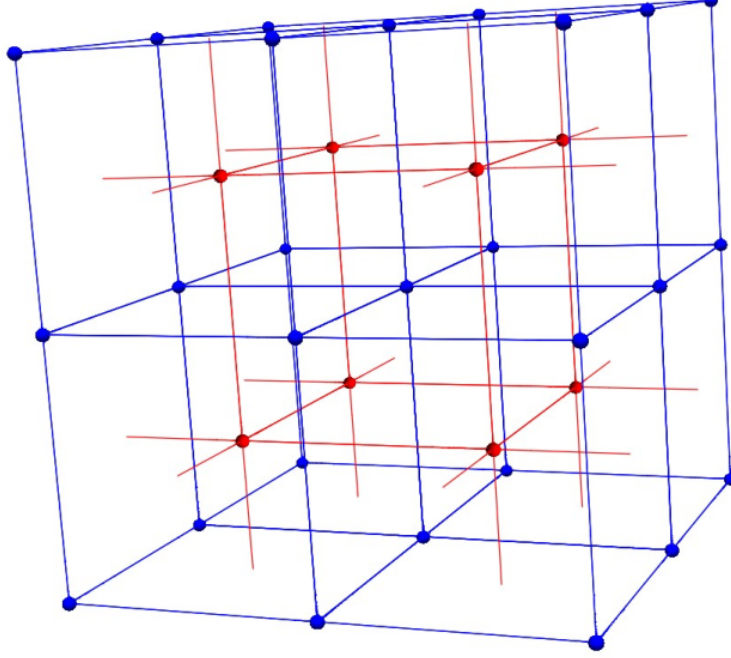


**Figure 3.2:** A schematic plot of the grid arrangement used for the numerical integrals.

And the sum is

$$\phi_j = \frac{1}{N} \sum_{k=0}^{N-1} e^{-2\pi i/N-jk} \left( \sum_{n=0}^{N-1} \rho_n e^{-2\pi i/Nnk} \right) \left( \sum_{m=0}^{N-1} G_m e^{-2\pi i/Nmk} \right), \quad 0 \leq j \leq N-1, \quad (3.26)$$

Since we have  $\tilde{\rho}$  and  $\tilde{G}$  and we convolve them, obtaining  $\tilde{p\tilde{h}i}$ , which later we deconvolve, having eventually 4 operations in one. Convolutions and 1 reverse Fourier transformation. This is just the FFT-based convolution of  $\rho_k$  with  $G_k$  as we mentioned in the previous chapter. Then,

$$\phi_j = \sum_{n=0}^{K-1} \sum_{m=0}^{N-1} \bar{\rho}_n G_m \frac{1}{N} \sum_{k=0}^{N-1} e^{-2\pi i/N(m+n-j)k} \quad 0 \leq j \leq N-1. \quad (3.27)$$

Now use the relation

$$\sum_{k=0}^{N-1} e^{-2\pi i/N(m+n-j)k} = N\delta_{m+n-j, iN} \quad (i \text{ an integer}). \quad (3.28)$$

As a result

$$\phi_j = \sum_{n=0}^{K-1} \bar{\rho}_n G_{j-n+iN} \quad 0 \leq j \leq N-1. \quad (3.29)$$

$G$  is periodic with period  $N$ . So,

$$\phi_j = \sum_{n=0}^{K-1} \bar{\rho}_n G_{j-n} \quad 0 \leq j \leq N-1. \quad (3.30)$$

In the physical (unpadded) region,  $j \in [0, J-1]$ , the quantity  $j-n$  satisfies  $-(K-1) \leq j-n \leq J-1$ . In other words the values of  $G_{j-n}$  are identical to  $\bar{G}_{j-n}$ . The zero-padded sequences have to have a length  $N \geq M$ , where  $M$  is the number of elements in the Green's function sequence  $\{x_m\}$ . Someone choose  $N = M$ , in which case the Green's function sequence is not padded at all, and only the charge density sequence,  $\{r_k\}$ , is zero-padded, with  $k = 0, \dots, K-1$  corresponding to the physical region and  $k = K, \dots, M-1$  corresponding to the zero-padded region. The Green's function is a symmetric function of its arguments, the value at the end of the Green's function array (at grid point  $J-1$  in this discussion) (at grid point  $J-1$ ) can be dropped, since it will be recovered implicitly through the symmetry of periodic Green's function. The Fast Fourier Transform (FFT) on the mesh is a very fast and accurate method.



# Chapter 4

## Case Studies

In order to validate the space charge algorithm, comparisons have been done with theoretical expressions of space charge fields. This happened for cylindrical and ellipsoidal distributions. In our case the ellipsoidal distribution is an ellipsoid with radial symmetry, hence we can call it a spheroid. The comparison has been made between RF-Track, ASTRA and the same analytical and numerical implementations in Octave. The results are presented in this chapter.

### 4.1 Uniformly charged sphere

Let's consider a uniformly charged sphere. By symmetry, we expect that the electric field generated by a spherically symmetric charge distribution to point radially towards, or away from, the center of the distribution, and to depend only on the radial distance  $r$  from this point. Consider a gaussian surface which is a sphere of radius  $r$ , centred on the center of the charge distribution. Applying Gauss law we have

$$A(r)E_r(r) = \frac{q(r)}{\epsilon_0} \quad (4.1)$$

where  $A(r) = 4\pi r^2$  is the area of the surface,  $E_r(r)$  the radial electric field strength at radius  $r$ , and  $q(r)$  the total charge enclosed by the surface. It is also easy to see that

$$q(r) = \begin{cases} Q & r \geq a \\ Q (r/a)^3 & r < a \end{cases} . \quad (4.2)$$

So,

$$E_r(r) = \begin{cases} \frac{Q}{4\pi\epsilon_0 r^2} & r \geq a \\ \frac{Qr}{4\pi\epsilon_0 a^3} & r < a \end{cases} . \quad (4.3)$$

The electric field strength is proportional to  $r$  inside the sphere, but falls off like  $1/r^2$  outside the sphere. Let's consider now a uniformly distributed and electron charged sphere. The radius of the sphere is 1 mm.

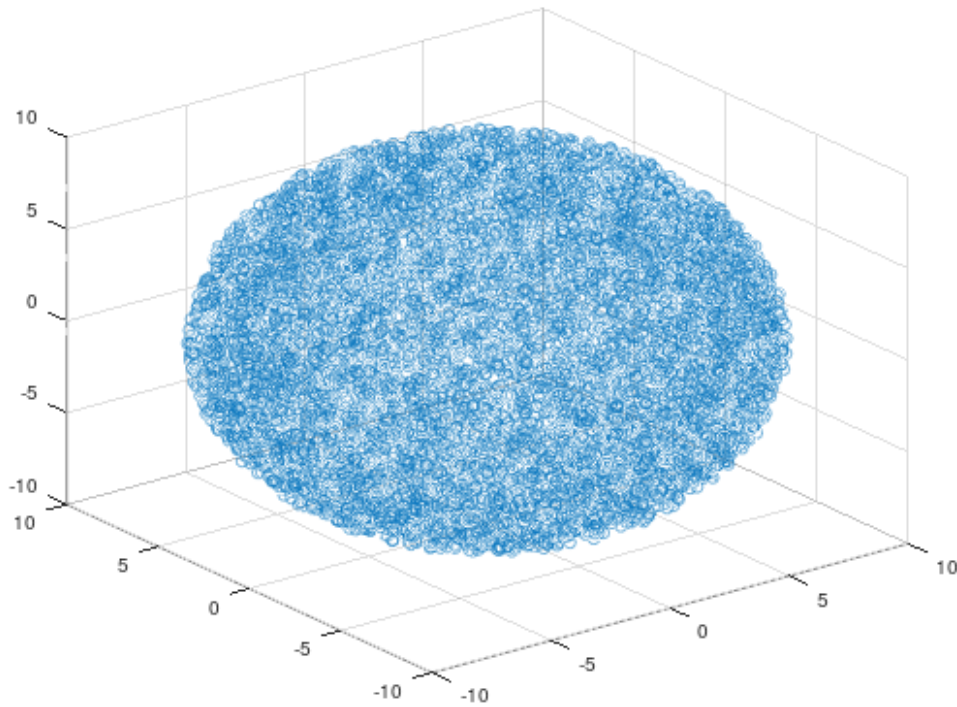


**Figure 4.1:** An example of a simple uniformly distributed sphere made in Octave with radius of 10 mm.

On the figure 3.2 one can see the good agreement between the plots of RF-Track and the analytical implementation of the electric charge in a sphere. The creation of the beam happens in Octave script with RF-Track. The results are presented in the plot below. This plot compares the analytic formula to the RF-Track simulations. There is no discrepancy and the compatibility of the RF-Track software with the analytical formula is very good. The light blue line is the analytic formula and the rest of them are the plots from RF-Track for different PIC. In the plot of the Figure of 3.2,

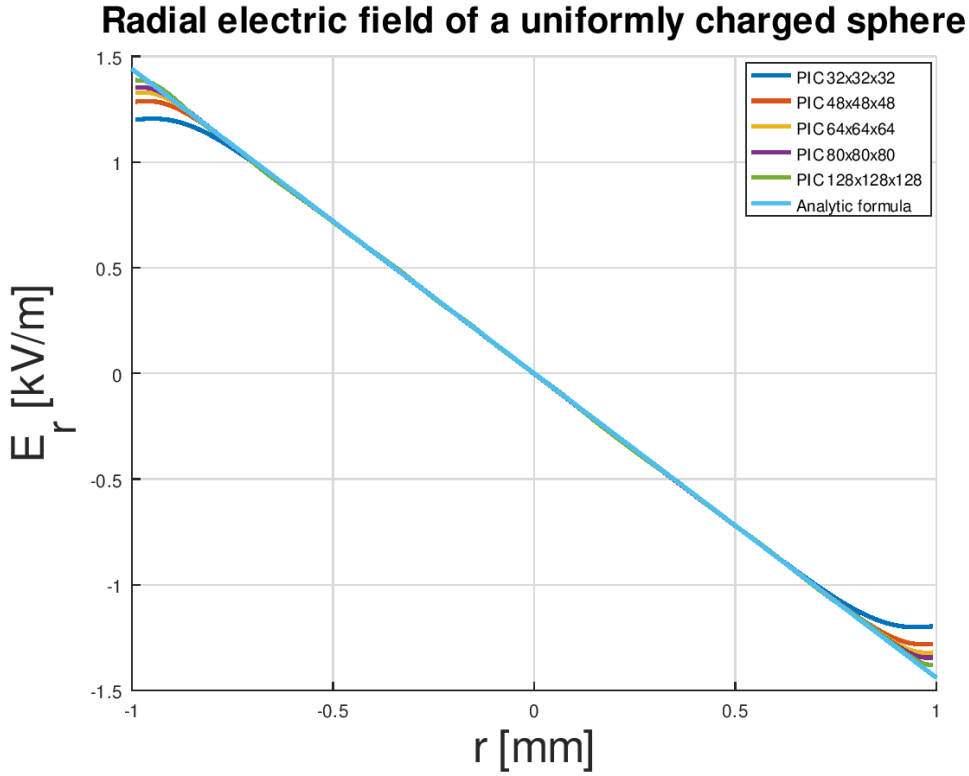


**Figure 4.2:** Radial Electric Field of a uniformly charged sphere. Comparison between RF-Track with different mesh shells and the analytic formula. In this plot there are PIC  $32 \times 32 \times 32$ , PIC  $48 \times 48 \times 48$ , PIC  $64 \times 64 \times 64$ , PIC  $128 \times 128 \times 128$ .

the x-axis is represented by  $r$  in mm and the y-axis is represented  $E_r$  in units of kV/m. The number of the simulated macroparticles is 1'000'000 and we have electrons with charge of one electron  $-1$ . The radius of the simulated

sphere as it shows in the figure is 1 mm. The next step is to compare the analytical solution for the electric field with the numeric solution of the green function in Octave in order to validate better the results of the calculation of the electric field in RF-Track. Since it is important to note that RF-Track calculates electric field with the green function, which explained in the previous chapter. As someone can see in the next figures, the simulation results are in a very good and reasonable agreement and within expectations.

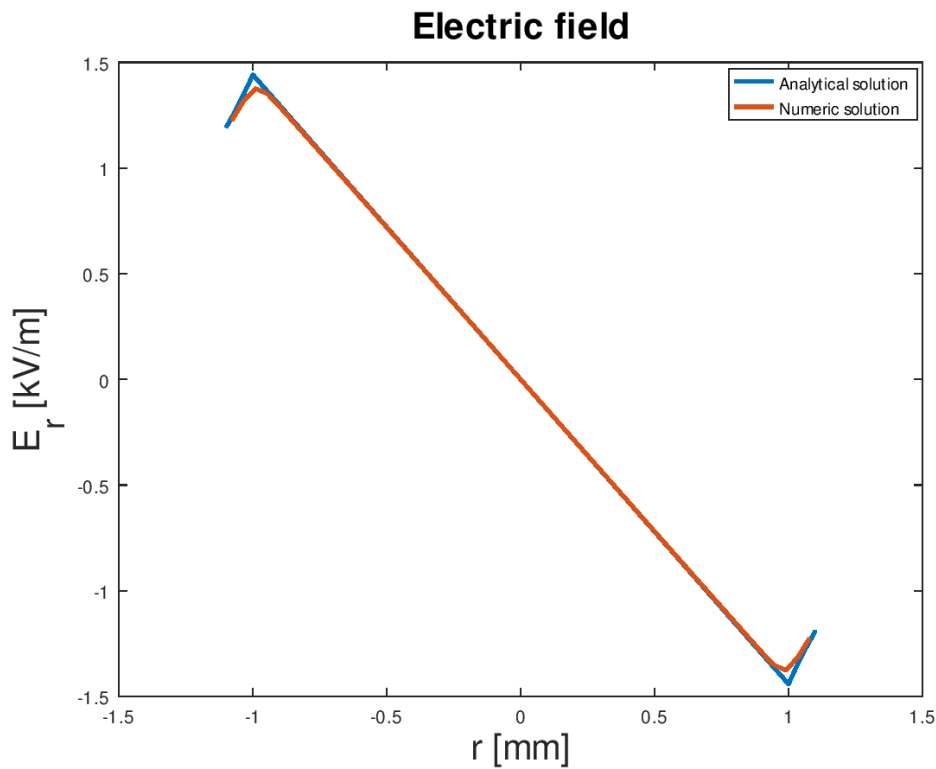


**Figure 4.3:** The comparison of the electric field between the analytical (blue line) and the numerical solution with the green function (red line), in Octave.



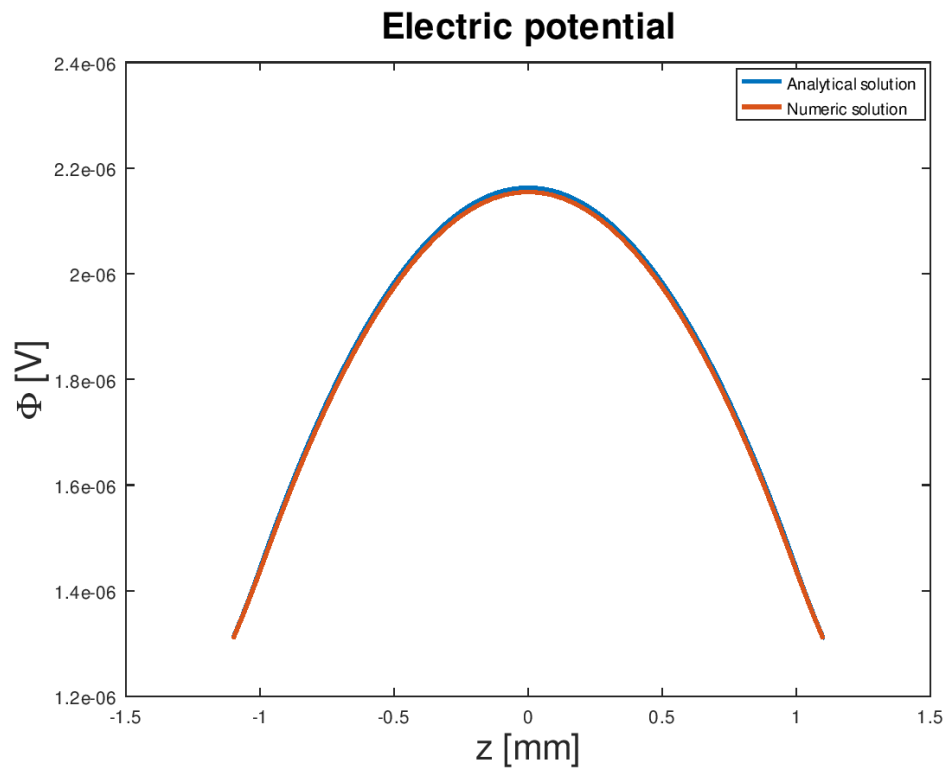


**Figure 4.4:** The comparison of the electric potential between the analytical (blue line) and the numerical solution with the green function (red line), in Octave.

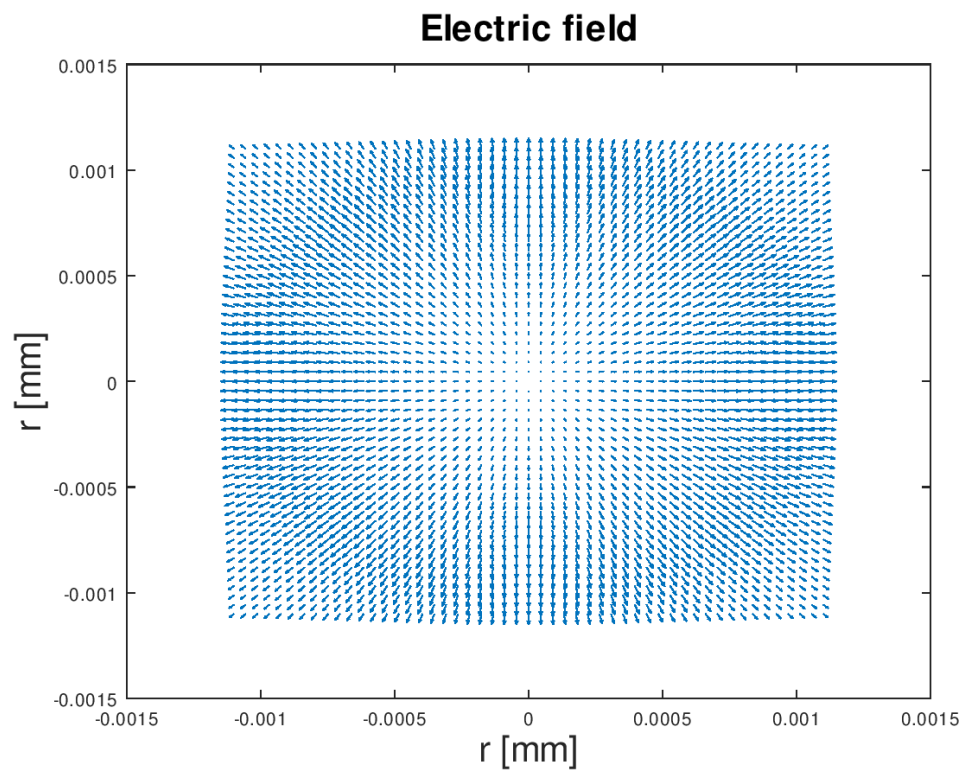


**Figure 4.5:** The electric field in the sphere, in Octave.

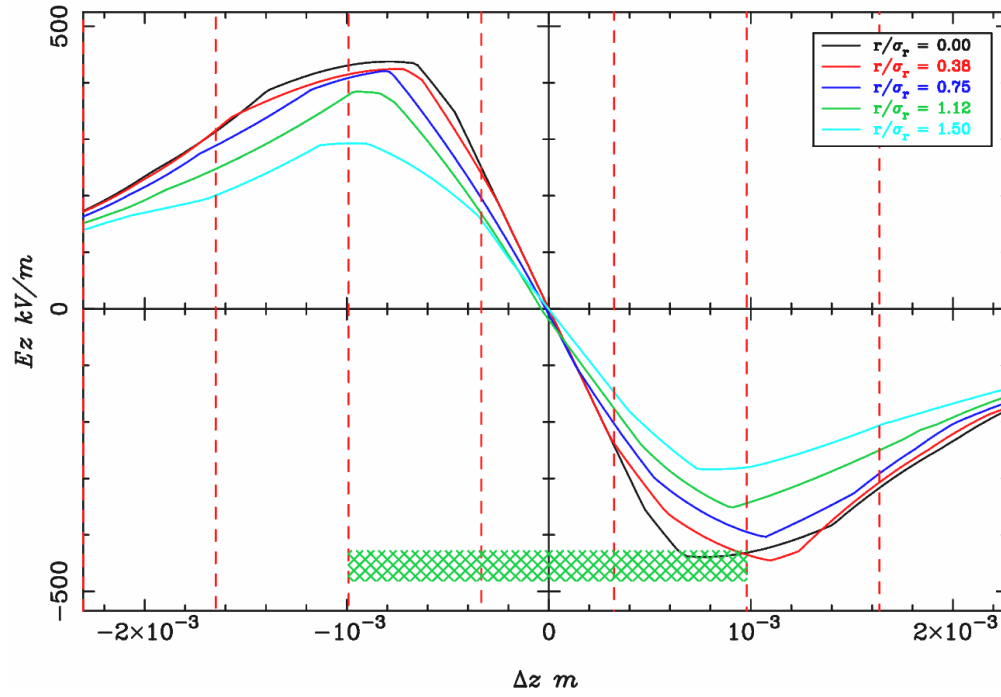


**Figure 4.6:** The results for the electric field for the same uniformly distributed sphere with ASTRA, with radial uniform distribution, similar to that simulated with the RFT and Octave.

In the Figure 3.8, one can see again the good agreement that RF-Track had with both analytical and numerical solutions.

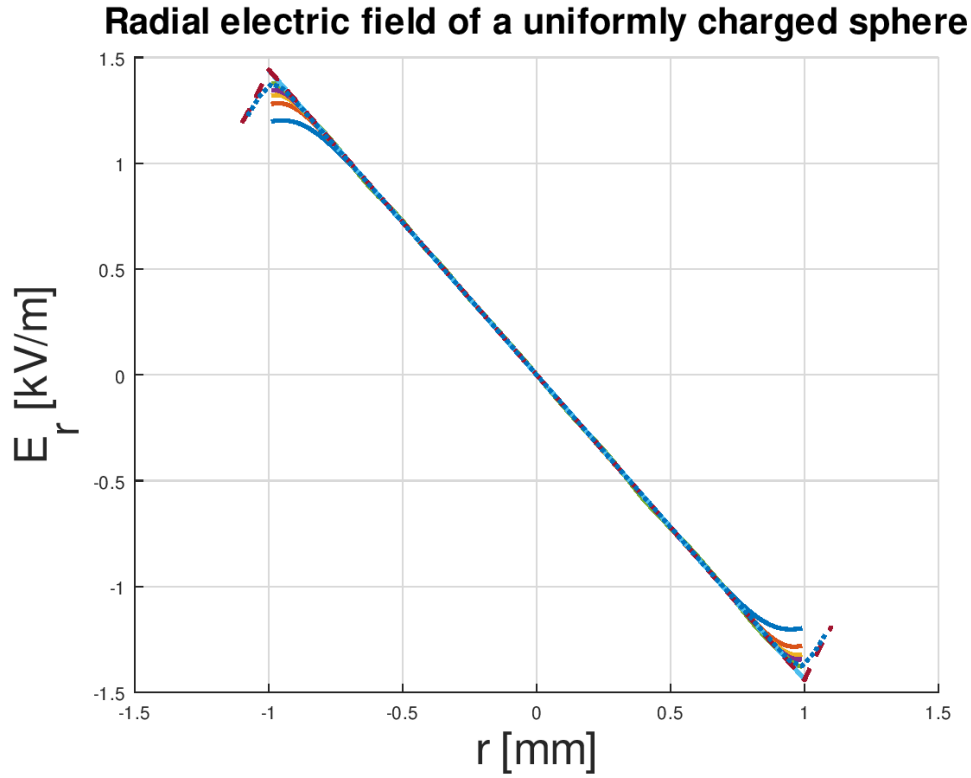


**Figure 4.7:** The comparison of the electric field in one plot of the analytical and numerical solution in Octave and the simulation in RF-Track. The dashed line is the analytical solution. The dotted line is the numerical solution and the solid lines are the simulations from RF-Track, for different PIC. In this plot there are PIC  $32 \times 32 \times 32$ , PIC  $48 \times 48 \times 48$ , PIC  $64 \times 64 \times 64$ , PIC  $128 \times 128 \times 128$ .

## 4.2 Cylindrical distribution

In this chapter one considers a cylinder of uniformly distributed charge. The electric field in a cylindrically symmetrical situation depends only on the distance from the axis. The electric field of an infinite cylinder of uniform volume charge density can be obtained by using Gauss law. Considering a Gaussian surface in the form of a cylinder at radius  $r > R$ , the electric field has the same magnitude at every point of the cylinder and is directed outward. The electric flux is then just the electric field times the area of the cylinder. Beginning with the theoretical expression of the potential, we consider a homogeneous distribution of charges in a cylindrical volume with revolution symmetry around the longitudinal axis Oz. The potential on any point  $z_0$  of this axis can be expressed using the Biot-Savart law

$$\Phi(0, z_0) = \frac{\rho}{4\pi\epsilon_0} \int_r \int_z \frac{2\pi r}{\sqrt{r^2 + (z - z_0)^2}} dr dz \quad (4.4)$$

$\rho$  is the density of charges. For a cylinder of semi-axis  $b$  and a radius  $a$  with  $N$  charges we have for  $\rho$

$$\rho = \frac{Ne}{2b\pi a^2} \quad (4.5)$$

We integrate the first equation along  $r$ , between  $r = 0$  and  $r = a$  and then change the variable  $Z = z_0 - z$

$$\Phi(0, z_0) = \frac{\rho}{2\epsilon_0} \int_{z_0-b}^{z_0+b} (\sqrt{a^2 + Z^2} - |Z|) dZ \quad (4.6)$$

Eventually for a cylindrical distribution, the potential inside,  $|z_0| < b$  and the potential outside,  $|z_0| > b$  are

$$\begin{aligned} \Phi(0, 0, z_0)_{int} = \Phi_0 + \frac{\rho}{2\epsilon_0} \{ & -(z_0^2 + b^2) + \frac{1}{2} [a^2 (\operatorname{arcsinh} \frac{z_0 + b}{a} - \operatorname{arcsinh} \frac{z_0 - b}{a}) \\ & + (z_0 + b) \sqrt{(z_0 + b)^2 + a^2} - (z_0 - b) \sqrt{(z_0 - b)^2 + a^2}] \} \end{aligned} \quad (4.7)$$

$$\begin{aligned} \Phi(0, 0, z_0)_{ext} = \Phi_0 + \frac{\rho}{2\epsilon_0} \{ & -2bz_0 + \frac{1}{2} [a^2 (\operatorname{arcsinh} \frac{z_0 + b}{a} - \operatorname{arcsinh} \frac{z_0 - b}{a}) \\ & + (z_0 + b) \sqrt{(z_0 + b)^2 + a^2} - (z_0 - b) \sqrt{(z_0 - b)^2 + a^2}] \} \end{aligned} \quad (4.8)$$

From the expression of the potential, the field component  $E_z = -\frac{d\Phi}{dz}$  on the axis, can be expressed.

$$E_{z,int}(0, z_0) = -\frac{\rho}{2\epsilon_0} [-2z_0 + \frac{1}{2} (\frac{a^2 + 2(z_0 + b)^2}{\sqrt{(z_0 + b)^2 + a^2}} - \frac{a^2 + 2(z_0 - b)^2}{\sqrt{(z_0 - b)^2 + a^2}})] \quad (4.9)$$

$$E_{z,ext}(0, z_0) = -\frac{\rho}{2\epsilon_0} [-2b \operatorname{sign}(z_0) + \frac{1}{2} (\frac{a^2 + 2(z_0 + b)^2}{\sqrt{(z_0 + b)^2 + a^2}} - \frac{a^2 + 2(z_0 - b)^2}{\sqrt{(z_0 - b)^2 + a^2}})] \quad (4.10)$$

The length of the cylinder is 1 mm and the radius 0.5 mm. The charge  $-100$  pC and the radius 0.5 mm. With initially  $E_z = 0V/m$  and with 10'000 macroparticles The same calculations as the sphere were made in the concept

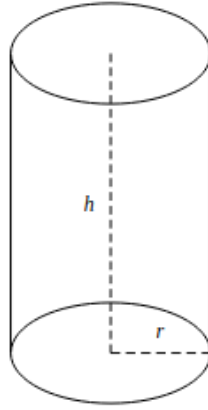


**Figure 4.8:** The cylinder

of the cylindrical distribution. The agreement is very good both between the numerical and analytical solution and the simulations from RF-Track.

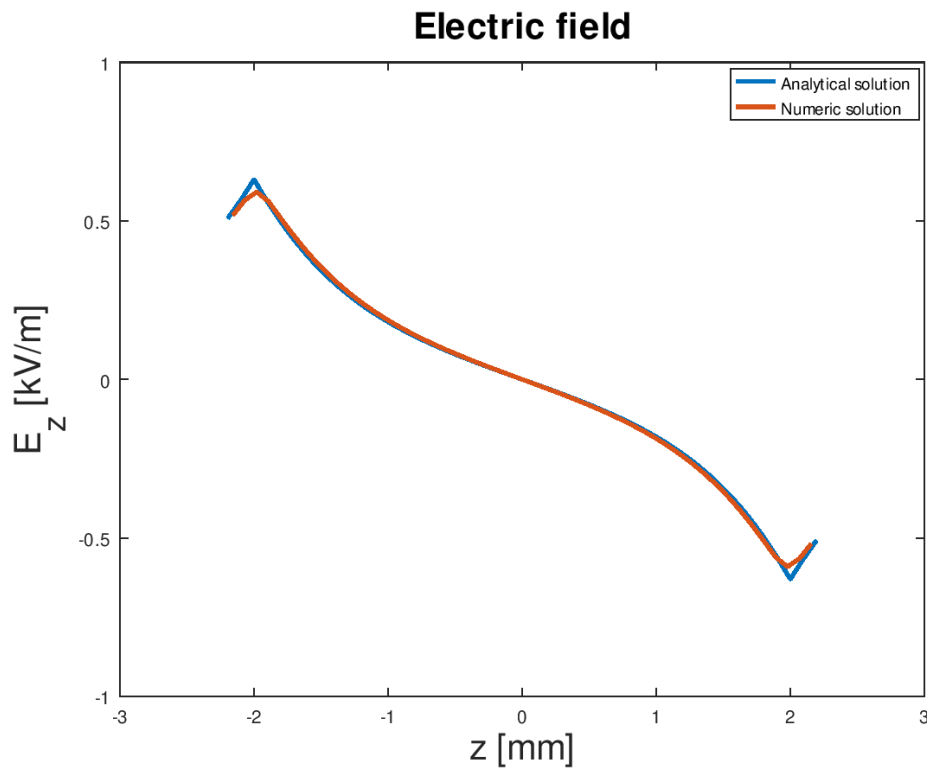


**Figure 4.9:** The comparison of the electric field between the analytical (blue line) and the numerical solution with the green function (red line), in Octave.

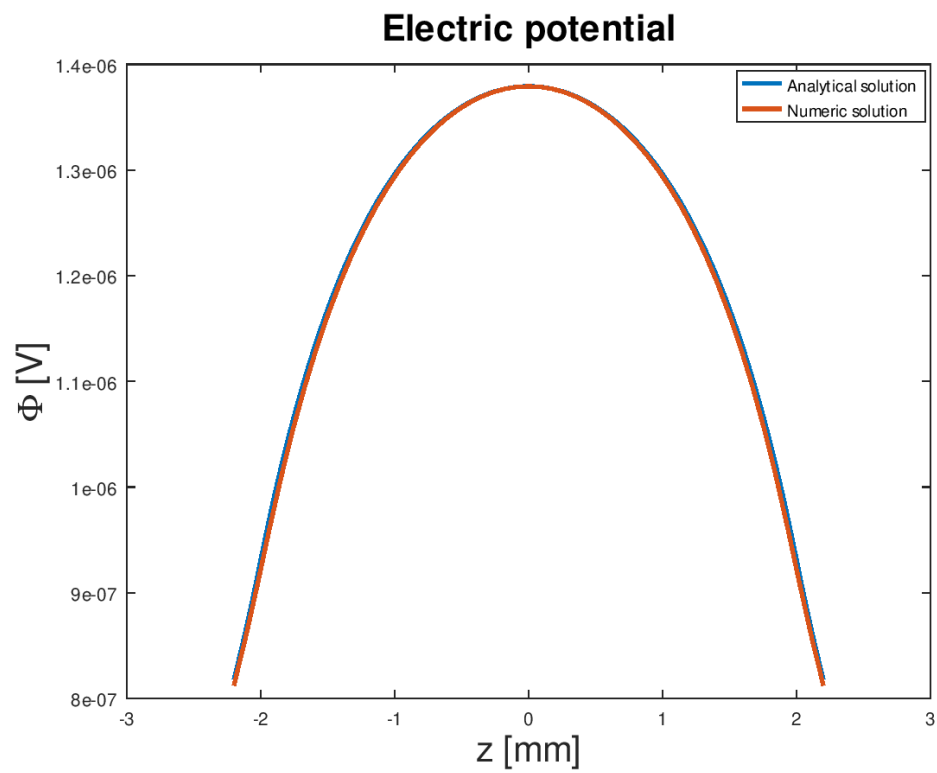


**Figure 4.10:** The comparison of the electric potential between the analytical (blue line) and the numerical solution with the green function (red line), in Octave.



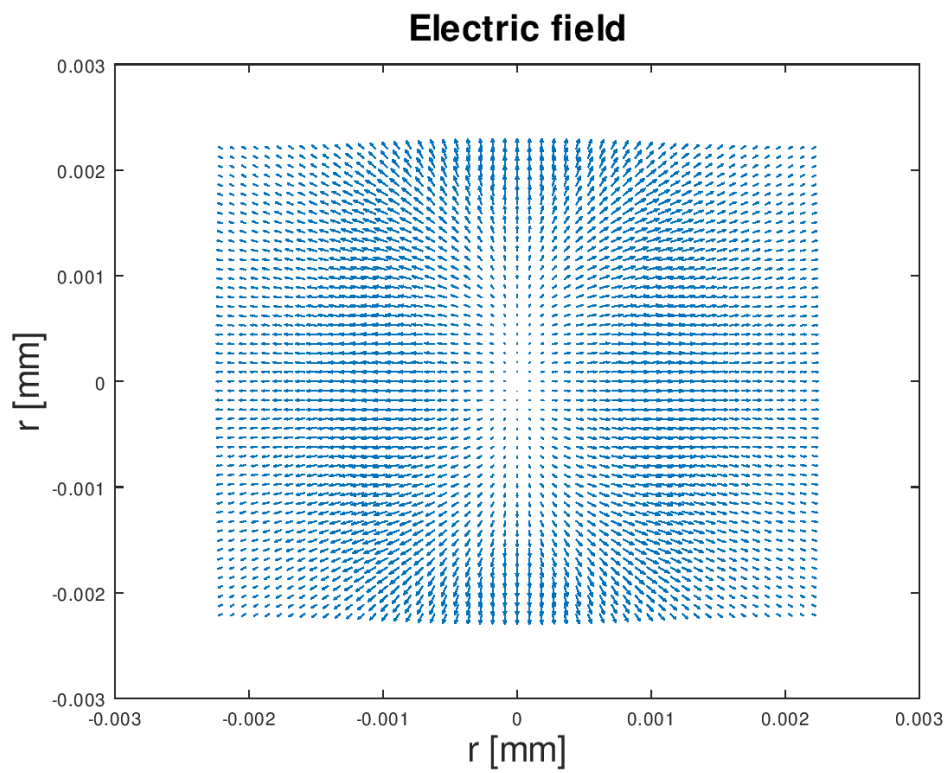


**Figure 4.11:** The electric field in the cylinder, in Octave.

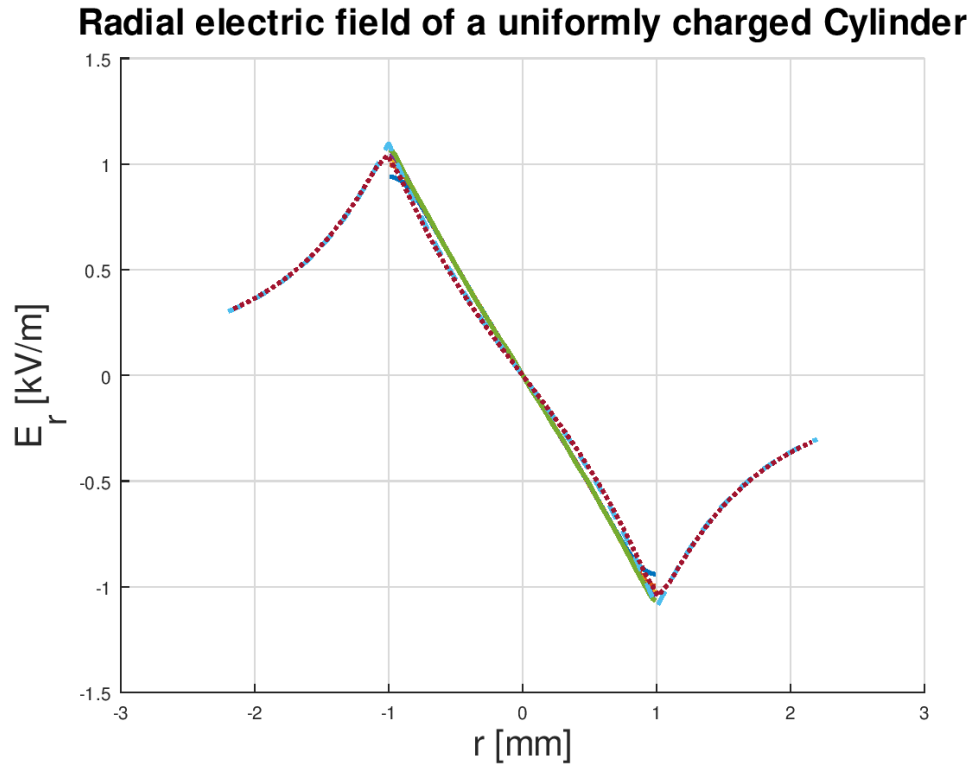


**Figure 4.12:** The comparison of the electric field in one plot of the analytical and numerical solution in Octave and the simulation in RF-Track. The dashed line is the analytical solution. The dotted line is the numerical solution and the solid lines are the simulations from RF-Track, for different PIC. In this plot there are PIC  $32 \times 32 \times 32$ , PIC  $48 \times 48 \times 48$ , PIC  $64 \times 64 \times 64$ , PIC  $128 \times 128 \times 128$ .

Since ASTRA cannot simulate particles at rest in the case of the cylindrical distribution, the calculations were made at this between ASTRA and RF-Track in Ez.

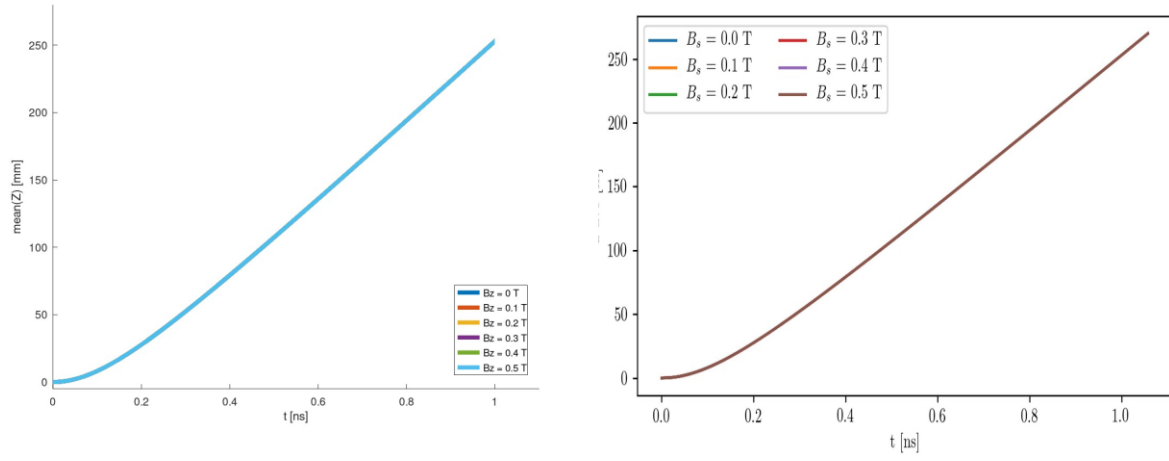


**Figure 4.13:** The comparison between RFT and ASTRA (from Luke Aidan Dyks, CERN) for  $E_z = -10 \text{ MV/m}$  and  $B_z$  scan:  $\text{mean}(Z)$

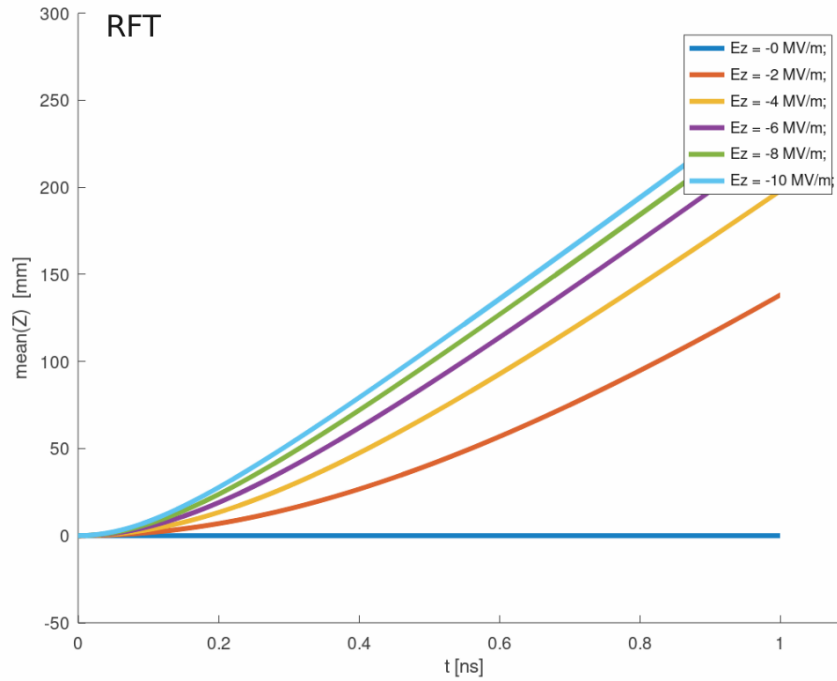


**Figure 4.14:** The  $E_z$  scan:  $\text{std}(Z)$

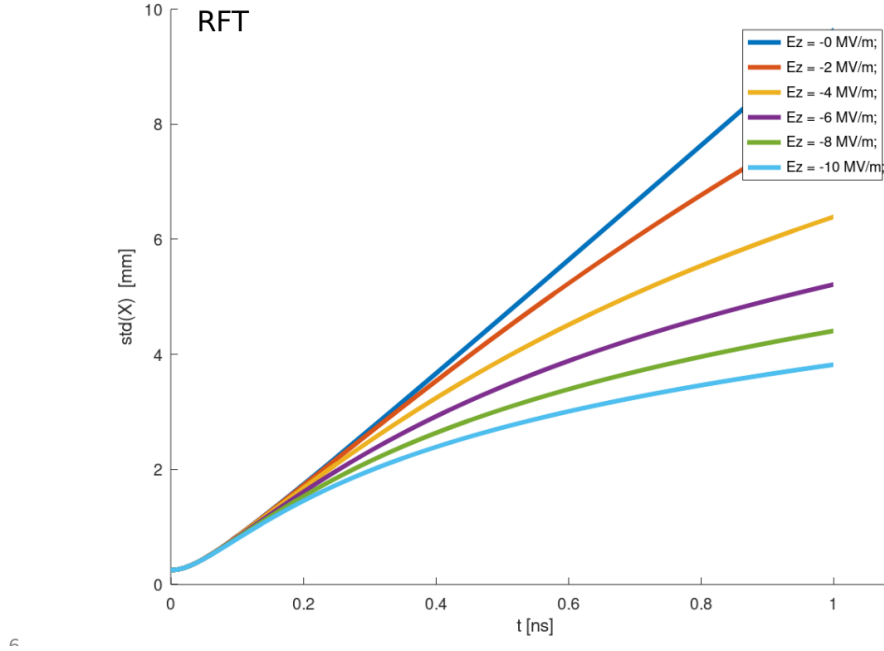


**Figure 4.15:** The  $E_z$  scan:  $\text{std}(X)$

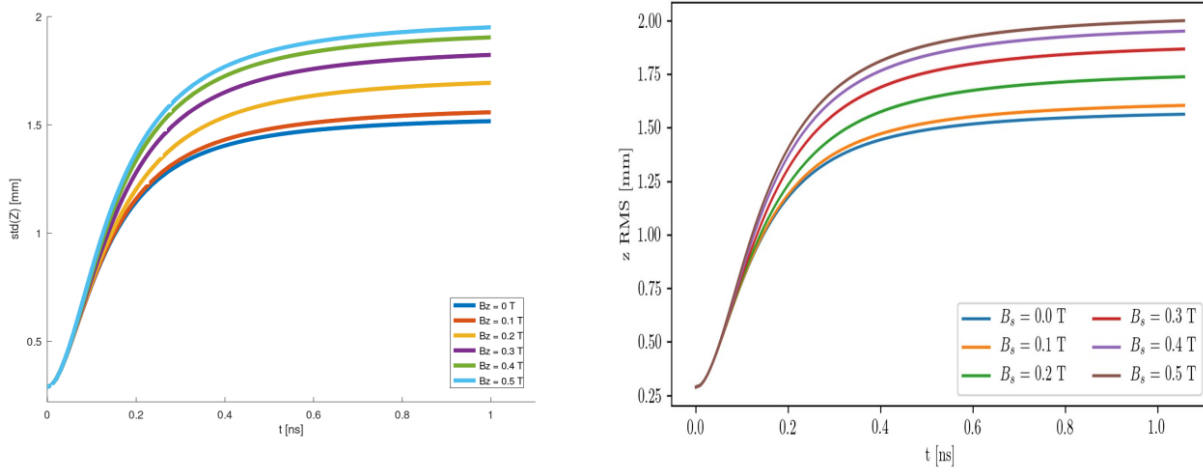


**Figure 4.16:** The comparison between RFT (left) and ASTRA (right) (from Luke Aidan Dyks, CERN) for  $E_z = -10$  MV/m and  $B_z$  scan:  $\text{std}(X)$ .

# Chapter 5

## Conclusions

RF-Track is a very powerful tool which is flexible and offers more than valid results. In the case of FFT calculations the simulation time of ASTRA is 342 sec while RF-track is only 104 sec. It is proved that is faster than ASTRA. This thesis is a good reference for someone to understand the calculation of space charge forces, a concept that is important for the study of accelerator physics. The implementation of the green function in Octave was a task, which was not only very interesting, but also very important for the validation of the codes.

## 5. Conclusions

---

# Bibliography

- [1] William Bober. Numerical and Analytical Methods with MATLAB. CERN 64-09. CERN.
- [2] CM. Ferrario, M. Migliorati, and L. Palumbo. Space Charge Effects. 2014.
- [3] DANIEL FLEISCH. A Student's Guide to Maxwell's Equations. 2008.
- [4] Randy J. Jost Karl E. Lonngren Sava V. Savov. Fundamentals of Electromagnetics with MATLAB.
- [5] ASTRA Manual Klaus Floettmann. DOI: <https://accelconf.web.cern.ch/e06/PAPERS/WEPOCH121.PDF>.
- [6] Andrea Latina. *RF-Track code and documentation*.
- [7] Andrea Latina. *RF-Track Reference Manual*. Tech. rep. Geneva, Switzerland: CERN, 2020. DOI: [10.5281/zenodo.3887085](https://doi.org/10.5281/zenodo.3887085).
- [8] Adrian OEFTIGER. Space Charge Effects and Advanced Modelling for CERN Low Energy Machines. 2016.
- [9] Justin Owen. *Simulation of Electron Beam Dynamics in the 22 MeV Accelerator for a Coherent Electron Cooling Proof of Principle Experiment*. 2013.
- [10] Raymond John Protheroe. Essential Electromagnetism. CERN 64-09. CERN.
- [11] Rodion Tikhoplav. Low Emittance Electron Beam Studies. CERN 64-09. CERN.

- 
- [12] CompactLight Website. DOI: <https://www.compactlight.eu/Main/HomePage>.
- [13] John A. Buck William H. Hayt. Engineering Electromagnetics. CERN 64-09. CERN.

[6] [3] [8] [9] [4] [3] [1] [11] [10] [10] [13]



## PART II



# Contents

<b>1</b>	<b>CERN accelerator complex</b>	<b>69</b>
1.1	General . . . . .	69
1.2	Particle accelerators and detectors . . . . .	70
1.3	CERN accelerator complex . . . . .	73
1.4	LHC . . . . .	75
<b>2</b>	<b>East Area</b>	<b>79</b>
2.1	Proton Synchrotron . . . . .	79
2.2	East Area . . . . .	81
2.3	CHARM . . . . .	84
<b>3</b>	<b>CHARM facility</b>	<b>85</b>
3.1	General . . . . .	85
3.2	Layout and operational parameters . . . . .	88
3.3	Beam parameters and instrumentation . . . . .	91
3.3.1	Beam specification . . . . .	91
3.3.2	Beam position and monitoring . . . . .	91
3.3.3	Beam intensity monitoring . . . . .	92
3.4	Targets . . . . .	94
3.5	Radiation fields . . . . .	95
3.6	Radiation protection assessment approach . . . . .	96
3.6.1	Prompt radiation . . . . .	96
3.6.2	Residual radiation . . . . .	97
3.6.3	Air activation and subsequent release to the environment	99

---

<b>4</b>	<b>Neutron attenuation and activation</b>	<b>101</b>
4.1	General . . . . .	101
4.1.1	Atoms and energy . . . . .	101
4.1.2	Nuclide Chart . . . . .	103
4.1.3	Discoveries in Radiation Physics . . . . .	103
4.1.4	Basic properties of the neutron . . . . .	105
4.2	Nuclear reactions . . . . .	111
4.3	Neutron interactions . . . . .	112
4.3.1	Neutron cross section . . . . .	114
4.4	Neutron attenuation . . . . .	124
4.5	Neutron activation . . . . .	125
4.5.1	Properties of induced radioactivity . . . . .	125
4.5.2	Estimation of induced radioactivity . . . . .	126
<b>5</b>	<b>FLUKA &amp; Dorian Code</b>	<b>131</b>
5.1	Monte Carlo method . . . . .	131
5.2	The FLUKA code . . . . .	138
5.2.1	Physical models and features . . . . .	139
5.2.2	Biasing . . . . .	141
5.2.3	Scoring . . . . .	142
5.3	The DORIAN code . . . . .	144
5.3.1	Calculation of residual dose rates . . . . .	144
5.3.2	Verification . . . . .	148
5.3.3	Advanced applications . . . . .	148
5.3.4	Implementation . . . . .	151
<b>6</b>	<b>Residual ambient dose equivalent rate measurements</b>	<b>153</b>
<b>7</b>	<b>Simulation setup</b>	<b>163</b>
<b>8</b>	<b>Comparison of simulations and measurements</b>	<b>171</b>
<b>9</b>	<b>Summary and Conclusions</b>	<b>177</b>

# Chapter 1

## CERN accelerator complex

### 1.1 General

The first decision regarding the establishment of a European Council for Nuclear Research (in French Conseil Européen pour la Recherche Nucléaire) was first made at an intergovernmental meeting of UNESCO in Paris in December 1951. CERN is now the European Organization for Nuclear Research. The CERN laboratory is located astride the Franco-Swiss border near by Geneva and it is considered one of the world's largest and most respected centers for scientific research and it was one of Europe's first joint ventures. Now CERN has 22 Member states and currently there are 2300 staff, 1620 paid personnel and 10500 users from all over the world. CERN's primary research is in fundamental particle physics finding out what the universe is made of and how it works. The laboratory also plays an important role in developing the technologies of the future. Using particle accelerators and detectors, it studies the basic constituents of matter, the fundamental particles. Accelerators boost beams of particles to high energies before they are made to collide with each other or with stationary targets. Detectors observe and record the results of these collisions. [\[38\]](#) The process gives us clues about how the particles interact, and provides insights into the fundamental laws of nature.

## 1.2 Particle accelerators and detectors

Accelerators at CERN boost particles to high energies before they are made to collide inside detectors. The detectors determine the identity of particles, by characterizing their speed, mass and charge. This process requires accelerators, powerful electromagnets, and layer upon layer of complex subdetectors. Particles that are produced in collisions normally travel in straight lines, but applying magnetic field their paths become curved. Electromagnets around particle detectors generate magnetic fields to make this effect happen. Through this procedure we can calculate the momentum of from the curvature of its path. Modern particle detectors consist of layers of subdetectors, each one is designed to look for particular properties, or specific types of particle. Tracking devices reveal the path of electrically charged particles as they pass through and interact with suitable substances and calorimeters stop, absorb and measure the particle's energy. Electromagnetic calorimeters measure the energy of electrons, positrons and photons. Hadronic calorimeters sample the energy. Calorimeters can stop most known particles except muons and neutrinos. There are two further methods in order to find the identity of a particle. Both methods work by detecting radiation emitted from charged particles. When a charged particle travels faster than light does through a given medium, it emits Cherenkov radiation at an angle that depends on its velocity. The particle's velocity can be calculated from this angle. Velocity can then be combined with a measure of the particle's momentum to determine its mass and so its identity. When a fast charged particle crosses the boundary between two electrical insulators with different resistances to electric currents, it emits transition radiation. The phenomenon is related to the energy of the particle and so can distinguish different particle types. Combining all these data we can understand what was in the detector at the moment of a collision. The next step is to scour the collisions for unusual particles, or for results that do not fit current theories. When the particle beams enter the detectors, insertion magnets take over. Particles must be squeezed closer together before they enter a detector so

that they collide with particles coming from the opposite direction. Three quadrupoles are used to create a system called an inner triplet. There are eight inner triplets, two of which are located at each of the four large LHC detectors, ALICE, ATLAS, CMS and LHCb.

At CERN in LHC, there are thousands of lattice magnets that bend and tighten the particles trajectory. They are responsible for keeping the beams stable and precisely aligned. Dipole magnets are one of the most complex parts of the LHC. These magnets used to bend the paths of the particles. There are 1232 main dipoles, each 15 meters long and weighing 35 tons. Powerful magnetic fields generated by the dipole magnets allow the beam to handle tighter turns. When particles are bunched together, they are more likely to collide in greater numbers when they reach the LHC detectors. Quadrupoles help to keep the particles in a tight beam. They have four magnetic poles arranged symmetrically around the beam pipe to squeeze the beam either vertically or horizontally. In addition there are sextupole, octupole and decapole magnets, which correct for small imperfections in the magnetic field at the extremities of the dipoles. After the beams collide in the detector, enormous magnets aid the measurement of particles. Other magnets minimize the spread of the particles from the collisions. When it is time to dispose of the particles, they are deflected from the LHC along a straight line towards the two beam dumps. A "dilution" magnet reduces the beam intensity by a factor of 100,000 before the beam collides with a block of concrete and graphite composite for its final stop. Insertion magnets are also responsible for beam cleaning, which ensures that stray particles do not come in contact with the LHC's most sensitive components. Luminosity is an important indicator of the performance of an accelerator. The higher the luminosity, the more data the experiments can gather to allow them to observe rare processes. It gives a measure of how many collisions are happening in a particle accelerator. To accelerate particles, the accelerators are fitted with metallic chambers containing an electromagnetic field known as radiofrequency (RF) cavities. Charged particles injected into this field

receive an electrical impulse that accelerates them.[20]

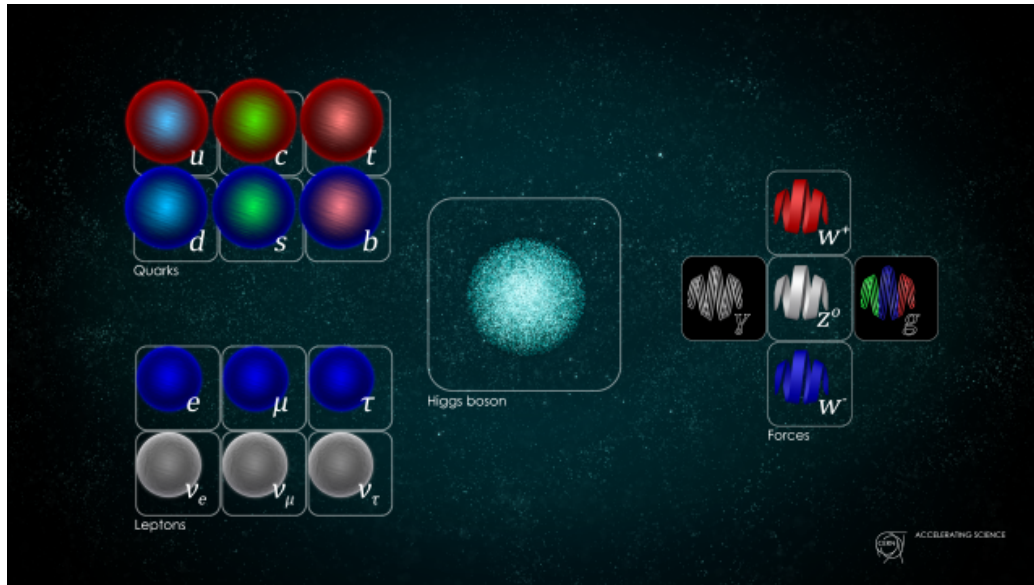


**Figure 1.1:** The Standard Model of particle physics. The W, Z and Higgs bosons were discovered at CERN.



### 1.3 CERN accelerator complex

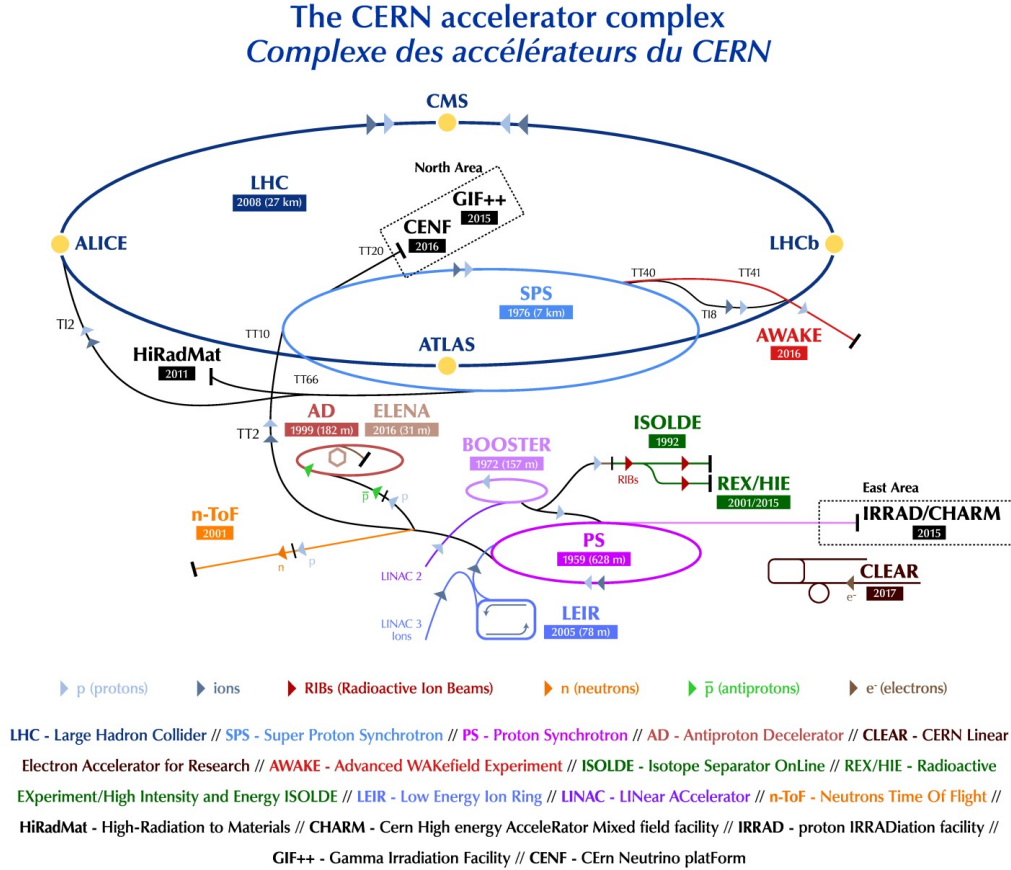


**Figure 1.2:** CERN accelerator complex

The accelerator complex at CERN is a succession of machines that accelerate particles to increasingly higher energies. Each machine from the sequence boosts the energy of a beam of particles, before injecting the beam into the next machine. The last element in this chain is the Large Hadron Collider (LHC). Proton beams are accelerated up to the record energy of 6.5 TeV per beam. The other accelerators in that succession chain use beams for experiments at lower energies. All proton beams start with a proton source. The proton source is a bottle of hydrogen gas. An electric field is used to strip hydrogen atoms of their electrons to yield protons. Linac 2

is the first accelerator in the chain, accelerates the protons to the energy of 50 MeV. The beam is then injected into the Proton Synchrotron Booster (PSB), which accelerates the protons to 1.4 GeV, followed by the Proton Synchrotron (PS), which pushes the beam to 25 GeV. Protons are then sent to the Super Proton Synchrotron (SPS) where they are accelerated to 450 GeV. The protons are finally transferred to the two beam pipes of the LHC. The beam in one pipe circulates clockwise while the beam in the other pipe circulates anticlockwise. The duration to fill each LHC ring is 4 minutes and 20 and 20 minutes for the protons to reach their maximum energy of 6.5 TeV. Beams circulate for many hours inside the LHC beam pipes under normal operating conditions. The two beams are brought into collision inside four detectors. ALICE, ATLAS, CMS and LHCb are these detectors and the total energy at the collision point is equal to 13 TeV. The accelerator complex includes also the Antiproton Decelerator and the Online Isotope Mass Separator (ISOLDE) facility, and the Compact Linear Collider test area and the neutron time-of-flight facility (nTOF). It also previously fed the CERN Neutrinos to Gran Sasso (CNGS) project. In LHC does not accelerated only protons. Lead ions for the LHC start from a source of vaporised lead and enter Linac 3 before are being collected and accelerated in the Low Energy Ion Ring (LEIR). They then follow the same route to maximum energy as the protons. There are also fixed-target experiments. A beam of accelerated particles is directed at a solid, liquid or gas target, which itself can be part of the detection system. COMPASS, which looks at the structure of hadrons, uses beams from the Super Proton Synchrotron (SPS). NA61/SHINE studies the properties of hadrons in collisions of beam particles with fixed targets. NA62 uses protons from the SPS to study rare decays of kaons. The CLOUD experiment is investigating a possible link between cosmic rays and cloud formation. ACE, AEGIS, ALPHA, ASACUSA, and ATRAP all use antiprotons from the Antiproton Decelerator.[\[20\]](#)

## 1.4 LHC

As it is referred below, the Large Hadron Collider (LHC) is the world's largest and most powerful particle accelerator. It first started up on 10 September 2008, and it is the latest addition to CERN's accelerator complex. The LHC consists of a 27-kilometer ring of superconducting magnets with a number of accelerating structures to boost the energy of the particles along the way. The beams inside the LHC are made to collide at four locations around the accelerator ring, corresponding to the positions of four particle detectors. These four points are ATLAS, CMS, ALICE and LHCb. ATLAS and CMS, use detectors to investigate the largest range of physics possible. ALICE and LHCb have detectors specialized for focusing on specific phenomena. These four detectors are located underground in huge caverns on the LHC ring. The smallest experiments on the LHC are TOTEM and LHCf, which focus on protons or heavy ions that brush past each other rather than meeting head on when the beams collide. MoEDAL uses detectors deployed near LHCb to search for a hypothetical particle called the magnetic monopole.

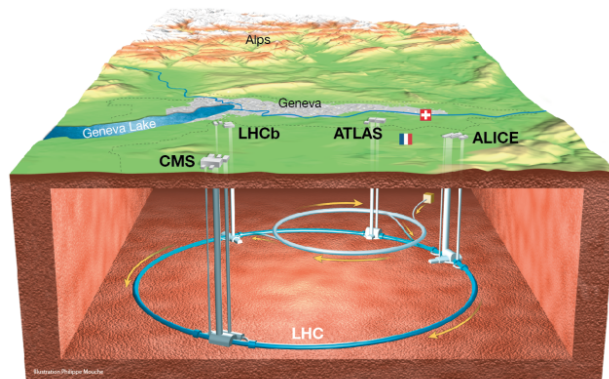


**Figure 1.3:** Overall view of the LHC. View of the 4 LHC detectors: ALICE, ATLAS, CMS and LHCb.

The Large Hadron Collider (LHC) is currently operating at the energy of 6.5 TeV per beam. At this energy, the trillions of particles circle the collider's

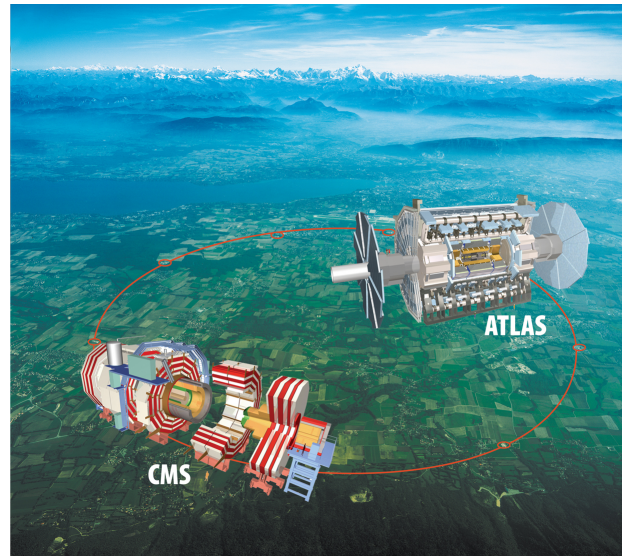


**Figure 1.4:** CMS and ATLAS experiment in Geneva area.

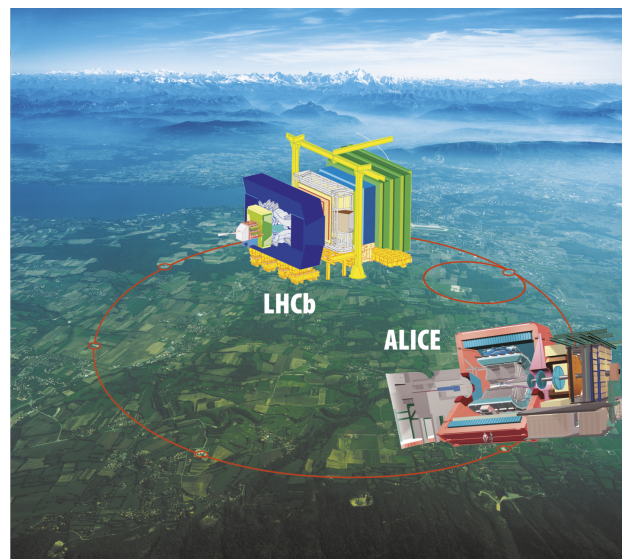


**Figure 1.5:** LHCb and ALICE experiment in Geneva area.

27-kilometre tunnel 11.245 times per second. More than 50 types of magnets are needed to send them along complex paths. All the magnets on the LHC are electromagnets. The main dipoles generate powerful 8.3 Tesla magnetic fields, more than 100.000 times more powerful than the Earth's magnetic field. The electromagnets use a current of 11.080 amperes to produce the

field, and a superconducting coil allows the high currents to flow without losing any energy to electrical resistance.

ATLAS is one of two detectors at the Large Hadron Collider (LHC). It investigates a wide range of physics, from the search for the Higgs boson to extra dimensions and particles that could make up dark matter. Beams of particles from the LHC collide at the center of the ATLAS detector making collision debris in the form of new particles, which fly out from the collision point in all directions. Six different detecting subsystems arranged in layers around the collision point record the paths, momentum, and energy of the particles, allowing them to be individually identified. A huge magnet system bends the paths of charged particles so that their momenta can be measured. The interactions in the ATLAS detectors create an enormous flow of data. To digest the data, ATLAS uses an advanced “trigger” system to tell the detector which events to record and which to ignore. Complex data-acquisition and computing systems are then used to analyze the collision events recorded. At 46 m long, 25 m high and 25 m wide, the 7000-tonne ATLAS detector is the largest volume particle detector ever constructed. It sits in a cavern 100 m below ground near the main CERN site, close to the village of Meyrin in Switzerland. [12] The Compact Muon Solenoid (CMS) is the other detector in LHC, who has general purpose like ATLAS. Studying from the Standard Model to searching for extra dimensions. It uses different technical solutions and a different magnet-system design than ATLAS. The CMS detector is built around a huge solenoid magnet. This takes the form of a cylindrical coil of superconducting cable that generates a field of 4 tesla. The field is confined by a steel “yoke” that forms the bulk of the detector’s 14,000-tonne weight. CMS detector was constructed in 15 sections at ground level before being lowered into an underground cavern near Cessy in France and reassembled. The complete detector is 21 metres long, 15 meters wide and 15 meters high. [15] ALICE (A Large Ion Collider Experiment) is a heavy-ion detector in the Large Hadron Collider (LHC) ring. It is designed to study the physics of strongly interacting matter at extreme energy densities, where a phase

of matter called quark-gluon plasma forms. The existence of plasma phase and its properties are key issues in the theory of quantum chromodynamics (QCD), for understanding the phenomenon of confinement, and for a physics problem called chiral-symmetry restoration. The ALICE collaboration uses the 10,000-tonne ALICE detector – 26 m long, 16 m high, and 16 m wide – to study quark-gluon plasma. The detector sits in a vast cavern 56 m below ground close to the village of Saint Genis Pouilly in France, receiving beams from the LHC. [11] The Large Hadron Collider beauty (LHCb) experiment specializes in investigating the slight differences between matter and antimatter by studying a type of particle called the "beauty quark", or "b quark". Instead of surrounding the entire collision point with an enclosed detector as do ATLAS and CMS, the LHCb experiment uses a series of subdetectors to detect mainly forward particles - those thrown forwards by the collision in one direction. The first subdetector is mounted close to the collision point, with the others following one behind the other over a length of 20 metres. To identify the b quarks, LHCb has developed sophisticated movable tracking detectors close to the path of the beams circling in the LHC. The LHCb detector is 5600 tonnes and made up of a forward spectrometer and planar detectors. It is 21 meters long, 10 meters high and 13 meters wide, and it is located 100 meters below ground near the village of Ferney-Voltaire in France. [37]



# Chapter 2

## East Area

### 2.1 Proton Synchrotron

The Proton Synchrotron (PS) is an important part of CERN's accelerator complex. It usually accelerates either protons delivered by the Proton Synchrotron Booster (PSB) or heavy ions from the Low Energy Ion Ring (LEIR). The PS was the first synchrotron at CERN. It first accelerated protons on 24 November 1959 and it became for a brief period the world's highest energy particle accelerator. When CERN start at building new accelerators in 1970's, the PS's main role was to supply particles to the new machines. Through the years it came through plenty of modifications and upgrades and the beam intensity of its proton beam has increased by several order of magnitude. It has a circumference of 628 meters and 277 conventional (room-temperature) electromagnets, including 100 dipoles to bend the beams round the ring. The accelerator can reach up to 25 GeV and has several extraction lines, such as the F16 line to the SPS, to the AD, to the nToF and the F61 line to the East Hall through the F61 beam line. In the East Hall are located the Proton Irradiation Facility (IRRAD) and the CERN High energy AcceleRator Mixed eld facility (CHARM) and they receive a proton beam with 24 GeV/c momentum. [\[54\]](#), [\[53\]](#), [\[35\]](#), [\[54\]](#), [\[18\]](#), [\[52\]](#).

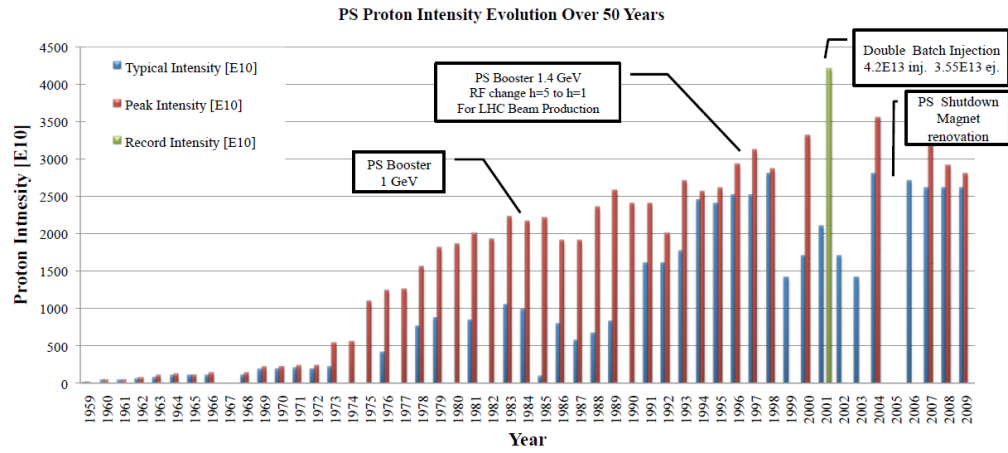


**Figure 2.1:** PS Proton intensity evolution over 50 years

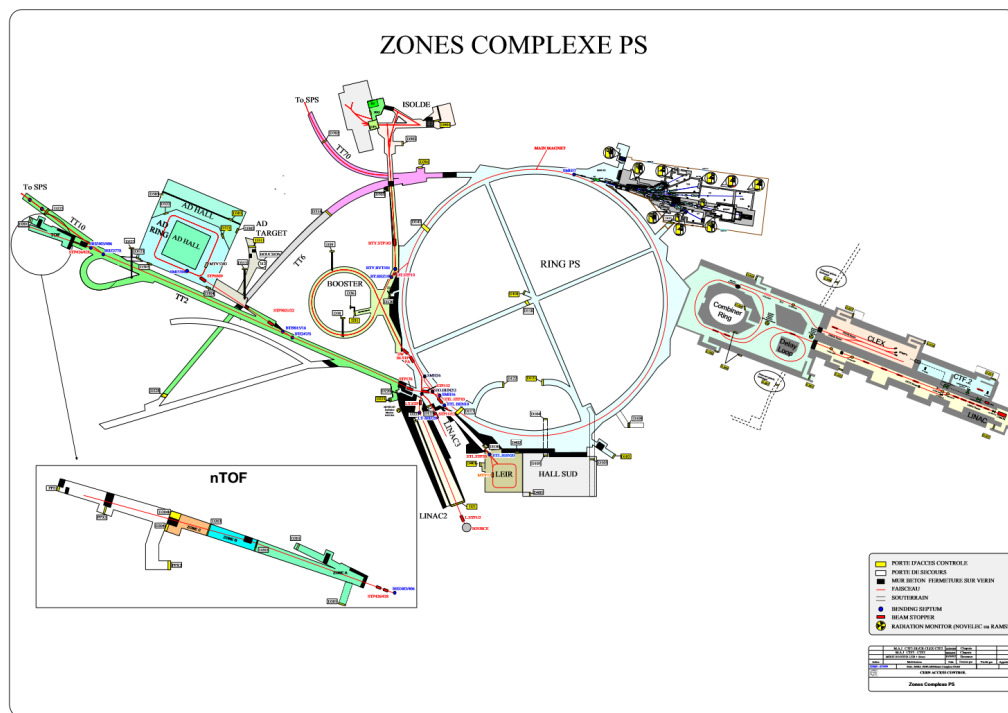


**Figure 2.2:** Zones Complexe PS



## 2.2 East Area

The East Area is an experimental area at the PS, located in building 157. It contains four beam lines: T8, T9, T10 and T11. As we told before, the beam lines are derived from the 24 GeV/c primary beam from the PS, which provides 1.2 second long cycles with extraction at flat top of about 400 msec. This extraction line is then split to the F61N (North) line towards the north target and to the F61S (South) line. For the North target we have the T9, T10 and T11 secondary beamline and the F615 beamline becomes the T8 beamline. The number of East Area cycles per supercycle depends on schedule constraints. Each cycle has a flat top of about 400 msec, with uniform time distribution.

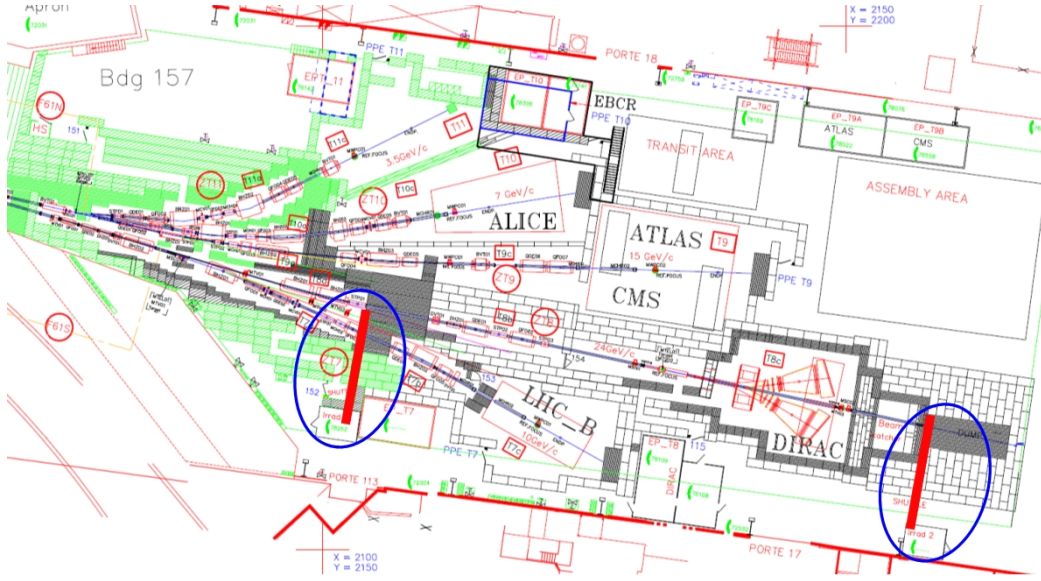


**Figure 2.3:** The geometry of east area

The T8 beam line is a primary beam line that transports the primary protons to the IRRAD and CHARM facilities with a 24 GeV/c beam momentum and where they finally impinge on the CHARM target. The T9 beam is a secondary beam that delivers secondary particles up to 15 GeV/c at a production angle of 0 degrees. The T10 beam is a secondary beam that delivers secondary particles up to 7 GeV/c at a production angle of 61.6 milliradians.

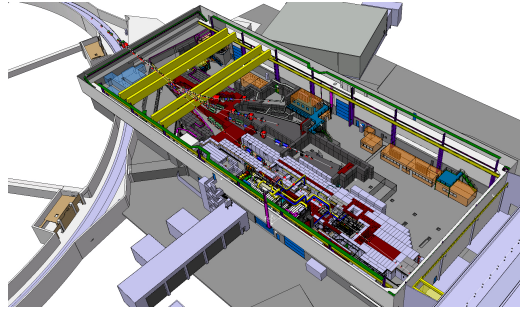


**Figure 2.4:** The 3D geometry of East Area

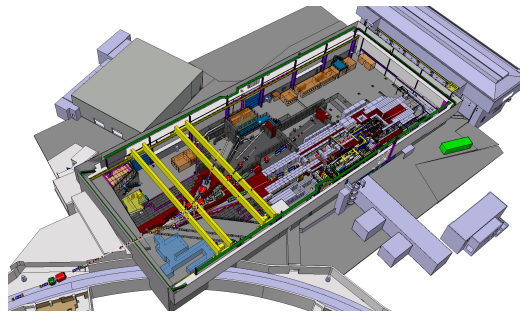


**Figure 2.5:** The 3D geometry of the East Area

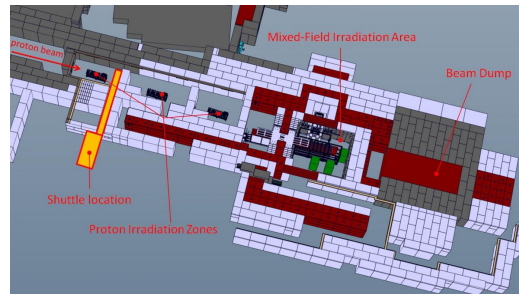


**Figure 2.6:** The CHARM facility

The T10 beam is a secondary beam that delivers secondary particles up to 7 GeV/c at a production angle of 61.6 milliradians. [59], [65]



**Figure 2.7:** The geometry of the East Area

## 2.3 CHARM

CHARM (CERN High energy AcceleRator Mixed field facility) has been built at CERN in the Proton Synchrotron (PS) east area. The facility scope is to assess radiation effects on electronics not only at component level but also at system level within particle accelerator representative environments. Its available radiation fields are also characteristics for ground and atmospheric environments (neutron energy spectra) as well as for space environments (representative for the inner proton radiation belt). The size of the available test area is such that large objects can also be irradiated. The target area is large enough to host a complete accelerator control or powering system (e. g for LHC power converters) but also full satellites, and parts of cars or planes. In addition it is possible to irradiate electronic systems in highly representative conditions, including with operational power and control systems. [\[1\]](#)

# Chapter 3

## CHARM facility

### 3.1 General

CHARM (CERN High energy AcceleRator Mixed field) is a unique testing facility in the East Area, that receives beam from CERN Proton Synchrotron (PS). It provides teams with a venue to test their equipment in radiation environments similar to those in the accelerator complex. More specific, this facility is used to assess radiation effects on electronics both at component level and system level within particle accelerator representative environments. Moreover its available radiation fields are characteristics not only for ground and atmospheric environments (neutron energy spectra) but also for space environments (representative for the inner proton radiation belt). The target area is large enough to host a complete accelerator control or powering system, for instance like LHC power converters, but also full satellites, and parts of cars or planes. Its well-known mixed radiation elds at different irradiation locations allow to study the effects of radiation on the equipment in the frame of the R2E project. The R2E project was created in 2011 after marking major downtime of the CERN LHC, consequently of Single Event Effects (SEE) in electronic equipment in the LHC tunnel that launched the dumping of the beams in LHC. To achieve the goal of R2E project of 0.5 SEE induced beam dumps per 1 inverse femtobarn of

integrated luminosity delivered to ATLAS and CMS in 2015 after the Long Shutdown 1 (LS1), see figure 3.1, a thorough test campaign of electronic equipment, that was installed in the LHC tunnel, was needed. Therefore the CHARM facility was built in LS1(2013-2014), to be able to test electronic systems, as we mentioned before, with dimensions of up to 1 m x 1 m x 2 m. [23]

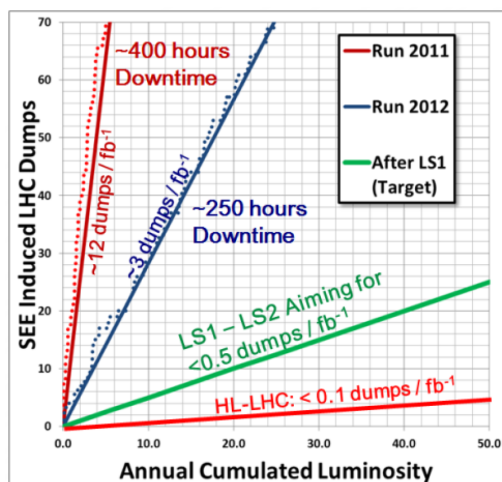


Figure 3.1

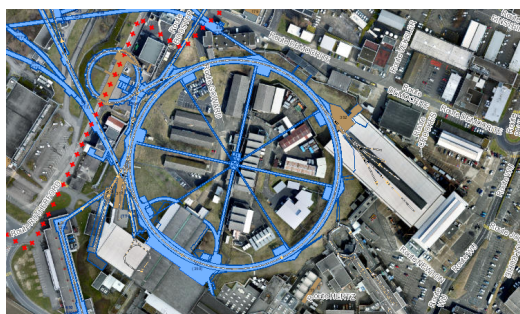


Figure 3.2: The PS from the map of CERN



**Figure 3.3:** Horizontal integration drawing of the CHARM facility at beam line level.

## **3.2 Layout and operational parameters**

The CHARM facility is located in one of the experimental halls at CERN. In order to be able to reduce at maximum the radiation outside of the shielding structure the surrounding layout of CHARM is composed of iron and concrete blocks. In the figures 2.4 and 2.6 is appeared a 3D view of the facility and a horizontal cut of the inner target chamber. As someone can see the target chamber is large enough to host bulky and complete systems, like satellites since around 70 m<sup>3</sup> of space are available for radiation tests. The 24 GeV/c proton beam is extracted from the Proton Synchrotron (PS) accelerator and impacts on a cylindrical copper or aluminium target. The created secondary radiation field is used to test electronic equipment installed at predefined test positions. For the primary beam target choices are used copper and aluminium as material choices, because of their mechanical and thermal properties. Moreover together with the mobile shielding configuration they also allow the creation of a secondary particle spectra representative for the source term of those present in the atmospheric, space and accelerators environments. To model and choose between the various representative spectra, different shielding configurations are thus available in the facility. There are four movable layers of an individual thickness of 20 cm made out of concrete and iron. These shielding walls can be placed between the target and the test locations in different combinations, thus allowing to modulate the test spectra and adopt them as closely as possible to the radiation field (energy and intensity) aimed for during the tests. The shielding plates are motorized with remote control. The intensity of the radiation field can be modulated by varying the primary beam intensity, the choice of target head, e.g. two massive ones (Al or Cu – the yield of the massive Al target is about 2.5 times smaller than for the massive Cu target) or one with reduced effective density (Al target with holes – it gives an additional reduction by a factor 4), allowing for an overall reduction factor (including beam intensity reduction) of the primary radiation field of 10-100 in total. The surrounding layout of the CHARM facility is composed of iron and concrete blocks in order to re-



duce at ultimate the radiation outside of the shielding structure to optimized levels. The CHARM facility receives the proton beam from the CERN PS through the F61S and then the T8 beam-line in the PS East Experimental Area. The beam crosses first IRRAD, a direct proton irradiation facility that is upstream of CHARM and then impacts on the CHARM target. The beam that comes from the PS has a momentum of 24 GeV/c with up to  $5 \times 10^{11}$  protons per pulse with a pulse length of 350 ns and with a maximum average beam intensity of  $6.7 \times 10^{10}$  p/s. [2] The shielding walls will be analysed in the next chapters. In the facility there is also an alcove, that can be closed or open with the target inside or outside.[1]



**Figure 3.4:** Inside the CHARM facility, opposite from the shielding walls. In this picture the walls are outside from the facility

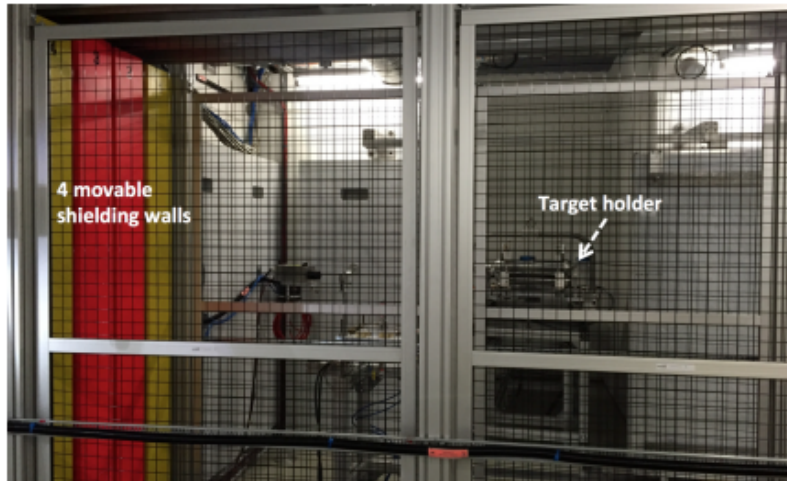


**Figure 3.5:** The 4 movable walls and the target holder



**Figure 3.6:** Inside the CHARM facility

### 3.3 Beam parameters and instrumentation

#### 3.3.1 Beam specification

The CHARM facility receives a pulsed proton beam from the CERN PS with a beam momentum of 24 GeV/c. The ultimate pulse intensity is  $5 \times 10^{11}$  protons per pulse and the beam is structured in pulses with a maximum length of 350 ms. The spills are separated by at least 2.4 seconds. Under nominal operation conditions of the facility, CHARM receives 2 spills per 45.6 seconds and the average proton beam intensity on target is  $2.2 \times 10^{10}$  p/s. When CHARM is the only user of beam cycles in East Experimental Area, there is the possibility to reach up to 6 spills per 45.6 seconds with  $6.7 \times 10^{10}$  p/s highest proton beam intensity on target. [2]

Parameter	Value
Proton beam momentum [GeV/c]	24
Maximum flux per PS spill	$5 \cdot 10^{11}$
Maximum number spills per super cycle	6
Duration of super-cycle [s]	45.6
Maximum number protons per second	$6.7 \cdot 10^{10}$
Maximum number days per year	200
Assumed efficiency	90 per cent
Maximum number of supercycles per year	340.000
Maximum number of protons per year	$1.0 \cdot 10^{18}$
Minimum spot size [mm RMS]	5x5

#### 3.3.2 Beam position and monitoring

Several monitors are used to measure the size and the position of the beam. Some of these monitors are the BPM (Beam Position Monitor) when the beam crosses the IRRAD facility, the BTV (Beam TV) and the MWPC (Multi-wire Proportional Chamber) when it crosses CHARM. The use of MWPC is to check the beam size and the position of the beam and the BTV is

used to control the precision of the beam position after the implementation of changes on the T8 beam line. The values of these monitors are also registered and are available via TIMBER (user interface to the LHC Logging System).

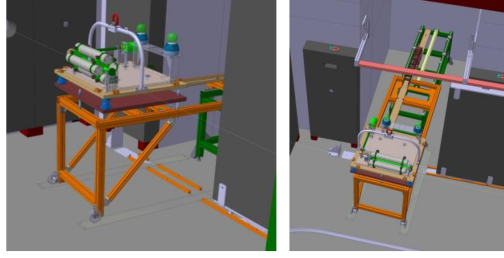


**Figure 3.7:** The target and the target holder

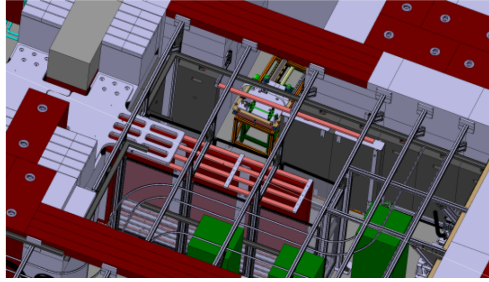


**Figure 3.8:** The CHARM facility

### 3.3.3 Beam intensity monitoring

The beam intensity can be estimated by two Secondary Emission Chambers, denoted SEC1 and SEC2, and as well as by Ionisation Chamber (IC). At the CHARM facility the SEC1 is used to verify the number of protons on the target (POT). The calibration of the SEC1 is done using the 'fast beam current transformer' (BCT) that is located right after the PS extraction point. Furthermore this has been cross checked by foil activation. An intensity calibration factor of  $1.87 \times 10^7$  p/count has been established for the SEC1 and has to be applied to the counts per pulse to obtain the number

---

of protons per pulse. The SEC2 can be used as well to measure the POT, is not a preferred option because this chamber is located after the IRRAD facility and the secondary radiation from the samples placed in IRRAD can affect the signal of the chamber. The measurement values of SEC1, SEC2 and IC are logged in a database they are accessible via TIMBER. [28],[25] [13], [9], [2], [50], [24].

## 3.4 Targets

There are three different types of targets that can be used in CHARM, a copper, an aluminium and an aluminium sieve target. Moreover, there is the option of having no target in the beam. The 3 targets are placed on a target holder as shown in Figure 3.7. The target holder can move back and into the beamline and can be retracted to the target alcove when there is an access to the facility. One target is chosen at a time based on the requested intensity radiation eld which can vary a factor of 3 among the different targets resulting in a total decrease in the primary radiation eld by a factor of 9. The copper target is the one that gives the highest intensity and the aluminium with sieve the lowest. All the targets are cylinders that are 50 cm long with a diameter of 8 cm.

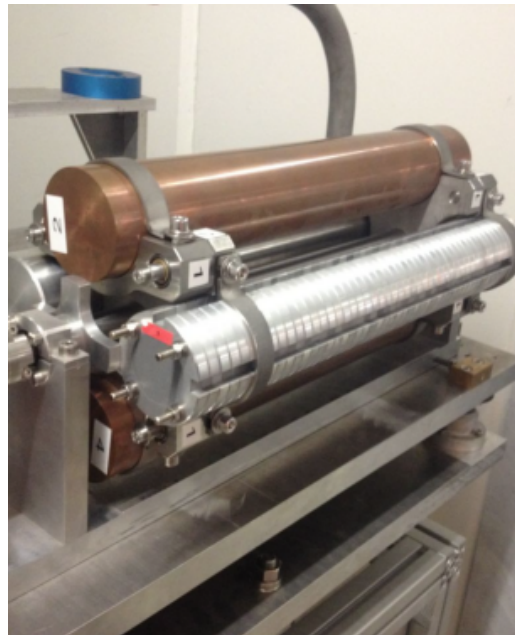


**Figure 3.9:** 2 copper targets and the aluminium with sieve target on the target holder. One of the two copper targets has been currently removed from the target holder.



### 3.5 Radiation fields

The primary proton beam comes from the PS with a 24 GeV/c momentum and impacts on the CHARM target. Then there is a shower of particles that is produced after the beam impinges on the target. These particles are a shower of particles such as protons, neutrons, pions, kaons, electrons, positrons, muons and photons, with large amplitude of energies up to 24 GeV. Because of this fact, the radiation field is called 'mixed' inside the CHARM facility. Furthermore, because of the thick concrete shielding around and top of the facility, the majority of particles that are escaping from the shielding are neutrons, photons, and muons in forward direction. Because of the manifold and alternative modes of operation of this facility, the radiation field occurs to have a large variation in the particle and energy spectra at the various test locations. In order to simulate the radiation fields for different configurations of the facility is used the FLUKA Monte Carlo code, that uses the correct parameters and geometry of the facility. From the results of these simulations the radiation spectra for the test locations are estimated and then used for the calculation of useful quantities referred, for instance to the testing of electronics.

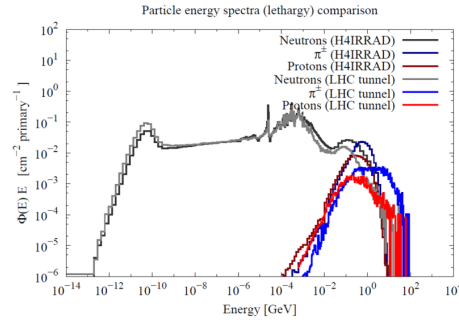


**Figure 3.10:** Particle energy spectra (lethargy) comparison

## 3.6 Radiation protection assessment approach

The radiation protection assessment of the facility can be divided in 3 categories. These categories are the shielding design for the prompt radiation, the optimization of the residual radiation and the activation of air and its subsequent release to the environment.

### 3.6.1 Prompt radiation

The shielding of the CHARM facility has been design to respect the CERN radiological area classification. This implies that the ambient dose equivalent rates should be below 3  $\mu\text{Sv/h}$  for the control rooms inside the East Hall and less than 15  $\mu\text{Sv/h}$  (low occupancy area) at 40 cm outside from shielding walls for the maximum average beam intensity of  $6.7\text{E}10$  protons per second. In addition, the ambient dose equivalent rates should be below 2.5  $\mu\text{Sv/h}$  outside of the hall for the maximum average beam intensity. These requirements meant that all shielding passages (access chicanes, ventilation ducts, cable ducts) had to be designed in an optimized way. The locations of the area monitors have been chosen to verify the compliance with these area classification limits. Moreover, the shielding had to be designed so that the annual effective dose to members of the public, combined from prompt radiation (sky-shine) and from releases to the environment, is less than 1  $\mu\text{Sv}$  for the nominal annual protons on target. The design of the shielding tried to make use of as many existing concrete and iron shielding blocks as possible as well as magnet yokes that had been part of the former LEP accelerator. In total, approximately 2000 tons of iron and 4000 tons of concrete have been used. The design had also to accommodate the fact that design choices were limited due to the presence of existing facilities in the East Experimental Area. [23] Monte Carlo simulations with the FLUKA code have been performed to estimate the prompt ambient equivalent dose rate levels for the CHARM facility.



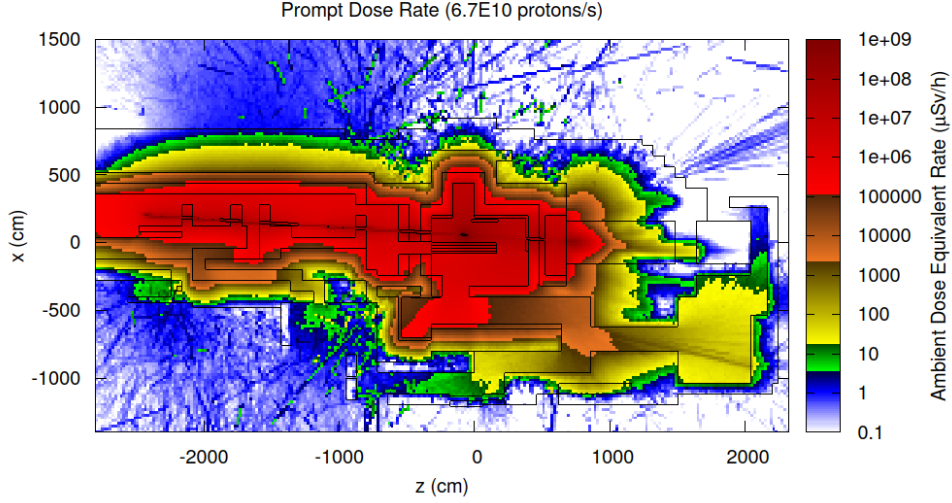


**Figure 3.11:** Prompt radiation for the maximum beam intensity at beam-line level with color-coded area classification (blue covering the acceptable control room levels and green the acceptable low occupancy area levels).

### 3.6.2 Residual radiation

The reduction of the residual ambient radiation levels is an important optimization following the ALARA principle. The International Commission on Radiological Protection (ICRP) has specified in its Recommendation 60 [1] that any exposure of persons to ionizing radiation should be controlled and should be based on three main principles, namely:

- justification: any exposure of persons to ionizing radiation has to be justified
- limitation: personal doses have to be kept below legal limits
- optimization: personal and collective doses have to be kept as low as reasonably achievable (ALARA).

These recommendations have been fully incorporated into CERN's radiation safety code. In addition, reducing the residual ambient radiation levels to

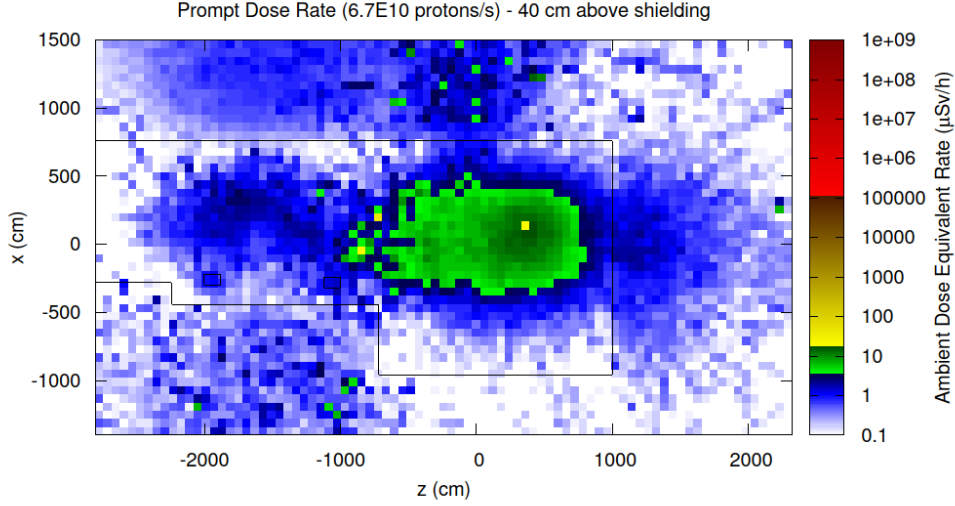


**Figure 3.12:** Prompt radiation for the maximum beam intensity at 40cm above the shielding roof with color-coded area classification (blue covering the acceptable control room levels and green the acceptable low occupancy area levels).

lower the effective dose to personnel during interventions will also decrease the administrative requirements for the interventions and, as a consequence, result in a more efficient exploitation of the facility. Monte Carlo simulations have been performed with FLUKA and the DORIAN code in order to predict the ambient dose equivalent rate levels for various operational scenarios and cool-down times. The ambient dose equivalent rates for the Patch Panel area at cooling time less than 1 day are approximately 3 times higher for the configuration where the movable shielding walls have been retracted from the facility during irradiation than for the configuration where the movable shielding walls have been inside the facility during irradiation. The objective of 100  $\mu\text{Sv/h}$  for the Patch Panel area can be achieved for a cooling time of 1 hour for the maximum beam intensity when the movable shielding walls have been inside the facility during irradiation and for the nominal beam intensity (lower by a factor of 3) when the movable shielding walls have been retracted from the facility during irradiation. [17], [14], [51],[34],[5], [61], [22],[67], [57]

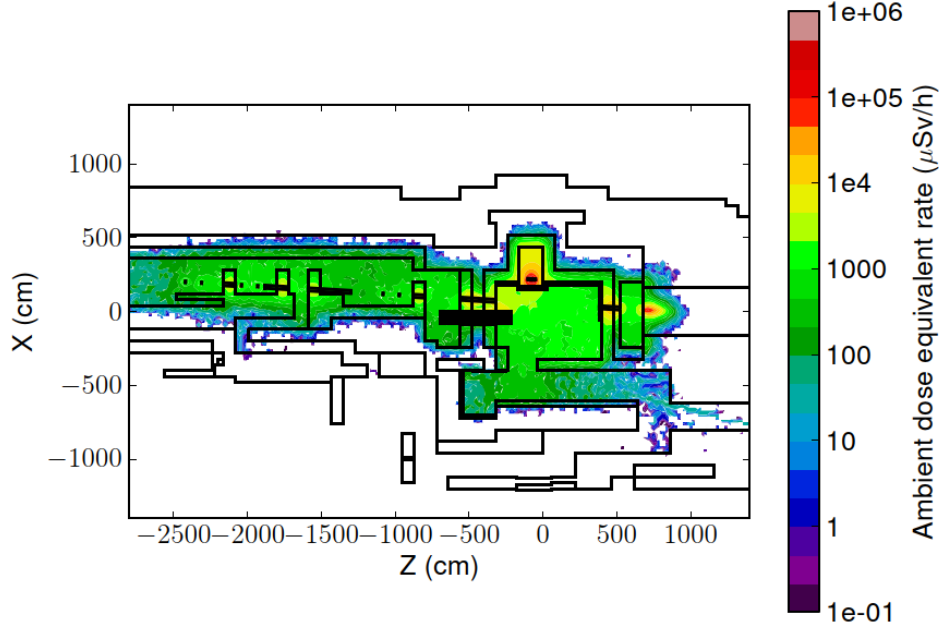


**Figure 3.13:** Residual radiation levels after 200 days of operation with maximum beam intensity followed by 1 hour and 1 day of cool-down

### 3.6.3 Air activation and subsequent release to the environment

The operation of the CHARM facility will result in the activation of the air inside the facility. The following methodology has been used to obtain the radionuclide concentrations, the annual release to the environment and the resulting annual effective dose to members of the public: 1. The track-length spectra for protons, neutron and charged pions have been scored in the air volumes inside the CHARM facility (and the upstream proton facility) in the FLUKA Monte Carlo simulation. 2. These track-length spectra have been folded with a dedicated set of air activation cross-sections to obtain the radionuclide production yields. 3. The radionuclide concentrations in the facility and the release term to the environment have been calculated from the radionuclide production yields taking the time evolution and the characteristics of the ventilation circuit into account. 4. The radionuclide

concentrations in the facility after beam stop have been converted to the committed effective dose due to inhalation without flush for a 1 hour access by application of exposure-to-dose conversion coefficients for inhalation [10]. The decrease of the radionuclide concentrations due to decay during the 1 hour period has been taken into account. 5. The release term has been converted to the effective dose to members of the public by application of release to effective dose conversion coefficients, computed with a dedicated Monte Carlo integration program EDARA [11]. To meet design goal 1, dynamic confinement with a flush before access has been chosen. To meet design goal 2, the effective dose to members of the public has been calculated as a function of the air tightness, which corresponds to the extraction rate to ensure the dynamic confinement, of the facility. A design goal for the air tightness of 2 air volumes per hour has been set to preserve enough margin for the overall design goal of 1  $\mu\text{Sv}$  per year for the effective dose to members of the public. [55], [1], [23],[33]

# Chapter 4

## Neutron attenuation and activation

### 4.1 General

Physics is used to describe the production and behavior of radiation and radioactivity and interactions that determine the energy deposited in media (dose) and allow its detection and modification (shielding). These uses justify a comprehensive and applied treatise of the major physics concepts of radiation protection.

#### 4.1.1 Atoms and energy

Physics constructs radiation protection. It is necessary for describing the origins of radiation, the types and properties of emitted radiation, and the mechanisms by which radiant energy is deposited in various materials. Four basic forces of nature control the dynamics (i.e., position, energy, work, etc.) of all matter, including the constituents of atoms. These forces, along with their magnitude relative to gravity are:

- gravity, which is an attractive force between masses =  $G$
- the weak force, which influences radioactive transformation  $\cong 10^{24}G$

- the electromagnetic force, which exists between electric charges  $\cong 10^{37}G$
- the nuclear force, which is strongly attractive between nucleons only  $\cong 10^{39}G$ .

Two of these forces largely determine the energy states of particles in the atom (gravitational forces are insignificant for the masses of atom constituents, and the weak force is a special force associated with the process of radioactive transformation of unstable atoms):

- the nuclear force between neutrons and protons which is so strong that it overcomes the electrical repulsion of the protons (which is quite strong at the small dimensions of the nucleus) and holds the nucleus and its constituent protons and neutrons together
- the force of electrical attraction between the positively charged nucleus and the orbital electrons which not only holds the electrons within the atom, but influences where they orbit.

### Structure of Atoms

Atoms contain enormous amounts of energy distributed among the energy states of the constituent parts. Some of this energy is emitted from the atom if an overall decrease occurs in the potential energy states of one or more of the constituents, and similarly absorption of radiant energy by an atom yields an increase in the potential energy of one or more states. Atom constituents are primarily neutrons, protons, and electrons, and their number and array establish what the element is and whether its atoms are stable or unstable and if unstable, how the atoms will emit energy.

Atoms are bound systems. More specific, they only exist when protons and neutrons are bound together to form a nucleus and when electrons are bound in orbits around the nucleus. The particles in atoms are bound into such an array because nature forces atoms toward the lowest potential energy possible. When they attain it they are stable, and until they do they have excess energy and are thus unstable, or radioactive.

The proton has a reference mass of about 1.0. It also has a positive electrical charge of plus 1 (+1). The electron is much lighter than the proton. It's mass is about 1/1840 of that of the proton and it has an electrical charge of minus one ( $\sim 1$ ). The neutron is almost the same size as the proton, but slightly heavier. It has no electrical charge. When these basic building blocks are put together, which is what happened at the beginning of time, very important things become evident.

The resulting atom is electrically neutral. This is, each ( $\sim 1$ ) charge on an orbital electron is matched by a (+1) positively charged proton in the nucleus. The total atom (the proton and an electron) has a diameter of about  $10^{10}$  m (or  $10^8$  cm) and is much bigger than the central nucleus which has a radius of about  $10^{15}$  m or ( $10^{13}$  cm) thus the atom is mostly empty space. The radius of the nucleus alone is proportional to  $A^{1/3}$ , where A is the atomic mass number of the atom in question or  $r = r_o A^{1/3}$ . The constant  $r_o$  varies according to the element but has an average value of about  $1.3 \times 10^{15}$  m, or femtometers.

#### 4.1.2 Nuclide Chart

The logical pattern of atom building can be plotted in terms of the number of protons and neutrons in each create of chart of the nuclides. This portion is plotted in the next figure.

#### 4.1.3 Discoveries in Radiation Physics

Roentgen's discovery of x-rays in 1895 began a series of discoveries that explained the structure of matter. Radioactivity, which was discovered shortly after, established that atoms are made up of constituent components, and it also made it possible to aim alpha particles at foils and gases. Rutherford discovered that an atom must have a small positively charged nucleus because the observed scattering of alpha particles requires a very small scattering center at the center of the atom. Bohr used this discovery and other

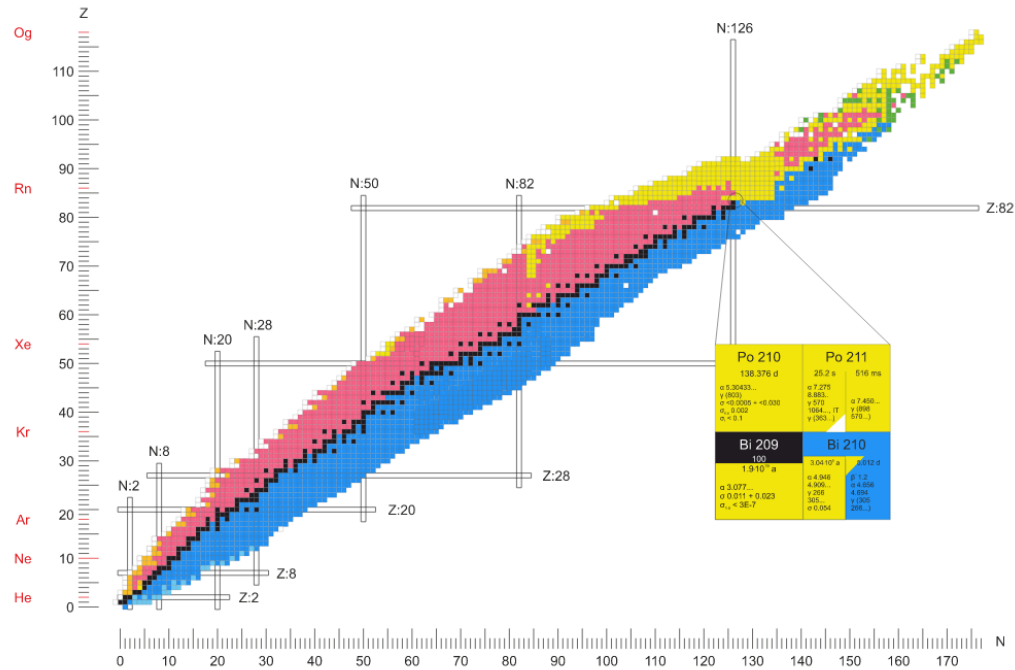


**Figure 4.1:** The nuclide chart

findings, including Planck's revolutionary hypothesis, to describe the motion of electrons and the processes of emission and absorption of radiation. Bohr's model of the atom was not quite precise, especially when applied to more complex atoms. The current concept of the atom might better be called a nebular model, with electrons spread as waves of probability over the whole volume of the atom, a direct consequence of de Broglie's discovery of the wave characteristics of electrons and other particles. The electrons are distributed around the nucleus in energy states determined by four quantum numbers according to the exclusion principle and at radii that are an equal number of de Broglie wavelengths, or  $n \lambda$ , where  $n$  is the principal quantum number corresponding to the respective energy shells K, L, M, etc., for  $n = 1, 2, 3$ , etc. The dynamics of the electrons are described by the Schrodinger wave equation. Changes between states are quantized, and discrete energies are apparent. The outer radius of the nebular cloud of electrons is about  $10^{10}$  m which is some 4 to 5 orders of magnitude greater than the nuclear radius at



about  $10^{-15}$  m. The nucleus contains  $Z$  protons which contribute both mass and positive charge, and neutrons (slightly heavier than protons) which make up the balance of the mass and help to distribute the nuclear force. Electrons do not, and, according to the uncertainty principle, cannot exist in the nucleus, although they can be manufactured and ejected during radioactive transformation.

#### 4.1.4 Basic properties of the neutron

The neutron is a nuclear particle, that does not have electrical charge. Its mass is  $939.56 \text{ MeV}/c^2$ ,  $m_n = 1.675 \times 10^{-27} \text{ kg}$ , close to that of the proton ( $938.27 \text{ MeV}/c^2$ ). The neutron does not exist naturally in free form, but decays into a proton, an electron, and an anti-neutrino. The neutron lifetime is  $\tau = 886 \text{ sec}$  and is much longer than the time of a neutron within a scattering experiment, where each neutron spends merely a fraction of a second. Even if the neutron is electrically neutral, still possess a magnetic moment  $\mu = \gamma \mu_N$ , where  $\gamma = 1.913$  is the neutron magnetogyric ratio and the nuclear magneton is given by  $\mu_N = eh/mp$ . The neutron magnetic moment is coupled antiparallel to its spin, which has the value  $s = 1/2$ . The neutron interacts with nuclei via the strong nuclear force and with magnetic moments via the electromagnetic force. The neutron also consists of three quarks, one up quark and two down quarks. The free neutron is unstable with a mean lifetime of about 15 minutes ( $880.2 \pm 1.0 \text{ s}$ ). Because of its mass, it can decay into a proton, an electron antineutrino and an electron. This radioactive decay is named  $\beta^-$  decay. The neutrons exist in the nuclei of typical atoms, along with their positively charged counterparts, the protons. Protons and neutrons have also their structure. Inside the protons and neutrons, there are true elementary particles called quarks. Within the nucleus, protons and neutrons are bound together through the strong force, a fundamental interaction that governs the behaviour of the quarks that make up the individual protons and neutrons.

A nuclear stability is determined by the competition between two fun-

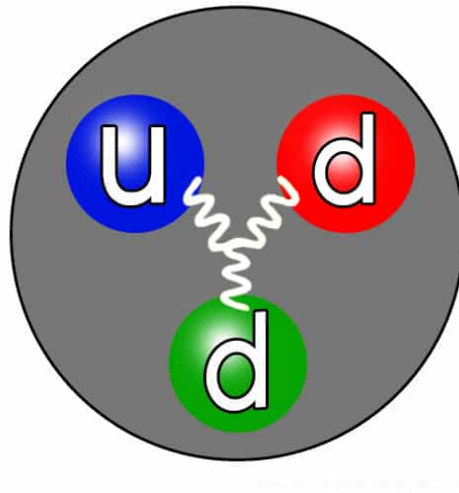


**Figure 4.2:** The quark structure of the neutron. The color assignment of individual quarks is arbitrary, but all three colors must be present. Forces between quarks are mediated by gluons

damental interactions. Protons and neutrons are attracted each other via strong force. On the other hand protons repel each other via the electric force due to their positive charge. Therefore neutrons within the nucleus act somewhat like nuclear glue, neutrons attract each other and protons, which helps offset the electrical repulsion between protons. There are only certain combinations of neutrons and protons, which forms stable nuclei. For example, the most common nuclide of the common chemical element lead (Pb) has 82 protons and 126 neutrons.

Because of the strength of the nuclear force at short distances, the nuclear binding energy (the energy required to disassemble a nucleus of an atom into its component parts) of nucleons is more than seven orders of magnitude larger than the electromagnetic energy binding electrons in atoms.

### Structure of the Neutron

The quark structure of the neutron. The color assignment of individual quarks is arbitrary, but all three colors must be present. Forces between quarks are mediated by gluons. Neutrons and protons are classified as hadrons, subatomic particles that are subject to the strong force and as

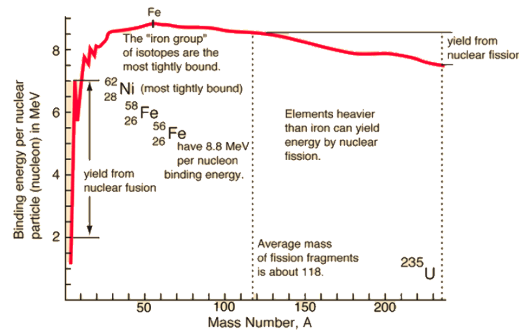


**Figure 4.3:** Nuclear binding energy curve. Source: [hyperphysics.phy-astr.gsu.edu](http://hyperphysics.phy-astr.gsu.edu)

baryons since they are composed of three quarks. The neutron is a composite particle made of two down quarks with charge  $-1/3e$  and one up quark with charge  $+2/3e$ . Since the neutron has no net electric charge, it is not affected by electric forces, but the neutron does have a slight distribution of electric charge within it. This results in non-zero magnetic moment (dipole moment) of the neutron. Therefore the neutron interacts also via electromagnetic interaction, but much weaker than the proton.

The mass of the neutron is  $939.565 \text{ MeV}/c^2$ , whereas the mass of the three quarks is only about  $12 \text{ MeV}/c^2$  (only about 1 per cent of the mass-energy of the neutron). Like the proton, most of mass (energy) of the neutron is in the form of the strong nuclear force energy (gluons). The quarks of the neutron are held together by gluons, the exchange particles for the strong nuclear force. Gluons carry the color charge of the strong nuclear force.

**Detection of Neutrons** Since the neutrons are electrically neutral particles, they are mainly subject to strong nuclear forces, but not to electric forces. Therefore neutrons are not directly ionizing and they have usually to be converted into charged particles before they can be detected. Generally every type of neutron detector must be equipped with converter (to convert neutron radiation to common detectable radiation) and one of the conventional radiation detectors (scintillation detector, gaseous detector, semiconductor detector, etc.).

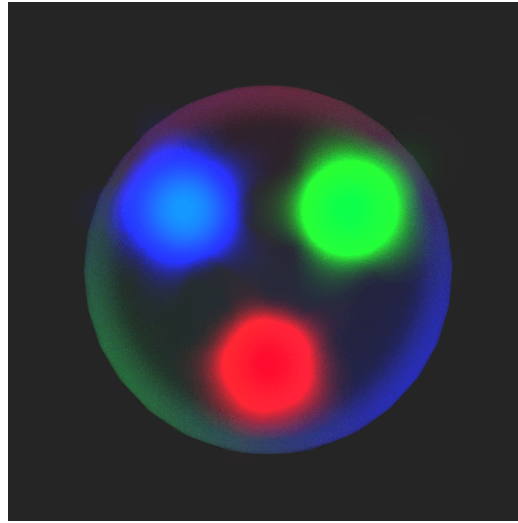


**Figure 4.4:** The quark structure of the neutron. The color assignment of individual quarks is arbitrary, but all three colors must be present. Forces between quarks are mediated by gluons.

### Shielding of Neutron Radiation

The amount of radiation exposure depends directly (linearly) on the time people spend near the source of radiation. The dose can be reduced by limiting exposure time. Moreover, the amount of radiation exposure depends on the distance from the source of radiation. Finally we have the shielding, if the source is too intensive and time or distance do not provide sufficient radiation protection the shielding must be used. Radiation shielding usually consist of barriers of lead, concrete or water. It depends on type of radiation to be shielded, which shielding will be effective or not.

There are three main features of neutrons, which are crucial in the shielding of neutrons.

- Neutrons have no net electric charge, therefore they cannot be affected or stopped by electric forces. Neutrons ionize matter only indirectly, which makes neutrons highly penetrating type of radiation.
- Neutrons scatter with heavy nuclei very elastically. Heavy nuclei very hard slow down a neutron let alone absorb a fast neutron.

- An absorption of neutron (one would say shielding) causes initiation of certain nuclear reaction (e.g. radiative capture or even fission), which is accompanied by a number of other types of radiation. In short, neutrons make matter radioactive, therefore with neutrons we have to shield also the other types of radiation.

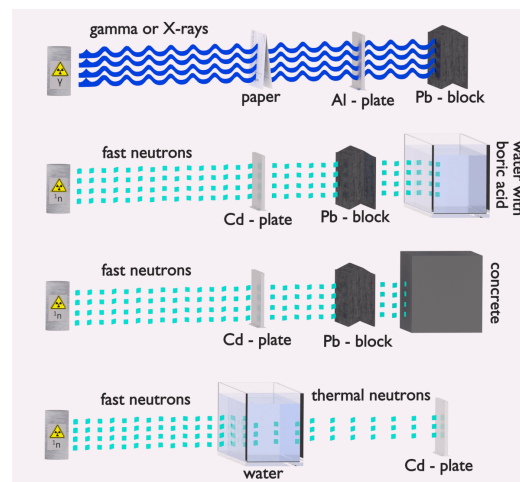


Figure 4.5

The best materials for shielding neutrons must be able to:

- Slow down neutrons. This can be fulfilled only by material containing light atoms (e.g. hydrogen atoms), such as water, polyethylene, and concrete. The nucleus of a hydrogen nucleus contains only a proton. Since a proton and a neutron have almost identical masses, a neutron scattering on a hydrogen nucleus can give up a great amount of its energy (even entire kinetic energy of a neutron can be transferred to a proton after one collision).
- Absorb this slow neutron. Thermal neutrons can be easily absorbed by capture in materials with high neutron capture cross sections (thousands of barns) like boron, lithium or cadmium.
- Shield the accompanying radiation.

		Thermal neutron			Fast neutron		
		Scattering	Capture	Fission	Scattering	Capture	Fission
Moderator	H-1	20	0.2	-	4	0.00004	-
	H-2	4	0.0003	-	3	0.000007	-
	C-12	5	0.002	-	2	0.00001	-
Structural materials, others	Zr-90	5	0.006	-	5	0.006	-
	Fe-56	10	2	-	20	0.003	-
	Cr-52	3	0.5	-	3	0.002	-
	Ni-58	20	3	-	3	0.008	-
	O-16	4	0.0001	-	3	0.00000003	-
Absorber	B-10	2	200	-	2	0.4	-
	Cd-113	100	30	-	4	0.05	-
	Xe-135	400	2,000,000	-	5	0.0008	-
	In-115	2	100	-	4	0.02	-
Fuel	U-235	10	99	583	4	0.09	1
	U-238	9	2	0.00002	5	0.07	0.3
	Pu-239	8	269	748	5	0.05	2

**Figure 4.6:** Table of cross-sections**Water as a neutron shield**

Water due to the high hydrogen content and the availability is effective and common neutron shielding. However, due to the low atomic number of hydrogen and oxygen, water is not acceptable shield against the gamma rays. On the other hand in some cases this disadvantage (low density) can be compensated by high thickness of the water shield. In case of neutrons, water perfectly moderates neutrons, but with absorption of neutrons by hydrogen nucleus secondary gamma rays with the high energy are produced. These gamma rays highly penetrates matter and therefore it can increase requirements on the thickness of the water shield. Adding a boric acid can help with this problem (neutron absorbtion on boron nuclei without strong gamma emission), but results in another problems with corrosion of construction materials.

**Concrete as a neutron shielding**

Most commonly used neutron shielding in many sectors of the nuclear science and engineering is shield of concrete. Concrete is also hydrogen-containing

material, but unlike water concrete have higher density (suitable for secondary gamma shielding) and does not need any maintenance. Because concrete is a mixture of several different materials its composition is not constant. So when referring to concrete as a neutron shielding material, the material used in its composition should be told correctly. Generally concrete are divided to “ordinary“ concrete and “heavy” concrete. Heavy concrete uses heavy natural aggregates such as barites (barium sulfate) or magnetite or manufactured aggregates such as iron, steel balls, steel punch or other additives. As a result of these additives, heavy concrete have higher density than ordinary concrete ( $\approx 2300\text{kg}/\text{m}^3$ ). Very heavy concrete can achieve density up to  $5900\text{kg}/\text{m}^3$  with iron additives or up to  $8900\text{kg}/\text{m}^3$  with lead additives. Heavy concrete provide very effective protection against neutrons.[21]. [38],[49], [56]

## 4.2 Nuclear reactions

The passage of particles through the matter can be characterized by two general effects. Energy loss and trajectory detection. For charged particles these effects are primarily due to electromagnetic interactions, mainly inelastic scattering with orbital electrons. Reactions with nuclei involving the strong interaction are rarer as consequence of the short range of this force,  $10^{-15}$  m, the typical size of nuclei. Furthermore, nuclei are typically 100.000 times smaller than the distance between them in solid matter. Neutrons are also subject to the electromagnetic and weak forces. In materials with unpaired electrons, neutrons may interact through a dipole-dipole interaction between the magnetic moments of the neutron and the unpaired electron. During elastic collisions the identity of particles, do not change and the total kinetic energy is conserved. During an inelastic collision with a nucleus, part of the kinetic energy of the interacting particles is dissipated through the nucleus excitation and/or with production of new particles. The combination of both effects explain why neutrons are very penetrating particles,

since their primary interaction is through the strong nuclear force with nuclei. When a particle strikes a nucleus, two classes of collisions can happen, elastic and inelastic scattering. Independently of energy and type of incident particles, elastic scattering from nuclei is always present. The incident particle transfers part of its energy to the recoil nucleus but the event does not contribute to activation since no new particles are created. For its part, inelastic scattering contributes to induced activity only if unstable particles are created. During a nuclear reaction, an external particle comes in such close contact to the atomic nucleus that they interact, most of the time via the very short range strong force. As leptons are not a problem to this interaction, they rarely interact with nuclei. The strong interaction only acts between quarks. Hadrons are composite particles made of quarks ( $q$ ). There are three subgroups of hadrons: baryons ( $qqq$ ), antibaryons  $q\bar{q}q$  and mesons  $q\bar{q}$ . So hadrons, in sequence, have the ability to interact with nuclei but for that to happen, positively charged hadrons, such as protons, must overcome the Coulomb potential barrier of the nucleus.

### 4.3 Neutron interactions

Neutrons have no charge and that is why they cannot interact in matter with the Coulomb force. When a neutron interacts, it is with a nucleus of the absorbing material. As a consequence, the neutron creates secondary particles or the neutron energy or direction is significantly changed. In contrast to photon interactions, the products resulting from neutron interactions are almost always heavy particles. These particles can result from neutron-induced nuclear reactions or can be the nuclei of the absorbing material itself, which have gained energy from neutron collisions. Regarding the thermal and slow neutron reactions less than ( $\sim 10\text{MeV}$ ), we have at first the elastic scattering ( $X(n, n)X$ ). The main mechanism of energy loss for neutrons up to 1 MeV. The internal energy of the nucleus is unaffected meaning that no energy is transferred into nuclear excitation. The linear momentum



and kinetic energy of the system are conserved, however, the neutron usually transfers part of its energy to the recoil nucleus. As far as the inelastic scattering ( $X(n, n')X^*$ ), we have the Neutron absorption by a nucleus forming a compound nucleus that subsequently emits a secondary neutron of lower kinetic energy. The original nucleus, left in an excited state, without nature change of decays afterwards by  $\gamma$  ray emission. The neutron energy must be higher than about 1 MeV in order to excite the nucleus. There is also the radioactive neutron capture  ${}^A_ZX(n_\gamma){}^{A+1}_ZX$ . Absorption of a neutron by a nucleus that, after some time, decays to its ground state by  $\gamma$  emission. The radiative capture is most likely to occurs with thermal and slow neutrons since, usually, the cross section for neutron capture varies approximately with  $\sim 1/v$  where  $v$  is the neutron velocity. In particle ejection  $X(n, x)Y$ ,  $x = p, \alpha$ , after absorbing a neutron, the energy excitation level of the compound nucleus is high enough to cause it to eject a proton or  $\alpha$  particle. The remaining nucleus can still be in an excited state and decays through  $\gamma$  emission. The particle ejection starts to be observed with thermal and slow neutrons for light target nucleus, whereas for heavier elements, higher energies of the incoming neutrons are required.

### Slow neutron interactions

The important interactions, for slow neutrons, are elastic scattering with absorber nuclei and a large set of neutron-induced nuclear reactions. Due to their small kinetic energy, very small amount of energy can be transferred to the nucleus in elastic scattering. Elastic collisions can have large cross sections and they often bring slow neutrons into thermal equilibrium with the medium of the absorber before another kind of interaction occurs. A big part of the population in the slow neutron energy range is found among thermal neutrons that they have an energy of about 0.025 eV at room temperature. The slow neutron interaction of big interest are the neutron-induced reactions that can create secondary radiation of sufficient energy to be detected directly. For the reason that the incoming neutron energy is low, all reactions

must have a positive Q-value to be energetically possible. The radiative capture  $n$  is the most probable and very critical in the attenuation or shielding of slow neutrons. This reaction can be used for indirect detection of neutrons using activation foils. Reactions like  $(n, \gamma)$ ,  $(n, p)$  and  $(n, fission)$  are preferred for active neutron detectors because the secondary radiations are charged particles.

### Fast neutron interactions

The neutron can transfer a considerable amount of energy in one collision, so with increasing neutron energy the importance of scattering becomes greater for detection purposes. In that example, the secondary radiations are recoil nuclei that have a detectable amount of energy deriving from neutron collisions. At every scattering the neutron loses energy and so is moderated or slowed to lower energy. The most efficient moderator is hydrogen because the neutron can lose up to all its energy in a single collision with a hydrogen nucleus. When the nuclei are heavier only a partial energy transfer is feasible. If the energy of the fast neutron is adequately high then inelastic scattering with nuclei can occur, in which the recoil nucleus is raised to one of its excited states during the collision. With the emission of a  $\gamma$  ray the nucleus quickly de-excites and the neutron loses a greater fraction of its energy than it would in an elastic collision. Inelastic scattering and the successive  $\gamma$  ray emission play a leading role in the shielding of fast neutrons but are an undesirable effect in the response of most fast neutron detectors that are based on elastic scattering.

#### 4.3.1 Neutron cross section

In general, the cross section is something that quantifies the likelihood of certain interaction between an incident object and a target object. The cross section of a particle is the same as the cross section of a hard object, if the probabilities of hitting them with a ray are the same. For a given event, the

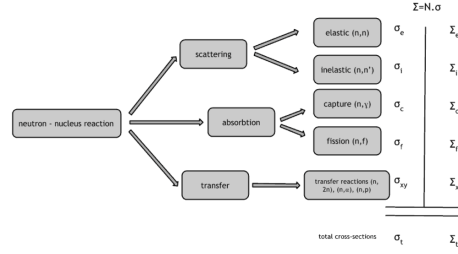
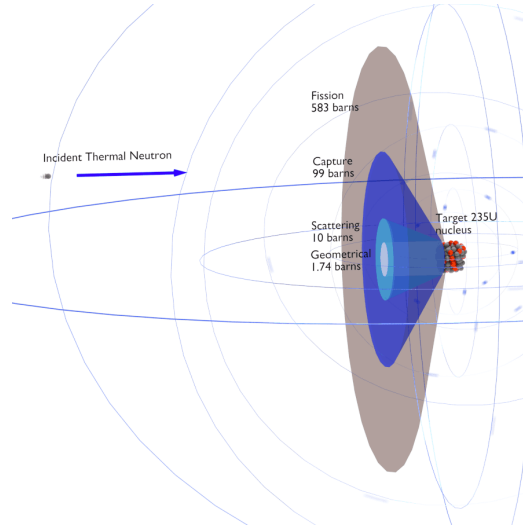


Figure 4.7

cross section  $\sigma$  is given by

$$\sigma = \mu/n \quad (4.1)$$

where  $\sigma$  is the cross section of this event  $m^2$ ,  $\mu$  is the attenuation coefficient due to the occurrence of this event  $[m^{-1}]$ ,  $n$  is the density of the target particles  $[m^{-3}]$ .



**Figure 4.8:** Graphical interpretation of the neutron cross section illustrated with the case of a thermal (25.3 meV) neutron interacting with a  $^{235}\text{U}$  nucleus.

In nuclear physics, the nuclear cross section of a nucleus is commonly used to characterize the probability that a nuclear reaction will occur. The cross section is typically denoted  $\sigma$  and measured in units of area  $[m^2]$ . The

standard unit for measuring a nuclear cross section is the barn, which is equal to  $10^{-28}m^2$  or  $10^{-24}cm^2$ . The nuclear cross section can be quantified physically in terms of “characteristic target area” where a larger area means a larger probability of interaction. About the nuclear radii we have that a typical nuclear radii are of the order  $10^{-14}m$ . Assuming spherical shape, nuclear radii can be calculated according to following formula:

$$r = r_0 A^{1/3} \quad (4.2)$$

where  $r_0 = 1,2 \times 10^{-15}m = 1,2 fm$ . If we use this approximation, we therefore expect the geometrical cross sections of nuclei to be of the order of  $\pi^2$  or  $4,510^{-30}m^2$  for hydrogen nuclei or  $1,74 \times 10^{-28}m^2$  for  $^{238}U$  nuclei.

In general, nuclear cross-sections can be measured for all possible interaction processes together, in this case they are called total cross-sections  $\sigma_t$ . The total cross section is the sum of all the partial cross sections such as:

- elastic scattering cross-section ( $\sigma_s$ )
- inelastic scattering cross-section ( $\sigma_i$ )
- absorption cross-section ( $\sigma_a$ )
- radiative capture cross-section ( $\sigma_\gamma$ )
- fission cross-section  $\sigma_f$

$$\sigma_t = \sigma_s + \sigma_i + \sigma_\gamma + \sigma_f + \dots \quad (4.3)$$

The total cross section measures the probability that an interaction of any type will occur when neutron interacts with a target. As we mentioned earlier, neutrons are neutral particles, therefore they travel in straight lines, deviating from their path only when they actually collide with a nucleus to be scattered into a new direction or absorbed. Neither the electrons surrounding (atomic electron cloud) a nucleus nor the electric field caused by a positively

charged nucleus affect a neutron's flight. In short, neutrons collide with nuclei, not with atoms.

### Microscopic Cross section

The extent to which neutrons interact with nuclei is described in terms of quantities known as cross sections. Cross sections are used to express the likelihood of particular interaction between an incident neutron and a target nucleus. It must be noted this likelihood do not depend on real target dimensions. In conjunction with the neutron flux, it enables the calculation of the reaction rate. The standard unit for measuring the microscopic cross section  $\sigma$  is the barn, which is equal to  $10^{-28}m^2$ , since this is the order of magnitude of the cross sectional area of the atomic nucleus. The reaction rate (i.e. number of reactions per unit time) induced by a neutron beam with a flux  $\phi(n/cm^2/s)$  that impinges an isotopically pure thin film with surface  $S(cm^2)$ , areal density  $n(atoms/b)$ , is directly proportional to the total neutron cross section  $\sigma_{tot}(b)$  by

$$R = \sigma_{tot}\phi S n \quad (4.4)$$

The theoretical description of neutron cross sections varies depending on the time scale of the interaction within the nucleus, related to the neutron energy. According to this, neutron-nucleus reactions can be classified as

- Direct reactions. A neutron and a target nucleus interact for a very short time ( $\tau \sim 10^{-22}s$ ) allowing for an interaction with a single nucleon. This reactions require minimum neutron energies of  $\sim 5 MeV/A$  and are characterised by anisotropic distributions of the outgoing particles.
- Compound Nucleus reactions. The neutron and the nucleus are within the range of nuclear forces for a sufficiently long time ( $10^{-16} - 10^{-18} s$ ), allowing the creation of a relatively long lived intermediate state called the Compound Nucleus.

The cross section  $\sigma$  can be interpreted as the effective 'target area' that a nucleus interacts with an incident neutron. The larger the effective area,

the greater the probability for reaction. This cross section is usually known as the microscopic cross-section.

The concept of the microscopic cross section is therefore introduced to represent the probability of a neutron-nucleus reaction. Suppose that a thin 'film' of atoms (one atomic layer thick) with  $N_a \text{ atoms/cm}^2$  is placed in a monodirectional beam of intensity  $I_0$ . Then the number of interactions  $C$  per  $\text{cm}^2$  per second will be proportional to the intensity  $I_0$  and the atom density  $N_a$ . We define the proportionality factor as the microscopic cross-section  $\sigma$ :

$$\sigma_t = C/N_a I_0 \quad (4.5)$$

In order to be able to determine the microscopic cross section, transmission measurements are performed on plates of materials. Assume that if a neutron collides with a nucleus it will either be scattered into a different direction or be absorbed (without fission absorption). Assume that there are  $N$  (nuclei/  $\text{cm}^3$ ) of the material and there will then be  $Ndx$  per  $\text{cm}^2$  in the layer  $dx$ . Only the neutrons that have not interacted will remain traveling in the  $x$  direction. This causes the intensity of the uncollided beam will be attenuated as it penetrates deeper into the material.

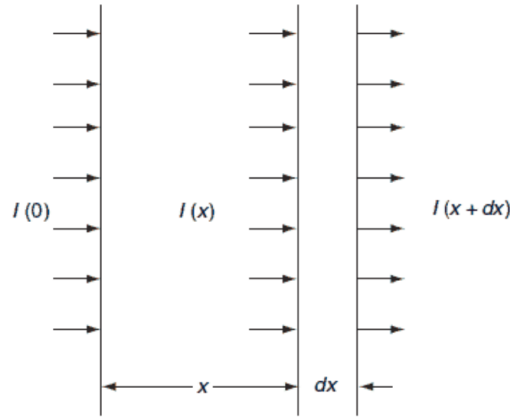
Then, according to the definition of the microscopic cross section, the reaction rate per unit area is  $N\sigma(x)dx$ . This is equal to the decrease of the beam intensity, so that

$$-dI = N\sigma I(x)dx \quad (4.6)$$

and

$$I(x) = I_0 e^{-N\sigma x} \quad (4.7)$$

It can be seen that whether a neutron will interact with a certain volume of material depends not only on the microscopic cross-section of the individual nuclei but also on the density of nuclei within that volume. It depends

**Figure 4.9**

on the  $N\sigma$  factor. This factor is therefore widely defined and it is known as the macroscopic cross section.

The difference between the microscopic and macroscopic cross sections is very important. The microscopic cross section represents the effective target area of a single nucleus, while the macroscopic cross section represents the effective target area of all of the nuclei contained in certain volume.

Microscopic cross sections constitute a key parameters of nuclear fuel. In general, neutron cross sections must be calculated for fresh fuel assemblies usually in two dimensional models of the fuel lattice.

In general, the neutron cross section is variable and depends on:

- Target nucleus (hydrogen, boron, uranium, etc.). Each isotope has its own set of cross-sections.
- Type of the reaction (capture, fission, etc.). Cross-sections are different for each nuclear reaction.
- Neutron energy (thermal neutron, resonance neutron, fast neutron). For a given target and reaction type, the cross section is strongly dependent on the neutron energy. In the common case, the cross section is usually much larger at low energies than at high energies.

- Target energy (temperature of target material – Doppler broadening). This dependency is not so significant, but the target energy strongly influences inherent safety of nuclear reactors due to a Doppler broadening of resonances.

Microscopic cross section varies with incident neutron energy. Some nuclear reactions exhibit very specific dependency on incident neutron energy. This dependency will be described on the example of the radiative capture reaction. The likelihood of a neutron radiative capture is represented by the radiative capture cross section as  $\sigma_\gamma$ .

The capture cross-section can be divided into three regions according to the incident neutron energy. These regions will be discussed separately.

- $1/v$  Region
- Resonance Region
- Fast Neutrons Region

In the common case, the cross section is usually much larger at low energies than at high energies. For thermal neutrons (in  $1/v$  region), also radiative capture cross sections increase as the velocity (kinetic energy) of the neutron decreases. Therefore the  $1/v$  Law can be used to determine shift in capture cross section, if the neutron is in equilibrium with a surrounding medium. This phenomenon is due to the fact the nuclear force between the target nucleus and the neutron has a longer time to interact.

$$\sigma_a \sim \frac{1}{v} \sim \frac{1}{\sqrt{E}} \sim \frac{1}{\sqrt{T}} \quad (4.8)$$

This law is applicable only for absorption cross-section and only in the  $1/v$  region.

### Resonance Region

The largest cross sections are usually at neutron energies, that lead to long-lived states of the compound nucleus. The compound nuclei of these certain





excited states it is more likely that one neutron obtains an energy in collision with other nucleon greater than its binding energy in the nucleus. The neutron emission becomes dominant and gamma decay becomes less important. Moreover, at high energies, the inelastic scattering and  $(n, 2n)$  reaction are highly probable at the expense of both elastic scattering and radiative capture.

### Macroscopic Cross section

The difference between the microscopic cross section and macroscopic cross section is very important and is restated for clarity. The microscopic cross section represents the effective target area of a single target nucleus for an incident particle. The units are given in barns or  $cm^2$ .

While the macroscopic cross section represents the effective target area of all of the nuclei contained in the volume of the material. The units are given in  $cm^{-1}$

A macroscopic cross section is derived from microscopic cross section and the atomic number density:

$$\Sigma = \sigma N \quad (4.9)$$

Here  $\sigma$ , which has units of  $m^2$ , is the microscopic cross-section. Since the units of  $N$  (nuclei density) are nuclei /  $m^3$ , the macroscopic cross-section  $\Sigma$  have units of  $m^{-1}$ , thus in fact is an incorrect name, because it is not a correct unit of cross-sections. In terms of  $\Sigma_t$  (the total cross-section), the equation for the intensity of a neutron beam can be written as

$$-dI = N\sigma\Sigma_t dx \quad (4.10)$$

Dividing this expression by  $I(x)$  gives

$$-dI(x)/I(x) = \Sigma_t dx \quad (4.11)$$

Since  $dI(x)$  is the number of neutrons that collide in  $dx$ , the quantity  $-dI(x)/I(x)$  represents the probability that a neutron that has survived without colliding until  $x$ , will collide in the next layer  $dx$ . It follows that the prob-

ability  $P(x)$  that a neutron will travel a distance  $x$  without any interaction in the material, which is characterized by  $\Sigma_t$ , is:

$$P(x) = e^{-\Sigma_t x} \quad (4.12)$$

From this equation, we can derive the probability that a neutron will make its first collision in  $dx$ . It will be the quantity  $P(x)dx$ . If the probability of the first collision in  $dx$  is independent of its past history, the required result will be equal to the probability that a neutron survives up to layer  $x$  without any interaction ( $\sim \Sigma_t dx$ ) times the probability that the neutron will interact in the additional layer  $dx$  (i.e.  $\sim e^{-\Sigma_t x}$ ).

$$P(x)dx = \Sigma_t dx e^{-\Sigma_t x} = \Sigma_t e^{-\Sigma_t x} dx \quad (4.13)$$

**Mean Free Path** From the equation for the probability of the first collision in  $dx$  we can calculate the mean free path that is traveled by a neutron between two collisions. This quantity is usually designated by the symbol  $\lambda$  and it is equal to the average value of  $x$ , the distance traveled by a neutron without any interaction, over the interaction probability distribution.

$$\lambda = \int_0^\infty x p(x) dx = \Sigma_t \int_0^\infty x e^{-\Sigma_t x} dx = 1/\Sigma_t \quad (4.14)$$

whereby one can distinguish  $\lambda_s$ ,  $\lambda_a$ ,  $\lambda_f$ , etc. This quantity is also known as the relaxation length, because it is the distance in which the intensity of the neutrons that have not caused a reaction has decreased with a factor  $e$ .

For materials with high absorption cross section, the mean free path is very short and neutron absorption occurs mostly on the surface of the material. This surface absorption is called self shielding because the outer layers of atoms shield the inner layers.

## 4.4 Neutron attenuation

In the case that the interactions by primary protons of energy are less than 1 GeV, the average secondary particle energy will be less than 120 MeV and then their attenuation mean free path in the shielding varies with energy. Experimental data of the attenuation mean free paths of radiation in concrete exposed laterally to secondary radiation from proton interactions have been reviewed and compared with calculated values. These mean free paths are expressed as a proportion of the limiting value at high energies,  $\lambda_0$ . The neutron attenuation length is shown in the figure below for concrete and mono energetic broad beam conditions. The attenuation length reaches a value of approximately  $117 \text{ g/cm}^2$  above 200 MeV. As the cascade through thick shielding is driven by the high energy particles, this value is equal to the equilibrium attenuation length at 90 degrees in concrete.

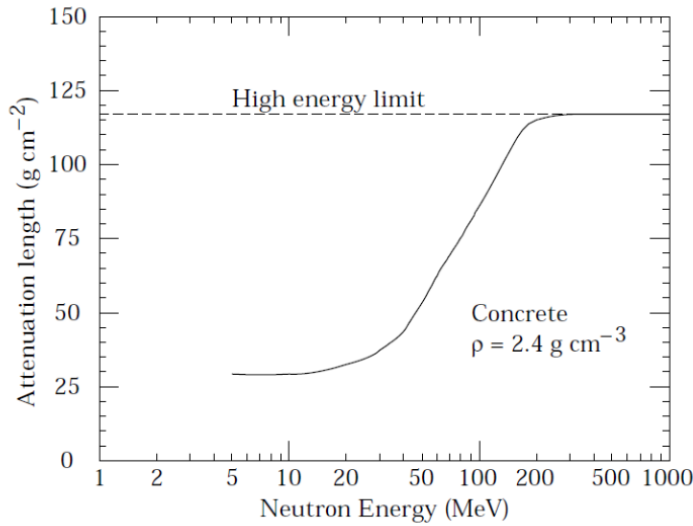


**Figure 4.12:** The variation of the attenuation length for mono-energetic neutrons in concrete as a function of neutron energy.

## 4.5 Neutron activation

When components at accelerators are exposed directly to the beam or to stray radiation, they may become radioactive decaying by gamma-rays, beta particles and rarely neutrons. The induced radioactivity produced when the accelerator is under operation remains after the accelerator has stopped operating, often for several years. It is one of the risks to the intervening personnel and demands serious restrictions on the accessibility of activated equipment for operation, maintenance, repairs and decommissioning purposes after the shutdown.

### 4.5.1 Properties of induced radioactivity

In the case that a high energy hadron interacts with a nucleus, neutrons, protons and other nuclear fragments can be emitted, converting the struck nucleus to that of a different nuclide, which might be radioactive. An amount of the secondary particles emitted in an interaction may have sufficient energy to continue and cause additional activation and therefore provoking a nuclear particle cascade. In this process, many nuclei are produced in excited states and de-excite by emitting neutrons, charged particles or fragments (that can be in an excited state as well) in a so called "evaporation" process, or they may de-excite by emitting photons. The process can continue and radionuclides can be produced till the energies of the particles fall below the thresholds for the nuclear reactions concerned or, in the case of exothermic reactions, until they are captured. Nevertheless, the total amount of radioactivity induced in an accelerator will depend on the primary beam loss, the likelihood of generating a particular radionuclide will also depend on the composition of the material struck, the spectrum of secondaries produced and the production cross section of the isotope concerned. The amount of radionuclides present at any given time will also depend on the radionuclide half-life and the time that the accelerator has been in operation, as well as on the time that the activity has had to decay since operation stopped. Therefore, the estimation

of induced radioactivity in an accelerator is a complicated process.

### 4.5.2 Estimation of induced radioactivity

In general, induced radioactivity can be generated at all accelerators that produce particles above the reaction threshold of the activation process of interest. When the accelerated beam hits a nucleus, the resulting nuclear reactions can generate a different nuclide, which may or may not be radioactive. The most simple activation situation at accelerators is that of fixed irradiation of some material by a spatially uniform flux density of particles that begins at time  $t = 0$  and continues at a constant rate for an irradiation period that ends at  $t = t_i$ . This is followed by a decay period called the cooling time  $t_c$ . A period of time that begins at  $t = t_i$  and ends at  $t = t_i + t_c$ . For this situation, self-absorption of the hadrons by the target is ignored, as is the fact that a whole energy spectrum of particles might be incident. Hence, the process of producing the radioactivity is characterized by a single average cross section factor  $\sigma$ . In the more complicated generalized situations the value of this cross section must be obtained from averaging over the energy spectra of the incident particles. The number of atoms of the radionuclide of interest per unit volume, in the absence of decay chains, will thus be governed by the following equation during the irradiation period:

$$\frac{dn(t)}{dt} = -\lambda n(t) + N\sigma\phi \quad (4.15)$$

where  $n(t)$  is the number density of atoms ( $cm^{-3}$ ) of the radionuclide of interest at time  $t$ ,  $\lambda$  is the decay constant ( $s^{-1}$ ),  $N$  is the number density of target atoms ( $cm^{-3}$ ),  $\sigma$  is the production cross section ( $cm^2$ ) and  $\phi$  is the flux density ( $cm^{-2}s^{-1}$ ) of the incident particles. On the right hand side of this equation, the first term represents the loss of radionuclides through decay during the irradiation while the second term represents the increase of radionuclides through the production reaction under consideration. The equation has the following solution for  $0 < t < t_i$ :

$$\nu(t) = \frac{N\sigma\phi}{\lambda} (1 - \exp(-\lambda t)) \quad (4.16)$$

The specific activity induced in the material as a function of time during the irradiation is given by  $a(t) = \lambda n(t)$ , hence

$$a(t) = N\sigma\phi (1 - \exp(-\lambda t)) \text{ for } 0 < t < t_i \quad (4.17)$$

When the irradiation reaches to an end ( $t = t_i$ ), the specific activity will be

$$a(t_i) = N\sigma\phi (1 - \exp(-\lambda t_i)) \quad (4.18)$$

so that the specific activity as a function of time is characterized by a buildup from zero towards the saturation value equal to  $N\sigma\phi$  for an infinitely long irradiation. After the irradiation has stopped ( $t > t_i$ ), the specific activity as a function of the cooling time,  $t_c = t - t_i$ , will obviously decay exponentially and is defined by the activation equation:

$$a(t_c) = N\sigma\phi (1 - \exp(-\lambda t_i)) \exp(-\lambda t_c) \quad (4.19)$$

The activity evolution for four radionuclides as function of the irradiation and cooling time is shown in Figure.

#### Activation formalism

In more complex cases including decay chains, the formalism has to be extended. The specific activity of a radionuclide  $b$  induced by a loss rate of one primary beam particle per second can be described as

$$A_b = \sum_r \sum_e T_{br} P_{re} m_e \quad (4.20)$$

where  $m_e$  stands for the weight fraction for the element  $e$ ,  $r$  shows all the radionuclides that are directly produced from the elements of the material. The matrix  $T_{br}$  indicates the time evolution and is defined in a following equation. The production rate of an radionuclide  $r$  from an element  $e$  for a

loss rate of one primary beam particle per second is given by the matrix

$$P_{re} = \frac{N_A}{M_e} \sum_{i=p,n,\gamma,\pi^{(+)},\pi^{(-)}} \int \Phi_{i(E)} \sigma_{(i,e,r)}(E) dE \quad (4.21)$$

where  $N_A$  is Avogadro's constant and  $M_e$  is the atomic weight for the element e. The sum is extended over protons (p), neutrons (n), charged pions ( $\pi^+$ ,  $\pi^-$ ) and photons  $\gamma$ .

With this definition the natural isotope abundances for each element e are taken into account, i.e. the cross section  $\sigma_{i,e,r}(E)$  is an abundance weighted average of the cross sections of each isotope of element e. Additionally,  $\Phi_i(E)$  is the radiation fluence for the various secondary particles ( $i = p, n, \gamma, \pi^+, \pi^-$ ) generated by one primary beam particle per second. The expression  $\sum_e P_{re} m_e$  corresponds to the production rate of the radionuclide r in the entire component for a loss rate of one primary beam particle per second. [48] The time evolution of the specific activity of radionuclide b, i.e. the build-up of radionuclide r and the full decay chain leading to radionuclide b, is explained by the matrix  $T_{br}$ . For an irradiation profile of a constant irradiation period of duration  $t_{irr}$  followed by a cooling time of duration  $t_{cool}$ , the time evolution  $T_{br}$  will be

$$T_{br}(t_{irr}, t_{cool}) = \sum_{c,r \rightarrow b} \int_0^{t_{irr}} \sum_{m=1}^{j_c} c_m^c e^{-\lambda_m^c} ((t_{cool} + t_{irr} - t_0) dt_0 \quad (4.22)$$

and this is equal to:

$$\sum_{c,r \rightarrow b} \sum_{m=1}^{j_c} \frac{c_m^c}{\lambda_m^c} (e^{-\lambda_m^c} ((t_{cool} + t_{irr}))) = \sum_{c,r \rightarrow b} \sum_{m=1}^{(j_c)} \frac{c_m^c}{\lambda_m^c} e^{-\lambda_m^c t_{cool}} (1 - e^{-\lambda_m^c t_{irr}}) \quad (4.23)$$

and this is equal to:

$$\sum_{c,r \rightarrow b} \sum_{m=1}^{(j_c)} \frac{c_m^c}{\lambda_m^c} e^{-\lambda_m^c t_{cool}} (1 - e^{-\lambda_m^c t_{irr}}) \quad (4.24)$$



where  $c$  runs over all decay chains starting from radionuclide  $r$  leading to radionuclide  $b$  and  $j_c$  is the number of radionuclides in a given decay chain  $c$ . The  $\tilde{\lambda}_m^c$  is the total decay rate of the  $m^{th}$  radionuclide in decay chain  $c$ . The  $\lambda_m^c$  is the partial decay rate of the  $m^{th}$  radionuclide in the given decay chain  $c$  and the coefficient  $c_m^c$  is the bateman coefficient of the  $m^{th}$  radionuclide in decay chain  $c$  given by

$$c_m^c = \frac{\prod_{i=1}^{j_c} \tilde{\lambda}_i^c}{\prod_{i=1, i \neq m}^{j_c} (\lambda_i^c - \lambda_m^c)} \quad (4.25)$$



## Chapter 5

# The Monte Carlo particle interaction, transport code FLUKA and Dorian code

### 5.1 A brief introduction to the Monte Carlo method

The Monte Carlo (MC) method applies probability theories and statistical methods to model physical/mathematical systems and processes that are stochastic in nature. The official invention was back to 1946, in the framework of the Manhattan project at Los Alamos National Laboratory, where S. Ulam devised it for thermonuclear weapons research. Recognizing the significance of this invention, von Neumann attempted to implement the method computationally, using rudimentary “pseudo random numbers” generation techniques and the early computer ENIAC to model thermonuclear reactions. As the project was under governmental secrecy, a code name had to be attributed. N. Metropolis suggested naming it “Monte Carlo”, alluding to the method’s random nature and the gambling addiction of S. Ulam’s uncle. Despite its official date of discovery, E. Fermi had already been ap-

plying it successfully to neutron moderation for the prior 15 years, albeit in a limited manner due to the unavailability of heavier computational power. In fact, even before the advent of computers the method was already applied. Some historical examples being Buffon's needle problem in 1777 and later Laplace's  $\pi$  determination method. With the growth of computational power, MC methods became more popular for different research topics. The first stage of MC method application is the definition of the problem in mathematical terms, so that one can calculate the quantities of interest. In order to do so, a statistical interpretation of the problem is performed. The MC mathematical core is the notion of moments of a distribution and the Central Limit Theorem. The former states that, for a variable  $x$  and probability density function  $f(x)$ , the mean of a function  $g(x)$  over an interval  $[a,b]$  is

$$\bar{g}(x) = \frac{\int_a^b g(x)f(x)dx}{\int_a^b f(x)dx} \quad (5.1)$$

By applying the normalized probability density function  $\mathcal{F}(x)$  as

$$\mathcal{F}(x) = \frac{f(x)}{\int_a^b f(x)dx} \quad (5.2)$$

and for  $\bar{g}(x)$

$$\bar{g}(x) = \int_a^b g(x)f(x)dx \quad (5.3)$$

where if  $g(x) = x$ , one directly obtains

$$\bar{x} = \int_a^b x\mathcal{F}(x)dx \quad (5.4)$$

In the same way, the mean of a distribution can be extended to multiple dimensions, based on various probability density functions. For example integrating over  $g(x,y,z)\mathcal{F}(x)\mathcal{G}(y)\mathcal{H}(z)...$  This is usually beneficial, consid-

ering that calculations of multidimensional integrals are usually impractical, but necessary for solving physical problems. The sampling  $\mathfrak{G}_N$  of  $N$  values of  $g$ , for example  $g_i(x_i, y_i, z_i)$ , while averaging over the number of times this process occurs

$$\mathfrak{G}_N = \frac{\sum_1^N g_i(x_i, y_i, z_i)}{N} \quad (5.5)$$

leads to a mean value for the solution. In the event that these terms follow the distribution of  $g$ , then the integration process corresponds to an analogue MC simulation. Regarding the Central Limit Theorem, it is the centerpiece for the MC method. It states that if  $N$  is sufficiently large, the normalized  $\mathfrak{G}_N$  value of  $N$  independent random variables identically distributed will tend to a normal distribution (except in cases when the second central moment is infinite), with mean  $\bar{g}$  and variance  $(\sigma_g^2/N)$ . Therefore:

$$\lim_{N \rightarrow \infty} \mathfrak{G}_N = \bar{g} \quad (5.6)$$

hence,

$$\lim_{N \rightarrow \infty} \mathcal{P}(\mathfrak{G}_N) = \frac{1}{\sqrt{\frac{2\pi}{N}\sigma_g^2}} e^{-\frac{(\mathfrak{G}_N - \bar{g})^2}{2\sigma_g^2/N}}. \quad (5.7)$$

Consequently, MC can be used to solve integrals with multiple dimensions throughout sampling from appropriate stochastic distributions, becoming in a sense a “mathematical experiment”. Convergence will eventually not depend on the number of variables  $n$ , as in general integration methods, in which convergence is governed by  $N^{-1/n}$ , but on the number of samples as  $\sigma \propto N^{-1/2}$  instead. Therefore, for problems with  $n > 2$ , which is the rule in particle transport, MC becomes extremely convenient and is often the most advantageous technique for scenarios of dimensionality above four.

#### **Application of Monte Carlo to particle interaction and transport**

The MC method is particularly well suited for particle transport problems, as these are systems of great complexity and radiation interaction is ultimately stochastic in nature. MC allows the user to set up a virtual framework

where particle detection can be performed in a controlled environment and with access to all physics processes, with the possibility of repeating the virtual experiment as often as required. Irrespective of the particle type, the baseline of either particle beams or radiation source products' transport should always be sound physics models, in order to replicate all physical mechanisms involved. This of course assuming that the geometry, materials and hence the real experimental setup, is properly defined and its properties replicated. When applied to particle transport, the MC method relies on “pseudo random numbers” and sampling techniques to model the transport of particles throughout media. Random sampling techniques are paramount in MC codes, since given a probability density function  $F(x)$  of a variable  $x$ , samples of  $x$  should be generated accordingly. True random numbers can neither be predicted nor reproduced, being generated by random physical processes (e.g. nuclear decay events). MC codes resort instead to sequences of random numbers generated by algorithms named “pseudo random numbers”, while they are practically random with respect to the correlation they are still reproducible. They still exhibit periodicity, albeit with prolonged periods (e.g.  $10^{61}$ ), proceeding from an initial number or “seed”, whose changing implies a different random number sequence generation. Regarding the MC method's application, since it dwells with stochastic problems, it requires modeling of random variables. In particle transport this becomes essentially an integration problem of probability density function in a phase space with multiple variables. As a primary particle travels throughout matter it is evaluated at certain steps, its “fate” (e.g. fission) is then decided by random selection from the given  $F(x)$ . For an oversimplistic case, concerning the photon beam attenuation, one may attempt to exemplify based on

$$p(x)dx = \Sigma e^{-\Sigma x} dx \quad (5.8)$$

where  $p(x)$  is the probability density function of the photon travelling a distance  $x$ . In its turn,  $x$  varies between  $0 < x < \infty$ , governed exponentially by the macroscopic cross section  $\Sigma$ . By integrating, an estimation of the

mean free path  $\lambda(x)$  can be obtained as

$$\lambda(x) = \int_0^\infty xp(x)dx = \frac{1}{\Sigma} \quad (5.9)$$

In a MC approach, the problem would be rewritten as

$$\int_0^x \Sigma e^{(-\Sigma y)} dy = \zeta \quad (5.10)$$

with  $0 \leq \zeta < 1$  being a radomly generated number. Solving the integral, one would obtain

$$1 - e^{-\Sigma s} = \zeta \leftrightarrow s = -\frac{\ln(1 - \zeta)}{\Sigma} \quad (5.11)$$

Thus, starting from a “pseudo random number”  $\zeta \in [0, 1]$  the distance travelled by a photon can be computed. However, the aforementioned example is oversimplistic as MC methods should reproduce the different phenomena during particle transport (e.g. solving the Boltzmann transport equation) from its creation until its destruction, transformation, absorption or discard by any transport- imposed condition. Also, in the event that secondary particles are produced as a result of interactions, they are to be placed onto a stack, and in turn transported iteratively until a new primary particle is considered again. [36], [39], [38], [47]. Below there is a simplified example of a neutron traversing a certain material, with the macroscopic cross section given as

$$\Sigma = \Sigma_a + \Sigma_s \quad (5.12)$$

with  $\Sigma_a$  and  $\Sigma_s$  referring to the absorption and scattering macroscopic cross sections. Once again, the expected distance at which an interaction occurs by the equation in the previous page, and the mean free path  $\lambda = 1/\Sigma$

At this point, since there are two types of macroscopic cross sections to be considered, the interaction will result from an interplay between absorption and scattering probabilities,  $\zeta_a$  and  $(1 - \zeta_a)$ , respectively. The outcome

becomes analogue to the schematic description in the next figure:

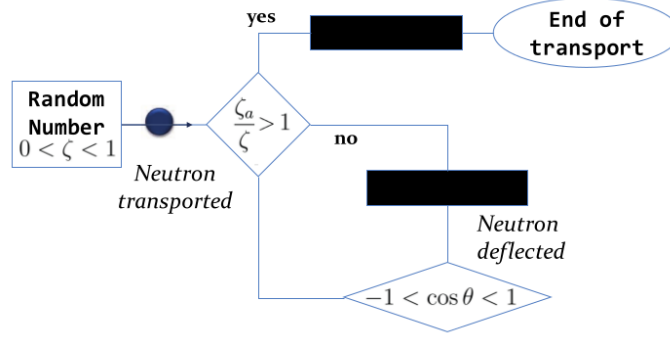


**Figure 5.1:** (Over)simplistic example of Monte Carlo application to neutron transport

The scattering happening with a polar angle  $\theta$ , assuming an isotropic scenario, given an uniform distribution for  $\cos\theta \in [-1, 1]$  as

$$\cos\theta = 2\zeta - 1, \phi = 2\pi\zeta \quad (5.13)$$

in the center of momentum frame and with an azimuthial angle  $\phi, \zeta \in [0, 1]$  being a random number. From then onward, the particle is retracked, until the next interaction occurs throughout the geometry defined. Obviously, there should be additional parameters taken into consideration in order to obtain a realistic result (e.g. absorption by capture or fission). Also, scattering can be elastic or inelastic, possibly entailing secondary particle production, which in turn would need to be tracked.

In the context of particle physics the number of particles in a phase space, or phase space density  $n(x, y, z, p_x, p_y, p_z, t)$ , is the key parameter to describe particle transport. Other components (e.g. spin) could also be added to those dimensions, if deemed relevant. The product  $n \vec{u}$  translates into the angular flux  $Ps\dot{i}$ :

$$\Psi = \frac{d\Phi}{dt dE d\vec{\Omega}} = \Phi_E \cdot \vec{\Omega}. \quad (5.14)$$

The above mentioned notion is a building block for particle transport,



being essentially the fluence ( $\Phi$ ) derivative carrying the information on time, energy and direction over the phase space. The resulting fluence is given as

$$\int_E \int_{\vec{\Omega}} \int_t \dot{\Phi}_{E\vec{\Omega}} dt d\vec{\Omega} dE. \quad (5.15)$$

Evaluating the quantity using the Monte Carlo method requires considering not only the transport of particles, but also the interaction and consequently secondary production. This is accomplished using the Boltzmann transport equation, which can be regarded as a balance equation that, for any phase space point, evaluates the particle density as a result of ingoing and outgoing terms.

$$\frac{1}{v} \frac{d\Psi(x)}{dt} + \vec{\Omega} \cdot \nabla \Psi(\chi) + \Sigma_t \Psi(\chi) - \mathcal{S}(\chi) = \int_{\Omega} \int_E \Psi(\chi) \Sigma_s(\chi' \rightarrow \chi) d\chi' dE d\Omega \quad (5.16)$$

On the left side, the first term describes the variation of angular flux (e.g. altered as a consequence of decay). As for the second term, it accounts for flux changes through motion without change of energy/direction, while the third term denotes absorption by accounting for the total macroscopic cross section ( $\Sigma_t$ ). The particle sources contribution is accounted for with the negative term  $\mathcal{S}(\chi)$ . On the other side, scattering is considered using  $\Sigma_s$ , the macroscopic scattering cross section. [43], [41], [42], [58], [32], [45], [3], [46], [24]. This latter represents the changes in flux due to either energy or directional changes of particle position. The evaluation of cross section data in Monte Carlo codes often resorts to data libraries, for different energies, particle types and materials. Depending on the phase space of interest and the quantity to be evaluated, various estimators can be considered and some examples will be provided in the next section. Various detector elements can be used to provide a result (estimate), in a mesh, for instance. The variance of the mean of  $x$  thus calculated, in  $N$  batches, comes as

$$\sigma_{<x>}^2 = \frac{1}{N-1} \left[ \frac{\sum_1^N n_i x_i^2}{n} - \left( \frac{\sum_1^N n_i x_i}{n} \right)^2 \right] \quad (5.17)$$

with  $x_i$  representing the average P N of  $x$  and  $n_i$  being the number of particle histories in the  $i^{th}$  batch. On the other hand,  $n = \sum_i^N n_i$  is the total number of histories in the  $N$  batches. As a result of the Central Limit Theorem, if the system convergence criteria are met, the sample average will tend to the actual distribution if  $N \rightarrow \infty$ . In the domain of medical physics and hadron therapy in particular, Monte Carlo has gained popularity and its models have contributed to:

- Detector development for image monitoring (e.g. prompt  $\gamma$ , PET) and dose delivery optimization purposes
- A better understanding of ion beam interactions with matter and their secondary particle production
- Improvements of radiobiological models
- General accelerator design and beam line development
- TP validation and optimization

## 5.2 The FLUKA code

FLUKA (FLUktuierende KAskade) is a general purpose Monte Carlo code tool for the simulation of particle transport and interactions with matter, covering an extended range of applications spanning from proton and electron accelerator shielding to target design, calorimetry, activation, dosimetry, detector design, Accelerator Driven Systems, cosmic rays, neutrino physics, radiotherapy etc. This tool has its roots in radiation protection studies at high energy accelerators and thus contains all features needed in this area of application. The FLUKA code can simulate with high accuracy the interaction and propagation in matter of about 60 different particles, including

photons and electrons from 1 keV to thousands of TeV, neutrinos, muons of any energy, hadrons of energies up to 20 TeV (up to 10 PeV by linking FLUKA with the DPMHET code) and all the corresponding antiparticles, neutrons down to thermal energies and heavy ions. The program can also transport polarised photons (e.g., synchrotron radiation) and optical photons. Time evolution and transport of radiation emitted from the decay of unstable residual nuclei can be performed on-line. [6]

### 5.2.1 Physical models and features

FLUKA uses physical models for hadron inelastic nuclear interactions, elastic scattering, nucleus-nucleus interactions, transport of charged hadrons and muons, low energy neutrons ( $<20$  MeV), electrons, photons, optical photons and neutrinos. The module used for hadronic interactions is called PEANUT (PreEquilibrium Approach to Nuclear Thermalization) and comprises a phenomenological description (Dual Parton Model-based Glauber-Gribov cascade) of high-energy interactions (up to 20 TeV), a generalized intra-nuclear cascade and pre-equilibrium emission models as well as evaporation, fragmentation, fission, and de-excitation by gamma emission models. Ions interactions are simulated through interfaces with different codes based on models suitable for certain ranges of energy (DPMJET3 above 5 GeV/nucleon, rQMD-2.4 between 0.1 and 5 GeV/nucleon, Boltzmann Master Equation below 0.1 GeV/nucleon). The interface with DPMJET3 also allows the simulation of minimum-bias proton-proton and heavy ion collisions at LHC energies which enormously facilitates calculations of stray radiation fields around LHC experiments. The transport of neutrons with energies below 20 MeV is performed by a multi-group algorithm based on evaluated cross section data (ENDF/B, JEF, JENDL, etc.) binned into 260 energy groups, 31 of which are in the thermal energy region. For a few isotopes ( $^1\text{H}$ ,  $^6\text{Li}$ ,  $^{10}\text{B}$ ,  $^{14}\text{N}$ ) point-wise cross sections can be optionally used during transport. The detailed implementation of electromagnetic processes in the energy range between 1 keV and 1 PeV is fully coupled with the models for hadronic

interactions. Many variance reduction techniques are available in FLUKA, among others, weight windows, region importance biasing as well as leading particle interaction length and decay length biasing. FLUKA has one-of-a-kind capabilities for studies of induced radioactivity, specifically with regard to radionuclide production, their decay and the transport of residual radiation. Particle transport and interaction of prompt and residual radiation are simulated in parallel based on microscopic models for nuclide production and a solution of the Bateman equations for activity build-up and radioactive decay. The decay radiation and its associated electromagnetic cascade are internally flagged as such in order to distinguish them from the prompt cascade. This allows the user to apply different transport thresholds and biasing options to residual and prompt radiation and to score both independently. Particle fluences can be weighted on-line with energy-dependent conversion coefficients in order to obtain the effective dose or the ambient dose equivalent. Prompt and residual dose equivalent can therefore be calculated in three-dimensional meshes, the latter for arbitrary user-defined irradiation and cooling profiles. [8]

**Combinatorial geometry** FLUKA in order to describe the geometry of the simulation is using the combinational geometry model that is based on two fundamental concepts: bodies and regions. Bodies are defined as convex solid bodies, e.g. portions of space delimited by surfaces of first (planes) or second (quadratics), infinite cylinders (circular and elliptical) and planes (half-spaces). An advantage of using infinite bodies is that they make input preparation and modification much easier and less error-prone. Regions are defined as combinations of bodies by using the Boolean operators like union, difference and intersection. Each region is not necessarily simply connected, since it can be made of two or more non contiguous parts, but must be of homogeneous material composition. FLUKA provides the user with a geometry debugger in order to facilitate the procedure of building the geometry with the capability of finding undefined points, i.e. points which are not included in any defined region, as well as multiple defined points,

i.e. points which are included in more than one region. All the regions are surrounded by an infinitely absorbing material ("blackhole"), which absorbs all the escaping particles. A repetition capability ("lattice") is available to avoid the multiple description of repetitive structures. Only one module has to be defined, which can be re-iterated as many times as required. This allows defining geometries, containing up to thousands of different regions, by using only a small number of region and body definitions.

### 5.2.2 Biasing

FLUKA is able to perform fully analogue particle transport calculations. However, in many cases of non-uniform radiation fields only on a very small fraction of all histories contributes to the desired response in the regions of interest. In these cases, the user's concern might be to estimate the desired response in the most efficient approach. This can be achieved by the replacement of the actual physical problem with a mathematically equivalent one, i.e. having the same solution but faster statistical convergence. This replacement technique is called biasing. When the limit of the number of histories tends to infinity, the values of all calculated quantities tends exactly to the same averages in the analogue and in the corresponding biased calculation. Namely, biasing is mathematically correct and involves no approximation. Nonetheless, an acceleration of convergence in specific regions of phase space (space/energy) will generally give the disadvantage of a slower convergence in other regions. Due to the fact that an actual calculation does not use an infinite number of particles, but it is necessarily truncated after a finite number of histories, results must be judged accordingly. [4]

**Importance biasing** The simplest and safest biasing option in FLUKA is importance biasing. Each geometry region can be assigned an importance, particularly a number between  $10^{-4}$  and  $10^5$ , proportional to the contribution that particles in that region are expected to give the desired result: the number of particles moving from a region to the neighbouring one will increase or decrease accordingly to the ratio of importance values assigned

to both regions and the particle statistical weight will be modified inversely so that the total weight will remain unchanged. For instance, in a simple, mono-dimensional attenuation problem, the importance is often set at the inverse of the expected fluence attenuation factor for each region, in order that the fluence value is constant with the increasing shielding thickness. The equivalent dose attenuation by a thick shielding is in first order described by an exponential attenuation:

$$\exp - \frac{z}{\lambda} \quad (5.18)$$

where  $z$  (in  $gcm^{-2}$ ) is the shielding thickness and  $\lambda$  (in  $gcm^{-2}$ ) is the attenuation length typical of the shielding material. Since each particle (according to its energy) contributes differently to the total equivalent dose, the biasing was built in order to maintain constant the scored dose and not the particle fluence. The importance value of the inner shielding region can start from  $10^{-4}$  and increase while moving outwards. Every region is given an importance value equal to the value of the previous adjacent one multiplied by a factor  $R$ , which is the inverse of the expected attenuation in the considered region

$$R = \frac{1}{\exp - \frac{\Delta z}{\lambda}} = \exp\left(\frac{\Delta z}{\lambda}\right) \quad (5.19)$$

where  $\Delta z$  (in  $gcm^{-2}$ ) is the shielding thickness of the considered region and  $\lambda$  (in  $gcm^{-2}$ ) is the attenuation length. Once  $10^5$ , the highest importance possible in FLUKA, is reached in a certain region, all the following regions are given this same constant value of importance, which means that no biasing is applied.

### 5.2.3 Scoring

Results in a Monte Carlo calculation can be obtained by adding up the contributions to the “score”, or “tally” of a detector defined by the user. A detector is the Monte Carlo equivalent of a measurement instrument. Each detector, also denoted as “estimator”, is designed to estimate one or more

radiometric quantities, and the final score is a statistical estimation of the average value of the corresponding population of primary particles. As in experimental measurements, it is possible to calculate a standard deviation by running several independent calculations. There are different input options corresponding to different types of detectors. The simplest one is SCORE which provides energy deposition (proportional to absorbed dose) or star density in every region of the geometry. “Stars” is an old name for inelastic hadron reactions which derives from early experiments with nuclear emulsions. The same quantities can be scored in a geometry-independent uniform spatial mesh, called a “binning”, by means of the option USRBIN. There are several types of binnings: Cartesian, 2D-cylindrical, 3D-cylindrical and even more complex phase space structures. In addition to dose and star density, it is possible to use USRBIN to score weighted particle fluence distributions. USRBIN results are often displayed as colour plots where each colour corresponds to a pre-defined colour-coded range of values. Fluence, averaged over the volume of a given geometry region, can be calculated with options USRTRACK. It is a “track-length estimator” (it estimates fluence as volume density of particle trajectory lengths). USRTRACK works also in vacuum and provides fluence differential energy spectra. Production of residual nuclei can be obtained with command RESNUCLEI. The results, which are closely related to induced activity and dose rate from activated components, can include nuclei produced in low-energy neutron interactions, provided the corresponding information is available in the neutron cross-section library for the materials of interest. [6], [4], [8]

## 5.3 The DORIAN code

The estimation of residual dose rates is something very significant for the radiation protection and as in our case for the work and dose planning of interventions in an accelerator facility. The DORIAN (DOse Rate Inspector and ANalyser) is a method of two steps, that splits the computation of residual dose rates in three steps. The DORIAN code is written in the python and exposes scripting interface. The FLUKA Monte Carlo simulation code can provide calculations for residual dose rates for a given irradiation profile and a number of cooling times. At this point, in order to obtain the dose rate for another irradiation profile or another set of cooling times, the whole simulation has to be runned again. There is no direct method to assess the contribution of the different geometrical regions and different radionuclides to the dose rate. The FLUKA simulations for the second step, their execution and the combination of the results as well as the analysis in the third step are highly automated and costumizable. [26]

### 5.3.1 Calculation of residual dose rates

**First step of the DORIAN code.** In the first step, the FLUKA simulation of the primary process of interest is performed and all the information concerning the creation of radionuclides is recorded as an input in the second step. This is done with a DORIAN supplied USRRNC FLUKA user routine that has been linked to the FLUKA code. Every time a radionuclide is created, this routine is called during the simulations. It writes the atomic number, the mass number and a flag for an isomeric state of the produced radionuclide, the coordinates of the creation point, the region number, the weight of the creation event and a flag indicating whether or not the creation was caused by a neutron with an energy below 20 MeV to a dedicated output file. Furthermore, this flag allows the DORIAN to omit calls to the USRRNC user routine by the direct residual dose rate algorithm of FLUKA. Therefore it is irrelevant for DORIAN wheteher an irradiation profile and cooling times



have been directly specified in the first step. If the simulation of this first step is split over multiple cycles, the output files are merged for the second step.

**Second step of the DORIAN code** In the second step, FLUKA simulations are performed for the decay of the various radionuclides produced in the first step and the resulting dose-per-decay contributions are computed. First, the content of the dedicated output file from the first step is analyzed. For each of the various radionuclides produced in each of the different regions, the corresponding content of the file is selected and written to a separate output file, denoted thinned output file. In addition, transformations can be applied to the content of the output file from the first step. Regarding the geometrical transformations, the geometrical coordinates of the generation points of radionuclides can be transformed. A typical application would be the translation/ rotation of the points for specific regions. Together with a corresponding modification of the geometry for the second step, the movement of an object to a different location after the end of the irradiation can be simulated. Moreover about the branching ratios, the FLUKA code assumes a branching ratio  $\frac{50/100}{50/100}$  between ground state and the first isomeric state for radionuclides with isomeric states. A correction can be applied to reflect energy averaged branching ratios found in JEFF 3.1.1 library. Last but not least as far as the suppression, the calculation of the contributions for certain radionuclides or for certain regions can be suppressed by the user in case it is expected that these contributions are negligible for the desired quantities. For example, radionuclides with a half life significantly shorter than the cooling times of interest. During the simulation of the second step, a DORIAN supplied SOURCE user routine, that has to be linked to the FLUKA code, reads the corresponding thinned output file, for example the selection of the production points of the first step, and then generates radioactive decay events at these positions. For each radionuclide that is produced in the first step, its generation positions are used as decay positions in the second step for the radionuclide itself and for all radionuclides in all decay chains that

originate from it.

The FLUKA input files for the second step are based on information and meta-information stored in the FLUKA input file of the first step. To generate them, a dedicated *define* statement is prefixed to the input file from the first step together with cards that specify the given radionuclide and that are necessary to simulate the transport of the radiation produced by the FLUKA generated decays of the given radionuclide. This means that only a single FLUKA input file has to be maintained. In addition the content of the input files for the second step can be changed with respect to the first step by using the preprocessor capabilities of FLUKA. Important examples are changes in the geometry and material assignments (possible also together with geometrical transformations of the output file of the first step) as well as the adjustment of the biasing scheme to the residual radiation transport instead of the prompt radiation transport that is currently not possible in FLUKA. All the FLUKA simulations of the second step are automatically executed by DORIAN on a user defined numbers of cores. [26]

### Third Step of DORIAN code

As it says above in the second step, the contribution of the various radionuclides is computed. In the third step these various radionuclides are combined according to a specified irradiation profile and cooling time, yielding the residual dose rate.

The dose rate  $d$  is obtained by weights sum

$$\frac{dD}{dt} = d = \sum_r \sum_b d_{b,r}^{S2} \frac{N_{i_{b,r}}^{S1}}{W_{tot}^{S1}} \frac{W_{b,r}^{S2}}{N_{b,r}^{S2}} T(b, i_b, r) \quad (5.20)$$

where  $d_{b,r}^{S2}$  denotes the dose per decay computed in the second step for radionuclide  $b$  and region  $r$ . The factors that enter the normalization are the quantity of the first simulation to be normalized to, i.e. either the number of primaries or the sum of the weights of all primaries, denoted by  $W_{tot}^{S1}$ , the number of productions  $N_{i_{b,r}}^{S1}$  in the first step of the starting radionuclide  $i_b$  of the decay chain leading to radionuclide  $b$ , the sum of the weights of

the primaries  $W_{b,r}^{S2}$  and the number of primaries  $N_{b,r}^{S2}$  in the second step for the simulation of the decays of radionuclide  $b$  in region  $r$ . The time evolution  $T(b, i_b, r)$  for the starting radionuclide  $i_b$  of the decay chain leading to radionuclide  $b$ , that depends on the irradiation profile and the cooling time, also has to be taken into account. Arbitrarily complex step-wise irradiation profiles can be specified and decay chains are fully taken into account. This is done by integration of the solution of the Bateman equations.

It is possible to apply different irradiation profiles or even if and the cooling times for different regions. A possible application is the estimation of the dose rate in the vicinity of internal dumps that are regularly replaced during preventive maintenance. Each summand in the equation is available for analysis. The relevance of the various contributions to the total dose rate can be assessed.

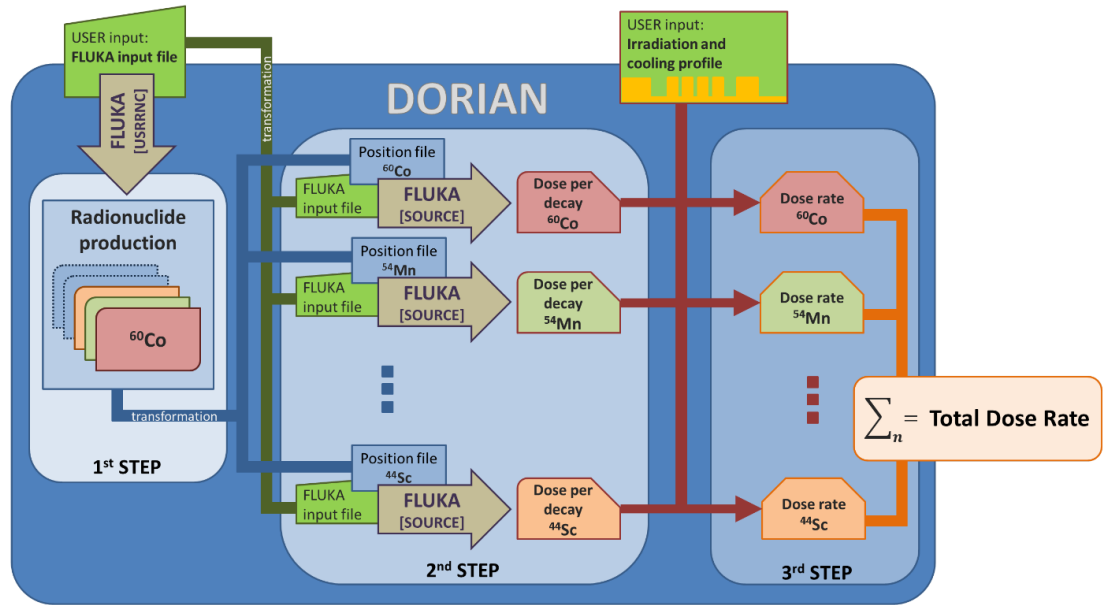


**Figure 5.2:** Schematic representation of the work-flow for the three steps of the calculation of residual dose rates the DORIAN code.[26]

### 5.3.2 Verification

In order to verify the correctness of the DORIAN code with respect to the FLUKA code, a simulation of a proton beam hitting a copper target has been performed. There is a cylinder copper target, surrounded by vacuum. This cylinder has radius of 5 cm and length 50 cm. The proton beam has momentum 1 GeV/c. This proton beam, is impinging onto the target at the center of the circular front face. The dose rate at a distance of 50 cm upstream of the impact face after one year of irradiation with unit beam intensity. For instance, one proton per second, computed by DORIAN as a function of the cooling time is compared to the prediction of a direct FLUKA simulation. Furthermore, the contributions of the various radionuclides to the dose rate computed by DORIAN are shown. Except from the statistical fluctuations for cooling times up to a couple of hours, the values computed with DORIAN are FLUKA simulation values very well. The dose rate is dominated by  $^{56}\text{Co}$  and  $^{58}\text{Co}$  for cooling times from 1 hour to 6 months, by  $^{54}\text{Mn}$  for cooling times around one year and by  $^{60}\text{Co}$  for cooling times between two years and 10 years.

### 5.3.3 Advanced applications

In an example of a target irradiated in a concrete bunker and then moved to an alcove. The entrance can be closed with movable marble walls. The capabilities of the DORIAN code can be demonstrated by this example. In the verification simulation, the copper target is a cylinder with radius of 5 cm and length of 50 cm. The proton beam is impinging onto the target at the center of the circular front face with an intensity of  $10^{10}$  protons per second and with momentum of 1 GeV/c. The horizontal dimensions of the concrete bunker can be seen in the next figure, the height of the bunker is 240 cm and the target is placed at the center of the bunker. The marble walls are 10 cm thick.

**Dose rate for a target moved to an alcove**

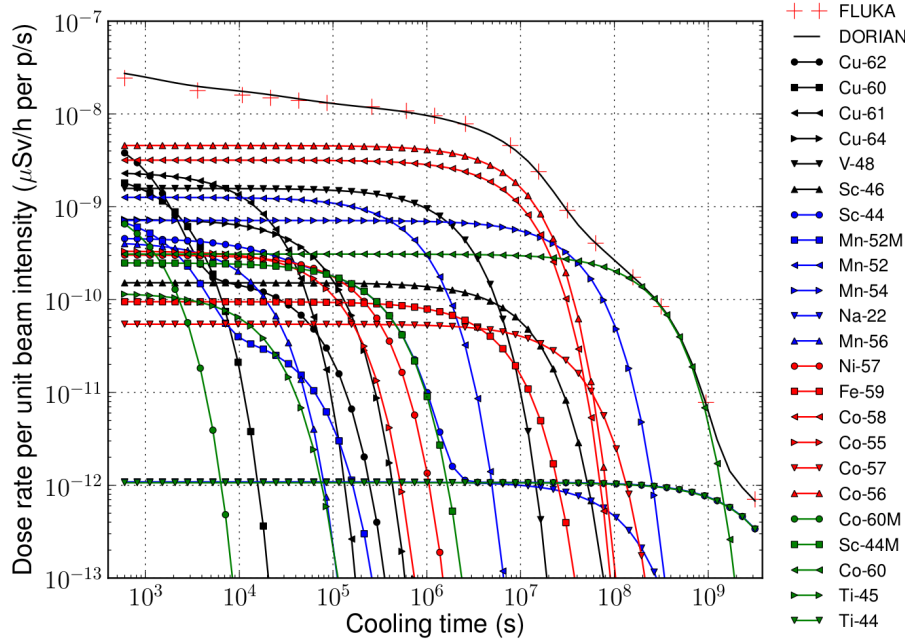


**Figure 5.3:** Comparison of the dose rate at a distance of 50 cm upstream of the impact face of a copper target hit by 1 GeV/c proton beam computed by DORIAN with the values predicted by direct FLUKA calculation. The dose rates are shown as a function of the cooling time after an irradiation of 1 year. The contributions of various radionuclides are shown for the DORIAN calculations. [26]

The residual dose rate is shown after an irradiation of 1 year followed by a cooling time of 1 day. There is the case that the target is remaining at its position during irradiation and the case that the target is moved 320 cm to the alcove parking position after irradiation, including the closure of the 10 cm marble shielding at the entry to the alcove. What is worth to be observed is the self shielding effect of the target, the residual dose rate contribution from the activation of the concrete and the effect of the marble shielding.

#### Minimum required cooling time before an intervention

The minimum required cooling time before the intervention has to be computed as a function of the previous irradiation time, in the case of planning an intervention near the target in detail. The threshold dose rate to authorize the intervention is  $200 \mu\text{Sv/h}$  in the distance of 25 cm upstream

of the impact face of the copper target in the alcove parking position. This is based in the geometrical setup of the target moved to the parking position in the alcove together with a work and dose planning of the intervention. The irradiation profile and cooling time can be varied. The cooling time, at which the dose rate at the location of the intervention has dropped to  $200 \mu\text{Sv}/h$  for a give irradiation profile, can be computed by a root finding algorithm (SciPy implementation of the Brent algorithm). Below is shown the minimum required cool-down time as a function of the irradiation time for several years of operation of the facility. Moreover we can say that, the work and the dose planning could be a program that calculates with the help of DORIAN the most important radiological quantities for the intervention.

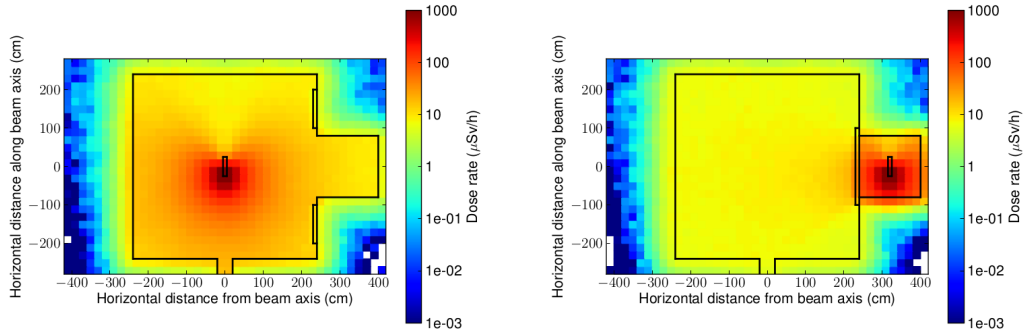


**Figure 5.4:** Residual dose rate maps for copper target placed in a concrete bunker and hit by 1 GeV/c proton beam computed by DORIAN. The dose rates are shown after an irradiation of 1 year followed by a cool-down period of 1 day. Residual dose rates are shown both for the target remaining at its position during irradiation and for the target moved to the alcove parking position after irradiation including the closure of a 10 cm marble shielding at the entry to the alcove. In the right figure the target is at the target irradiation position and in the left image, the target is at alcove parking position. [26]

### 5.3.4 Implementation

The DORIAN code is written in the python programming language, with a very compact code base, that consists of 300 lines of code plus 1000 lines of code for the time evolution. Therefore the DORIAN code automatically exposes a scripting interface. The dose-per-decay output files are converted to numPy arrays, making the weighted summation of the previous equation very fast. The creation of the FLUKA simulations for the second step is highly automated, as well as their execution and the results combination and analysis in the third step, which is happening in a very user-friendly and customizable way.

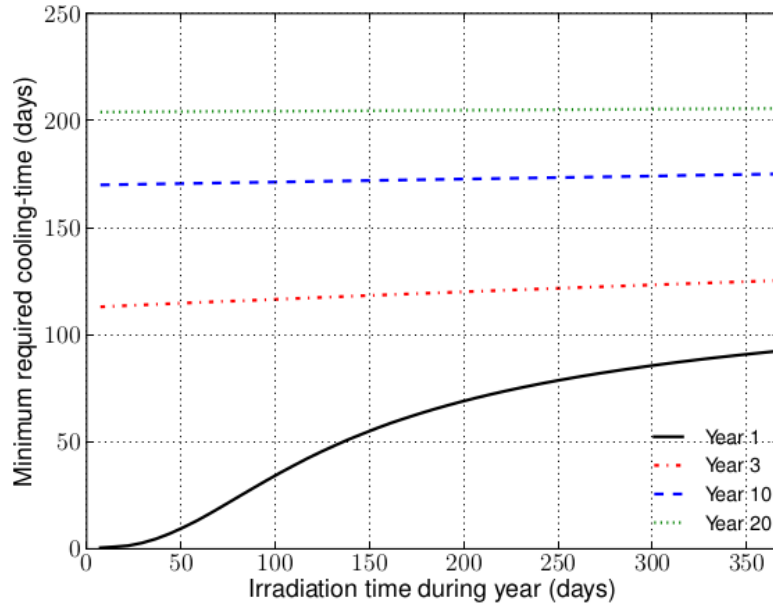


**Figure 5.5:** Minimum required cooling time before an intervention for different years of operation of the facility. The threshold for authorization is  $200 \mu\text{Sv/h}$  at a distance of 25 cm upstream of the impact face of the copper target in the alcove parking position. [26]





# Chapter 6

## Residual ambient dose equivalent rate measurements

As is already mentioned in the previous chapters, the CHARM facility (CERN High energy AccelRator Mixed field) has been constructed in 2014. It is located in the CERN East Experimental Area with the purpose to study radiation effects on electronic components. The primary beam is a proton beam with momentum of 24 GeV/c and a maximum average beam intensity of  $6.7 \cdot 10^{10}$  protons per second with a maximum pulse intensity of  $5 \cdot 10^{11}$  protons per pulse and a respective pulse length of 350 ns. CHARM's proton beam comes from CERN PS.

In order to produce the desired radiation fields at several experimental positions, the beam hits on one out of a set of dedicated targets.

Since the beam operation of the CHARM facility is on, this leads to the activation of the facility itself. This includes the activation of the targets, walls, floors and any other support structure. In order to plan the access to the facility and more important to optimize the design of this one of the kind facility is very important the correct prediction of the residual ambient dose equivalent rates.

One of the most interesting things, that makes the prediction more challenging for the CHARM facility is the fact that the facility configuration

## 6. Residual ambient dose equivalent rate measurements

---

during beam operation is different in the CHARM facility compared to the facility configuration during access. For example the irradiated targets are moved to a dedicated alcove that is closed during access. [26],[28], [62], [33], [27], [10],

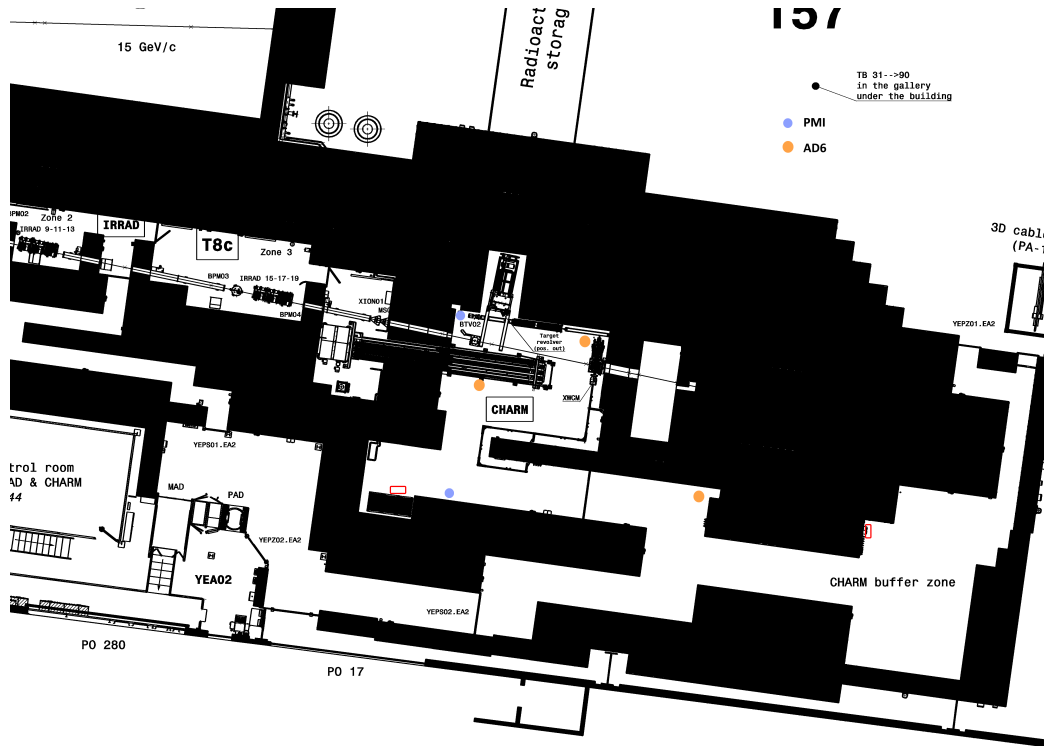
A dedicated residual ambient dose equivalent rate measurement campaign has been performed at the end of the 2015 beam period in the CHARM facility. It started from 1 hour after beam stop collecting data for 1 week. During this campaign there were installed several mobile devices and permanently installed devices collecting data.

These data are compared to predictions for the residual ambient dose equivalent rates in the CHARM facility performed with the FLUKA Monte Carlo code, coupled to the DORIAN code for the various facility configurations, as a function of the cool-down time taking the operational parameters of the CHARM facility in 2015 into account.

This includes the characteristics of the beam delivered to the CHARM facility as well as the CHARM target settings.

The figures below show the position of each mobile device inside the CHARM facility. The rest of them are the permanently installed detectors, PMI.

The detectors that are used where Geiger-Muller. A Geiger counter (Geiger-Muller tube) is a device used for the detection and measurement of all types of radiation: alpha, beta and gamma radiation. Basically it consists of a pair of electrodes surrounded by a gas. The electrodes have a high voltage across them. The gas used is usually Helium or Argon. When radiation enters the tube it can ionize the gas. The ions (and electrons) are attracted to the electrodes and an electric current is produced. A scaler counts the current pulses, and one obtains a "count" whenever radiation ionizes the gas. The apparatus consists of two parts, the tube and the (counter + power supply). The Geiger-Mueller tube is usually cylindrical, with a wire down the center. The (counter + power supply) have voltage controls and timer options. A high voltage is established across the cylinder and the wire



ITH

**Figure 6.1:** The 2 permanently installed PMI chambers in blue locations and 4 AD6 and with modems at the orange locations.

as shown in the figure. When ionizing radiation such as an alpha, beta or gamma particle enters the tube, it can ionize some of the gas molecules in the tube. From these ionized atoms, an electron is knocked out of the atom, and the remaining atom is positively charged. The high voltage in the tube produces an electric field inside the tube. The electrons that were knocked out of the atom are attracted to the positive electrode, and the positively charged ions are attracted to the negative electrode.

This produces a pulse of current in the wires connecting the electrodes, and this pulse is counted. After the pulse is counted, the charged ions become neutralized, and the Geiger counter is ready to record another pulse. In order for the Geiger counter tube to restore itself quickly to its original state after radiation has entered, a gas is added to the tube. For proper use of the Geiger

## 6. Residual ambient dose equivalent rate measurements

---

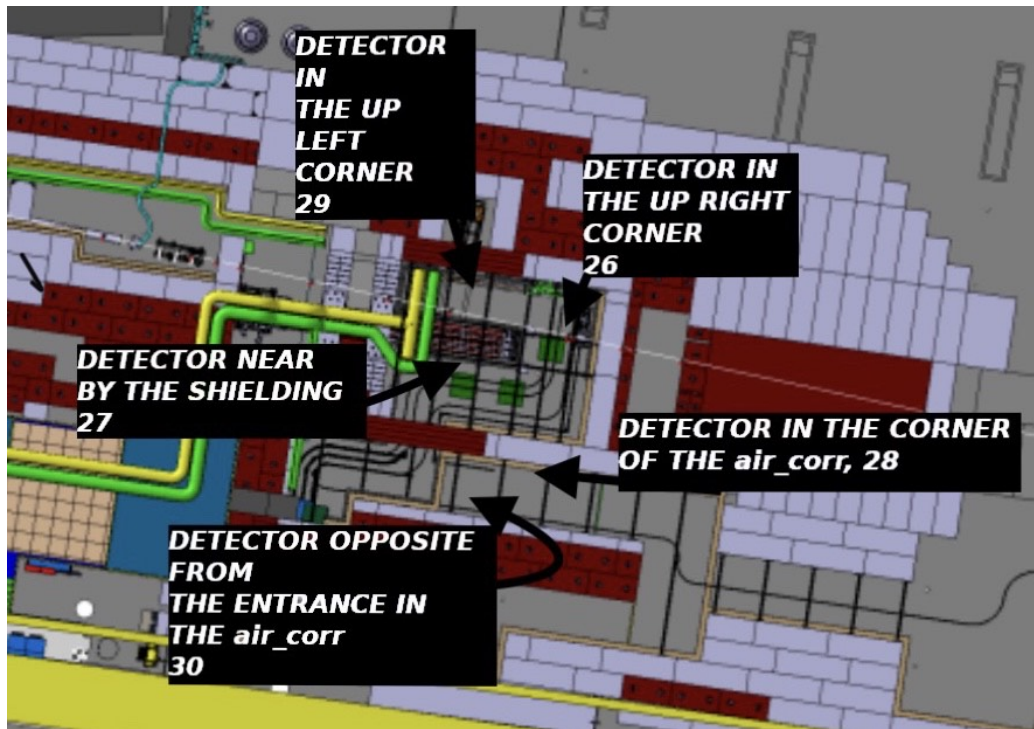


**Figure 6.2:** Map with the detectors with their names.

counter, one must have the appropriate voltage across the electrodes. If the voltage is too low, the electric field in the tube is too weak to cause a current pulse. If the voltage is too high, the tube will undergo continuous discharge, and the tube can be damaged. Usually the manufacture recommends the correct voltage to use for the tube. Larger tubes require larger voltages to produce the necessary electric fields inside the tube. In class we will do an experiment to determine the proper operating voltage. First we will place a radioactive isotope in from of the Geiger-Mueller tube. Then, we will slowly vary the voltage across the tube and measure the counting rate. In the figure I have included a graph of what we might expect to see when the voltage is increased across the tube. For low voltages, no counts are recorded. This is because the electric field is too weak for even one pulse to be recorded. As the voltage is increased, eventually one obtains a counting rate. The voltage at which the G-M tube just begins to count is called the starting potential. The counting rate quickly rises as the voltage is increased. For



**Figure 6.3:** The position of the one of the detectors inside of the facility. This is the detector 28.



**Figure 6.4:** The position of the one of the detectors inside of the facility. This is the detector 28.

our equipment, the rise is so fast, that the graph looks like potential. After the quick rise, the counting rate levels off. This range of voltages is termed the "plateau" region. Eventually, the voltage becomes too high and we have continuous discharge. The threshold voltage is the voltage where the plateau region begins. Proper operation is when the voltage is in the plateau region of the curve. For best operation, the voltage should be selected fairly close to the threshold voltage, and within the first 1/4 of the way into the plateau region. A rule we follow with the G-M tubes in our lab is the following: for the larger tubes to set the operating voltage about 75 Volts above the starting potential; for the smaller tubes to set the operating voltage about

## 6. Residual ambient dose equivalent rate measurements

---



**Figure 6.5:** The position of the one of the detectors inside of the facility. This is the detector 27.



**Figure 6.6:** The position of the one of the detectors inside of the facility. This is the detector 27.

50 volts above the starting potential.

The measurements had the form in the Figure 6.17. In order to be able to compare them, with the simulation results, there has to be a procedure picking some of them and transform the in the right csv form. So everything had to be converted in mSv and in seconds. In the next chapter in the python file there is the part, where the comparison of both of them happens.[\[40\]](#),[\[44\]](#), [\[16\]](#),[\[7\]](#), [\[26\]](#), [\[64\]](#), [\[63\]](#), [\[19\]](#) [\[60\]](#), [\[66\]](#), [\[30\]](#), [\[31\]](#),[\[29\]](#).





**Figure 6.7:** The position of the one of the detectors inside of the facility. This is the detector 26.



**Figure 6.8:** The position of the one of the detectors inside of the facility. This is the detector 27.



**Figure 6.9:** The position of the one of the detectors inside of the facility. This is the detector 26.

## 6. Residual ambient dose equivalent rate measurments

---



**Figure 6.10:** The position of the one of the detectors inside of the facility. This is the detector 27.



**Figure 6.11:** The position of the one of the detectors inside of the facility. This is the detector 26.



**Figure 6.12:** The CHARM facility.





**Figure 6.13:** The 4 movable shielding walls and the target holder inside the facility.

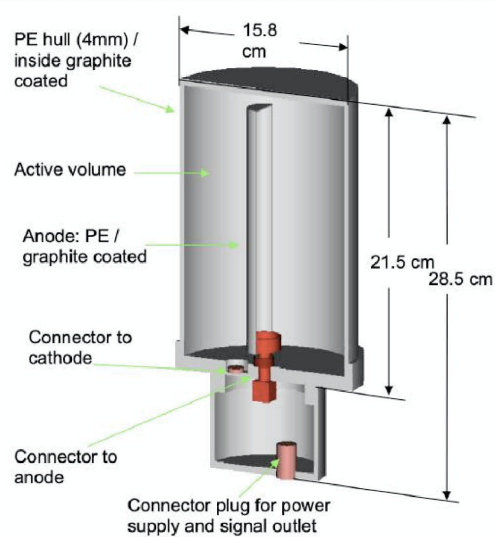


**Figure 6.14:** A PMI detector

## 6. Residual ambient dose equivalent rate measurements



Figure 6.15: An AD6 detector

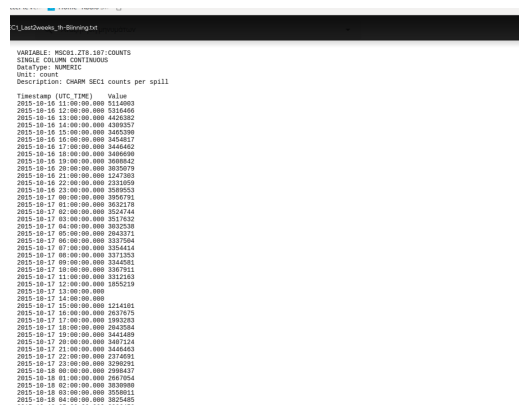


Figure 6.16: Beam intensity

# Chapter 7

## Simulation setup

The FLUKA Monte Carlo simulation package is dedicated to particle physics and is the main simulation tool, that is used to gain a better insight about the radiation environment inside the facility.

Proton beams can be defined with details and collided. By modeling and building the geometry of the CHARM facility and their surroundings, FLUKA can estimate the radiation effects. All the elements can be described accurately through the mathematical combinations of elementary shapes. However, a more detailed geometry model requires a more details description which can lead to longer CPU times when simulating and increased manpower requirements for maintenance. It is of high importance to assign appropriate materials with accurate densities and composition to the geometry volumes.

FLUKA predictions are useful to test shielding effectiveness as well as to assess radiation damage in the specific radiation environment. The FLUKA output format is specified using ‘scorings’ (predefined cards that estimate desired information during a simulation, as it shows in the figures below.) The output can be for instance, a particle flux map over a particular for example region (USRBIN). The user can specify the particle type or the group of particles to be included in the scoring. Typical physical quantities generally used in the FLUKA output are fluence and current. The former can be

## 7. Simulation setup

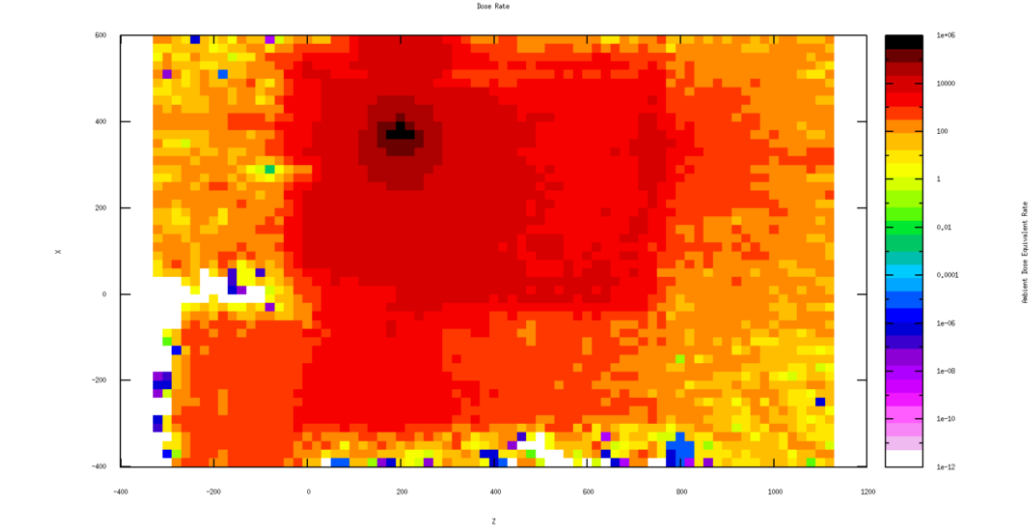


**Figure 7.1:** A figure after a run of the FLUKA simulation in the CHARM facility. This figure shows how highly irradiated is the CHARM facility after the beam. Prompt dose equivalent rate.

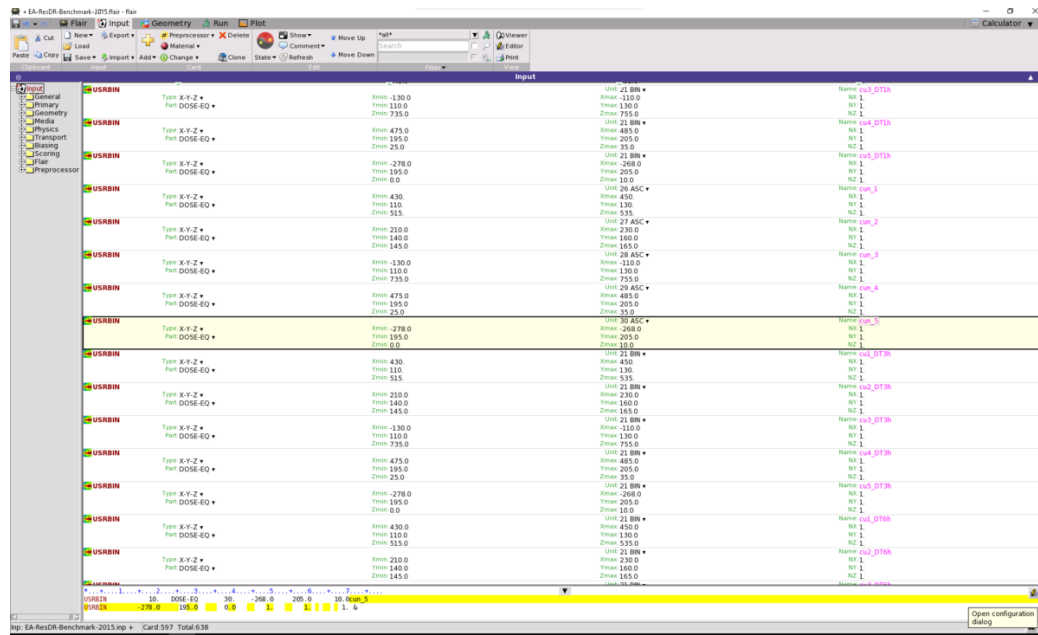


**Figure 7.2:** A screenshot in process to define the USRBINs for the CHARM facility

estimated using tracklength or boundary crossing scoring. All regional estimates (e.g., USRBIN) use the tracklength. It is calculated by adding paths  $dt/\cos\theta$  of particles crossing the infinitesimal thickness  $dt$  of the boundary with an angle  $\theta$  with respect to the normal to that surface and then dividing it by the boundary volume  $Sdt$ . Flair is used in order to built the geometry of the CHARM facility. Flair is in python and Tkinter and is an interface to facilitate the edit of input FLUKA files, the execution of code, making easier the visualization of the output files. The Figure 7.3 shows the input file with the tools and the features that are used to build the geometry, with the desirable materials, features etc.

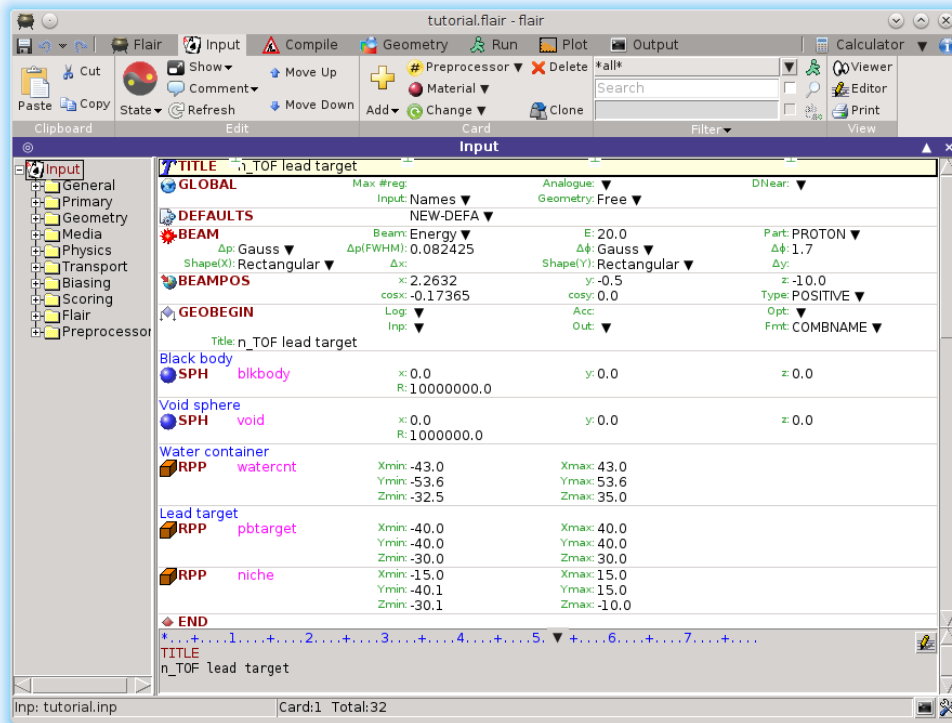


**Figure 7.3:** FLUKA Input editing with the interpreted cards

The Figure 7.4 shows the CHARM facility geometry, that has been built with the help of flair interface.

After the right corrections and set up of the geometry, with the desirable

## 7. Simulation setup

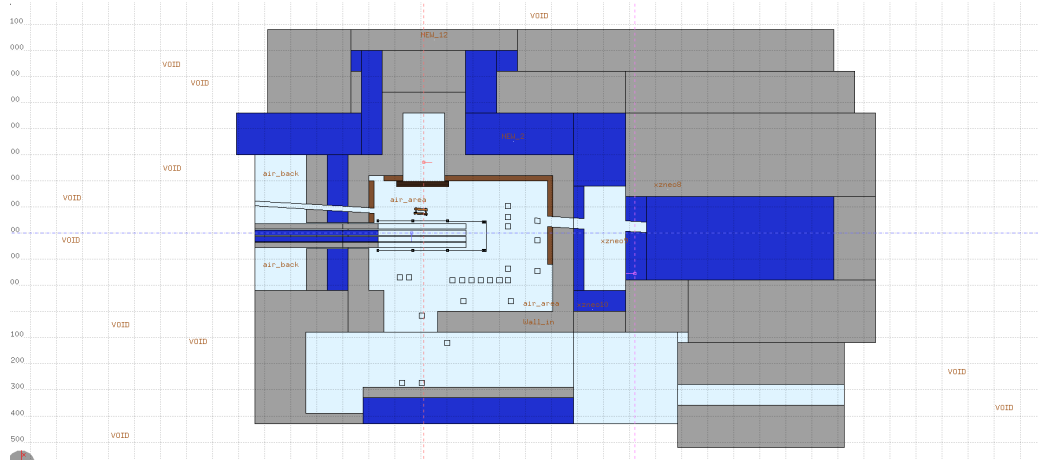


**Figure 7.4:** The geometry of CHARM facility

parameters in the input file, corresponding the closest possible with the real circumstances, Monte Carlo simulations have been performed with FLUKA and the DORIAN code. The aim was to predict the ambient dose equivalent rate levels for various operational scenarios and cool-down times. Per operational year with maximum beam intensity of  $6.610^{10} p/s$ .

In the Figure 7.5 is shown again the geometry of the whole CHARM facility, as it was in the four windows of the flair interface, during the process of constructing the simulation.

Each one of the figures below there each part of our geometry explained with its dimensions, material etc.

The Figure 7.6 shows the alcove with the importance implemented in its geometry. The alcove in z axis is 200 cm and in x axis is 20 cm.

In the figure 7.7 is the geometry both of the alcove (that is closed) and the target outside of the alcove and near by the position of the shielding.

Two of the detectors that were used, are in that area, as a result, it was considered significant to simulate that area as close as possible to the reality. The shielding walls were built with more accurate way, with plenty of choices of implementations. The wall of the alcove is separated in smaller areas of importance in order to have the most accurate results. The alcove area is from  $z=130$  cm until  $z=290$  cm and from  $x=500$  cm until  $x=790$  cm.

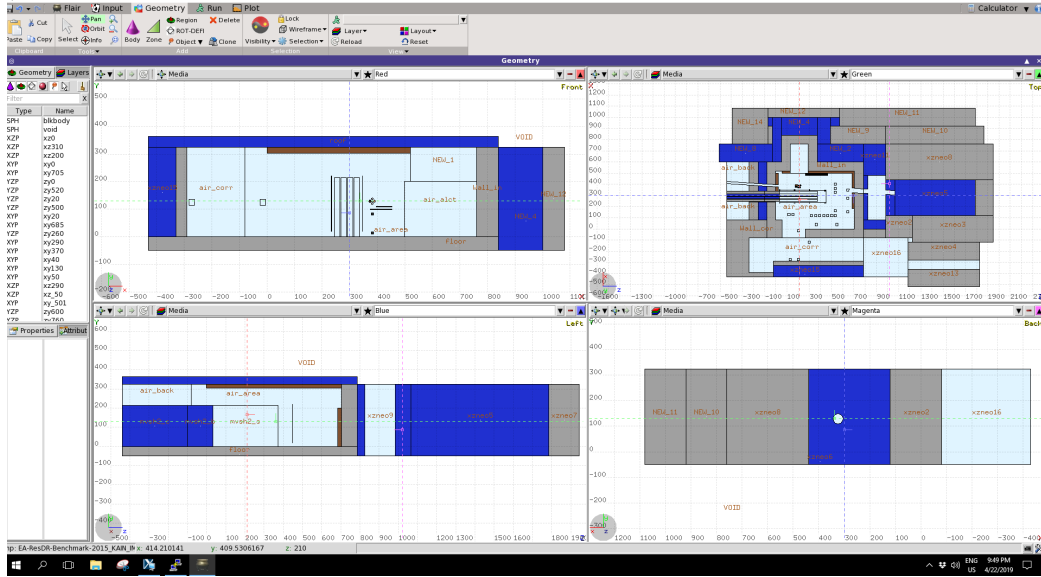


Figure 7.5: The geometry of the whole facility

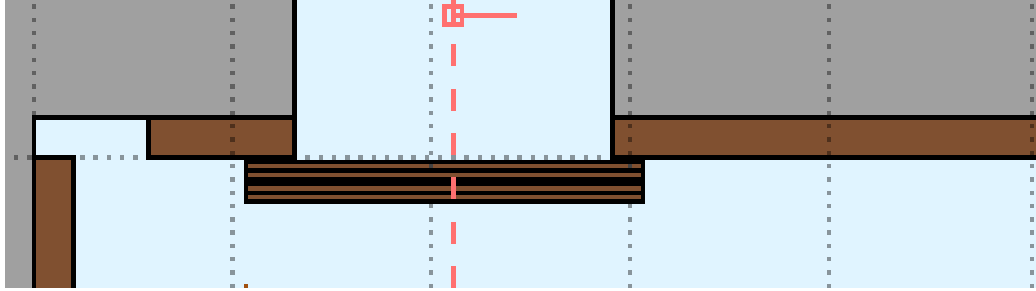
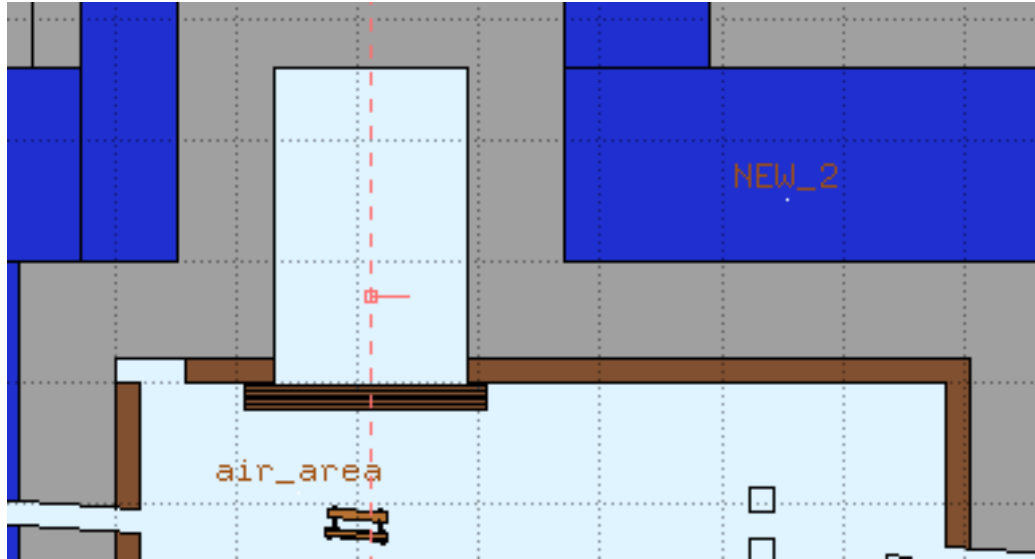


Figure 7.6: The tarsh with the importance of the closed alcove

In the Figure 7.9 are shown the four walls of the shielding walls. The areas with the grey color are made from concrete material, the blue is fonte, the brown marble and of course the rest of the area with the light blue color is air.

The Figure 7.9 shows the shielding walls are made by concrete (with the grey color) and by marble (with the blue color). The simulation was implemented with each one of the walls can be inside the facility alone or all together. Implementing the simulation of the facility that way is helping to have as much as different interfaces for various radiation concepts. The center of the wall is the  $mvsh1_b$  etc, for each wall. When the wall is inside

## 7. Simulation setup



**Figure 7.7:** The closed alcove

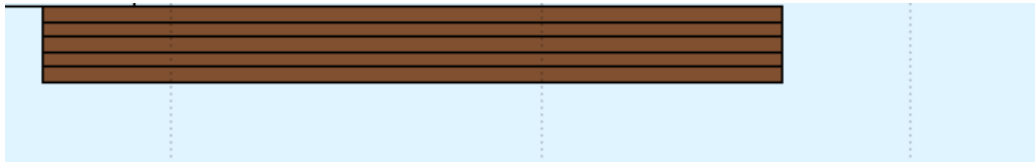


**Figure 7.8:** The importance of the tarsh again in that figure closer

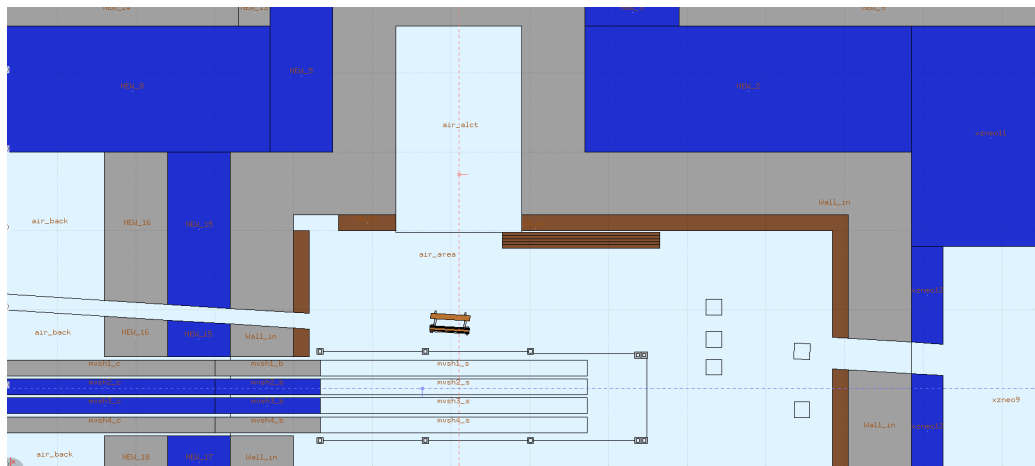


**Figure 7.9:** Part of the geometry of the CHARM facility. This figure shows the shielding, the alcove, the target and the beamline



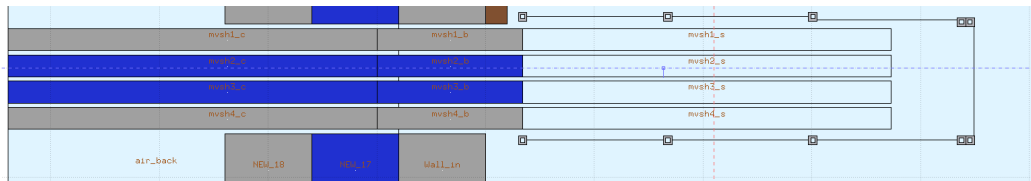


**Figure 7.10:** The geometry of the walls of the shielding.

the other side of the same wall is empty. This happened in order to have the best possible results and be as close as possible in the real circumstances.

## 7. Simulation setup

---

## Chapter 8

# Comparison of simulations and measurements

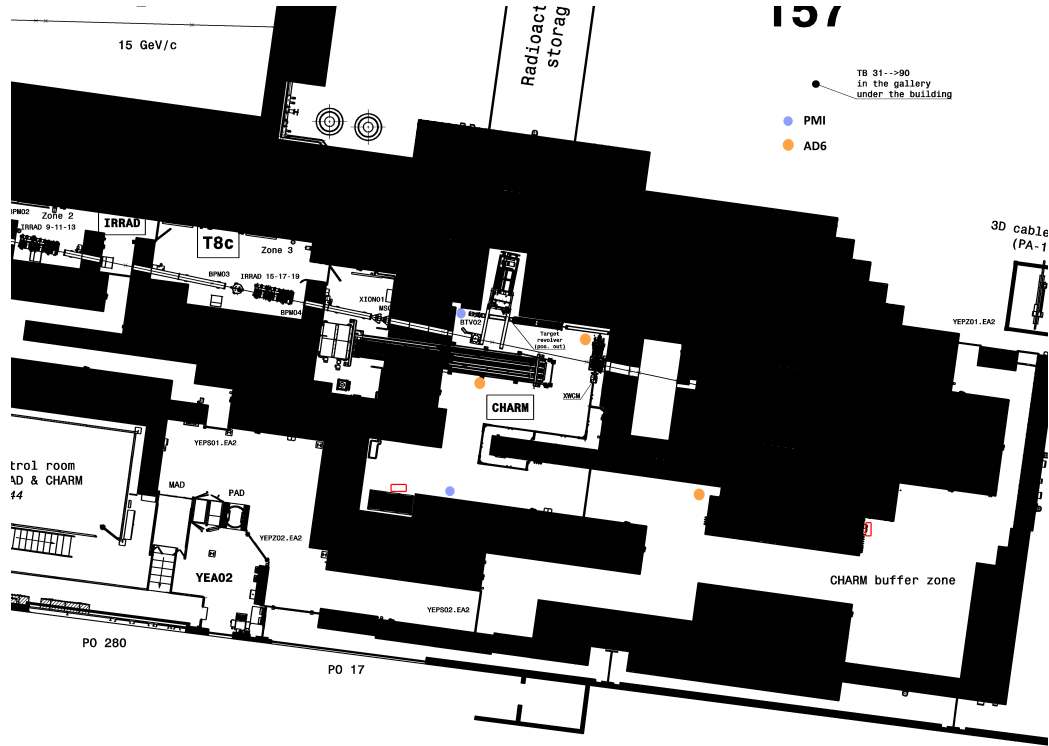
In this chapter is presented the comparison between the real measurements and the simulations that have been performed. The measurements, which were in TIMBER had to be processed and selected through excel in order to be in the right form and units of measurements for the comparison with the simulation results. In the Figure 8.1 is the layout of the facility with the detectors in their position. In the map of the Figures 8.2, there are the number of one of the detectors and their '*name*', position. The same '*name*', position is written in the description of the next Figures, which represent each one of the detectors, implementing the comparison between the measurements and the results of the simulations.

The Figure 8.3 demonstrates the comparison between the plots for the detector near by the shielding. The detector near by the shielding is a PMI detector. The agreement between these two plots is satisfactory. The measurements is the green line and the simulation is the blue line. The small thick spots in the upper part of the measurement plot, is because of the noise.

In the Figure 8.4 appears the comparison between the measurements for the detector that is positioned in the corner of the air corridor.

The agreement between these plots is very good in the most of the part.

## 8. Comparison of simulations and measurements



ITH

**Figure 8.1:** The layout of the facility with the PMI and AD6 detectors

The two plots coincide in the beginning. The difference between them, can be due to the fact that there is no importance implemented in the whole facility in the simulation until the air corridor.

In the Figure 8.5 is presented the comparison between the measurements and the simulation results about the detector that is located in the up right corner of the CHARM facility. The agreement between these two plots is optimal enough. The two plots in the most of their parts do not deviate not even for 10 per cent of each other. The success of the agreement of these two plots is because of the scoring and importance that we perform during the simulation in the area of the alcove.

In the Figure 8.6 the comparison between the measurements and the simulation results for the factor that is located in the up left corner. These two curves have minimum deviation. The good results about these two plots

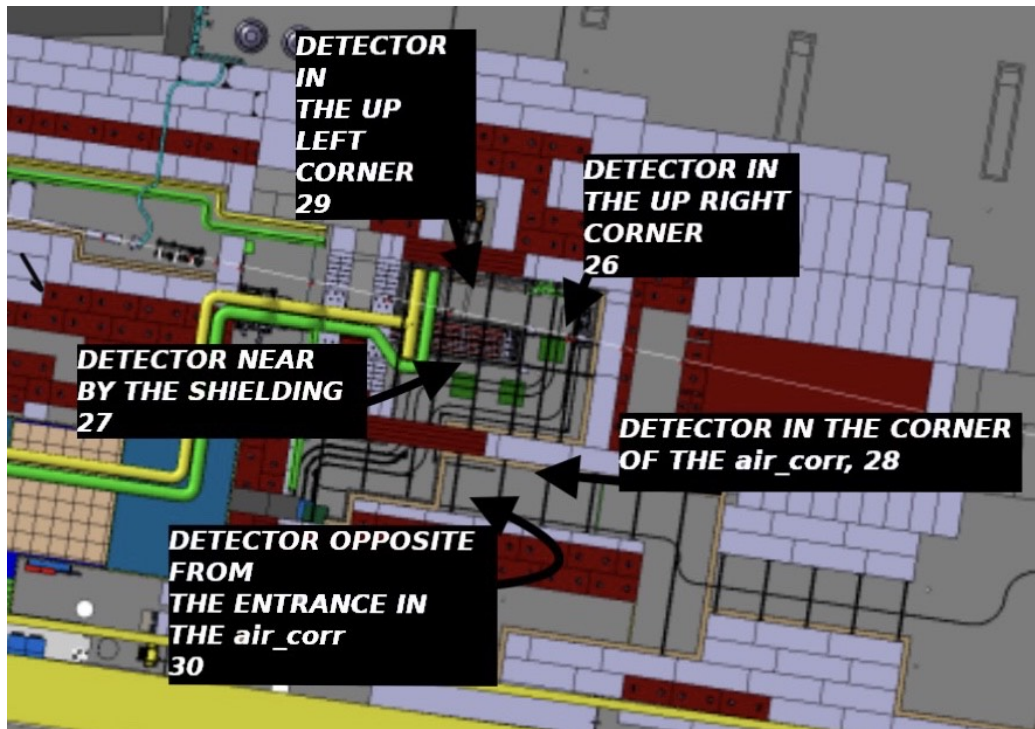


**Figure 8.2:** A closer look to the layout of the CHARM facility with the name of the detectors corresponding in the plots in this chapter.

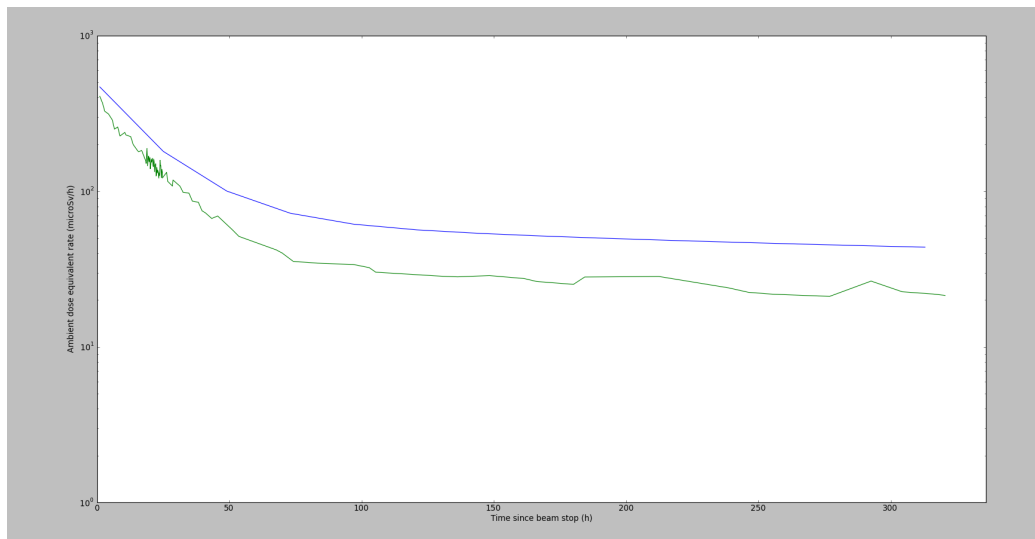


**Figure 8.3:** The Detector near by the shielding, 27. The blue line is the simulation and the green line are the measurements.

## 8. Comparison of simulations and measurements

---

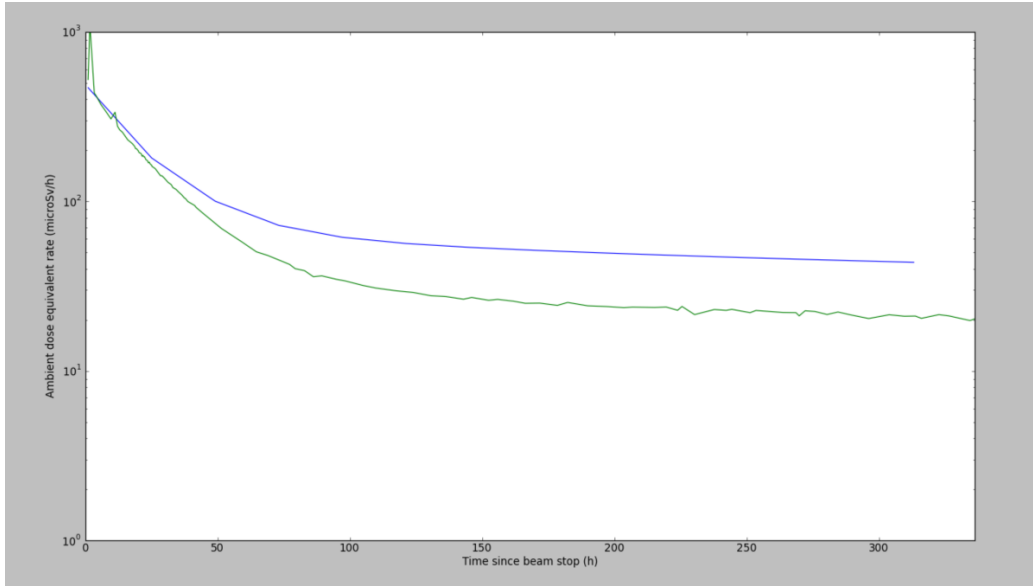


**Figure 8.4:** Detector in the corner of the air corridor, 28. The blue line is the simulation and the green line are the measurements.

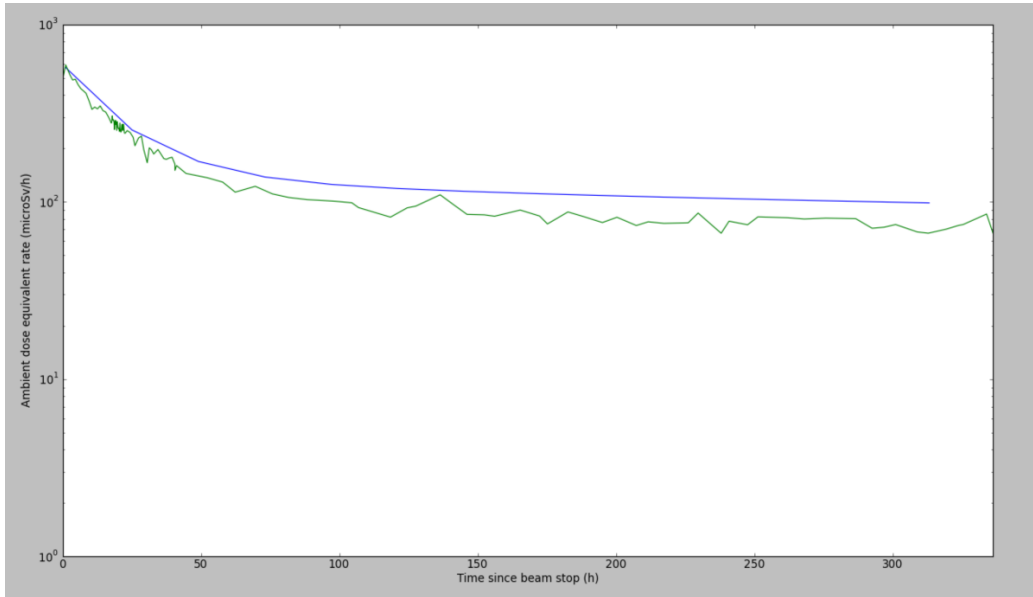


**Figure 8.5:** The detector in the up right corner, 26. The blue line is the simulation and the green line are the measurements.

are because of the scoring, importance that is performed in the simulation of the facility in the alcove.

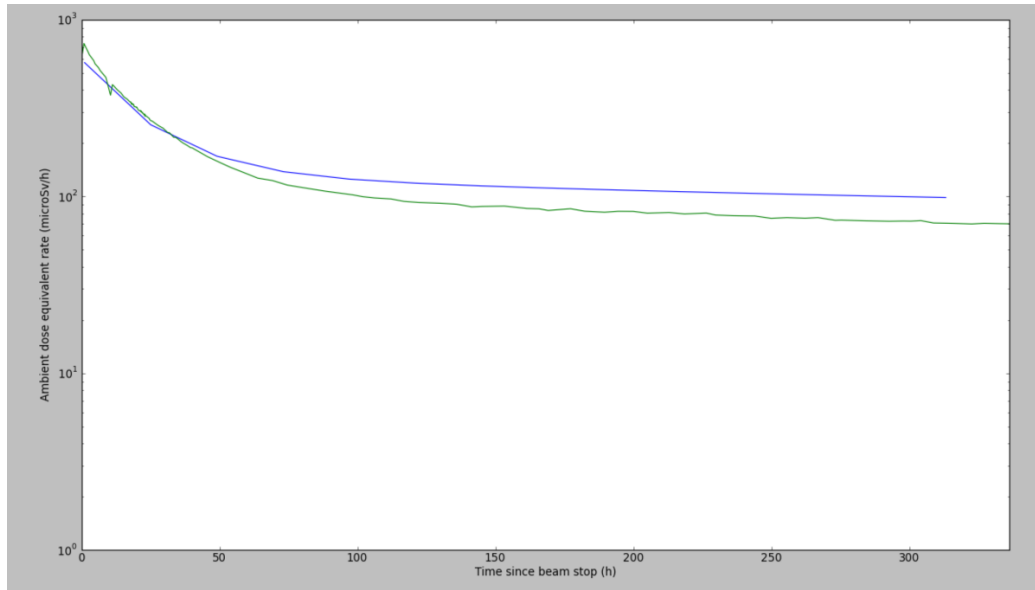


**Figure 8.6:** Detector in the up left corner, 29. The blue line is the simulation and the green line are the measurements.

The Figure 8.7 appears the comparison between the plots about the detector opposite is the entrance of the air corridor, 30. These two plots are in perfect almost 100 per cent agreement, except from the initial upper part that there is a deviation not more than 5 per cent. This comparison is the most optimal that we can have about our studies.

## 8. Comparison of simulations and measurements

---

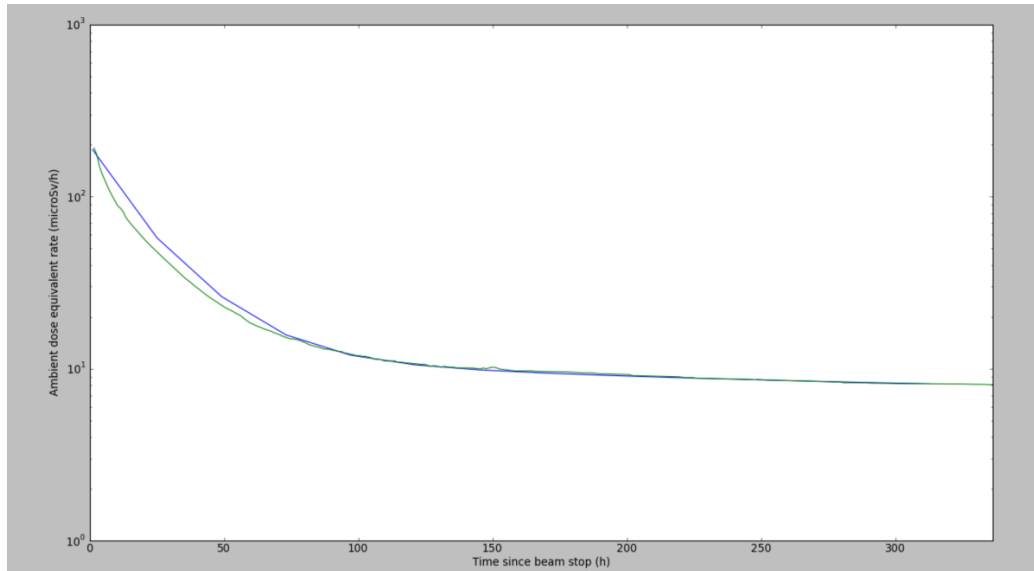


**Figure 8.7:** Detector in the opposite of the entrance of the air corridor,30. The blue line is the simulation and the green line are the measurements.



# Chapter 9

## Summary and Conclusions

The CERN High energy Accelerator Mixed field (CHARM) facility has been constructed in 2014 in the CERN East Experimental Area to study radiation effects on electronic components. It receives a primary proton beam from the CERN Proton Synchrotron at a beam momentum of  $24\text{GeV}/c$  and a maximum average beam intensity of  $6.7e10$  protons/second with a maximum pulse intensity of  $5e11$  protons/pulse and a respective pulse length of 350 ms. The beam impinges on one out of a set of dedicated targets to produce the desired radiation fields at several experimental positions. The beam operation of the CHARM facility leads to activation of the facility itself, including the targets, walls, floors and other support structures. The correct prediction of the residual ambient dose equivalent rates is important for the optimization of the design of such a facility as well as for the planning of accesses to the facility. The fact that the facility configuration during beam operation is different in the CHARM facility compared to the facility configuration during access, e.g. the irradiated targets are moved to a dedicated alcove that is closed during access, makes this prediction even more challenging for the CHARM facility. A dedicated residual ambient dose equivalent rate measurement campaign with several mobile devices as well as permanently installed devices has been performed at the end of the 2015 beam period in the CHARM facility starting from 1 hour after beam stop collecting data for

## 9. Summary and Conclusions

---

1 week. These data are compared to predictions for the residual ambient dose equivalent rates in the CHARM facility performed with the FLUKA Monte Carlo code, coupled to the DORIAN code for the various facility configurations, as a function of the cool-down time taking the operational parameters of the CHARM facility in 2015 into account. This includes the characteristics of the beam delivered to the CHARM facility as well as the CHARM target settings. After this investigation the conclusion is that the FLUKA Monte Carlo simulation is more than capable to simulate the real time conditions of a highly irradiated facility. Using FLUKA to model the CHARM facility, it is possible to calculate the radiation field at the various positions with all possible facility configurations. This normally would be very difficult and could potentially take months for actual measurements. The resulting agreement is better than a factor of  $\sim 2$ , except from the detector 28. This can be because of the biasing during the low statistics of the problem, since it is away from the source. This agreement demonstrates that FLUKA is a very suitable tool for this kind of description, that we studied in this Master thesis.

# Bibliography

- [1] <https://www.cern.ch/charm/>.
- [2] <https://www.cern.ch/r2e/>.
- [3] K. Nakamura et al (Particle Data Group) 2010 J. Phys. G: Nucl. Part. Phys. 37 075021. In: (2010).
- [4] J. Ranft A. Fasso A. Ferrari and P.R. Sala. FLUKA: a multi-particle transport code. Tech. rep. CERN-2005-10 (2005), INFN/TC-05/11, SLAC-R-773.
- [5] R.Froeschl et al. “*Radiation Protection Aspects of the Commissioning and Operation of the CHARM facility*”. In: *Presentation given at the SATIF-13 conference, Dresden, Germany, 10-12 October 2016* (2016).
- [6] T.T. Bohlen et al. “*The FLUKA Code: Developments and Challenges for High Energy and Medical Applications*”. In: *Nuclear Data Sheets 120* (2014), pp. 212–214.
- [7] F. Maekawa et al. Production of a Dosimetry Cross Section Set Up to 50 MeV, *Proc. 10th International Symposium on Reactor Dosimetry, Sep. 12-17, 1999, Osaka, Japan, p.417, American Society for Testing and Materials (2001)*.
- [8] G. Battistoni et al. “*The Application of the Monte Carlo Code FLUKA in Radiation Protection Studies for the Large Hadron Collider*”. In: *Progress in Nuclear Science and Technology, Vol.2* ().

- [9] M. Brugger et al. “*FLUKA Capabilities and CERN Applications for the Study of Radiation Damage to Electronics at High-Energy Hadron Accelerators*”. In: Presentation given at SNA MC 2010, October 17-21, 2010, Tokyo, Japan (2011), pp. 948–954.
- [10] R. Froeschl et al. *Work and Dose Planning for the PSB Injection Dumps*.
- [11] ALICE Collaboration, K. Aamodt et al. “*The ALICE experiment at the CERN LHC*”. In: *Journal of Instrumentation* 3(08):S080002 (2008).
- [12] ATLAS Collaboration, G. Aad et al. “*The ATLAS Experiment at the CERN Large Hadron Collider*”. In: *Journal of Instrumentation* 3(08):S080003 (2008).
- [13] M. Brugger. “*Radiation Damage to Electronics at the LHC*”. In: *Proceedings IPAC-2012-THPPP006* Presentation given at Conference C12-05-20.1 (2012), pp. 3734–3736.
- [14] S. Roesler C. Adorisio. Attenuation of high-energy neutrons in different shielding materials. A FLUKA benchmark for an intercomparison study. Tech. rep. CERN-DGS-2011-035-RP-TN. 2011.
- [15] CMS Collaboration, S. Chatrchyan et al. “*The CMS experiment at the CERN LHC*”. In: *Journal of Instrumentation* 3(08):S080004 (2008).
- [16] J. D. Cossairt. “*Induced radioactivity at accelerators*”. In: (). Professional Development School: Topics in Accelerator Health Physics, 31 Jan - 2 Feb 2008, Oakland, California, 2008.
- [17] Swiss Federal Council. “*Swiss Radiological Protection Ordinance (RPO)*”. In: 22 June 1994, Status as of 1 January 2014, Reference 841.501 ().
- [18] W. eterings and B. Goddard. *LOADING ASSUMPTIONS FOR BEAM DUMPS OF LINAC4 PS BOOSTER INJECTION*. Tech. rep. L4-T-EP-0001.

- [19] Evaluation of the Radiological and Economic Consequences of Decommissioning Particle Accelerators. Report Eur 19151. European Commission - Nuclear Safety and the Environment, 1999.
- [20] L. Evans and P. Bryant (editors). “*LHC Machine*”. In: *Journal of Instrumentation* 3(08):S080001 (2008).
- [21] F. Ravotti. Personal Communication.
- [22] D. Forkel-Wirth. *Zonage radiologique au CERN*.
- [23] R. Froeschl. Radiation Protection Assessment of the Proton Irradiation facility and the CHARM facility in the East Area. Tech. rep. CERN-RP-2014-008-REPORTS-TN. 2014.
- [24] R. Froeschl. *Radiation Protection Assessment of the PSB  $H^0/H^-$  Injection Dumps*. Tech. rep.
- [25] R. Froeschl. *Radiation Protection Assessment of the Titanium Option for the future PSB  $H^0/H^-$  Injection Dumps*. Tech. rep.
- [26] R. Froeschl. “*The DORIAN code for the prediction and analysis of residual dose rates due to accelerator radiation induced activation*”. In: *Proceedings of the AccApp13 Conference 2013* Brugge 5-8 August 2013 (2013).
- [27] G. Mason. “Presentation at the LIU-PSB beam review”. In: ().
- [28] L. Gatignon. Beam Properties for the East Area Irradiation Facility in the T8 Beam Line. Tech. rep. EAT8. 2013.
- [29] ALARA Review Working Group. *Final Report of the ALARA Review Working Group*. Tech. rep. Dec. 2012.
- [30] M. Huhtinen. Determination of cross-sections for assessments of air activation at LHC. Tech. rep. CERN/TIS-RP/TM/97-29. 1997.
- [31] ICRP. Human respiratory tract model for radiological protection. Tech. rep. ICRP Publication 66. Ann. ICRP 24(1-3), 1994.

- 
- [32] E. Iliopoulou et al. “*Measurements and FLUKA simulations of bismuth and aluminium activation at the CERN Shielding Benchmark Facility (CSBF)*”. In: *Nuclear Instruments and Methods in Physics Research A* 885 (2018), pp. 79–85.
- [33] E. Iliopoulou et al. Measurements and FLUKA Simulations of Bismuth and Aluminium Activation at the CSBF. Tech. rep. CERN–RP–2015–118–REPORTS–TN. 2015.
- [34] E. Iliopoulou et al. “*Measurements and FLUKA Simulations of Bismuth and Aluminum Activation at the CERN Shielding Benchmark Facility (CSBF)*”. In: *Proceedings of SATIF 13, Dresden, Germany (2016)* (2016).
- [35] K.Hanke. *PS BOOSTER DUMP UPGRADE*. Tech. rep. PBU–T–ES–0002.
- [36] Gnell F. Knoll. Radiation Detection and Measurement. John Wiley Sons, Inc., 2000.
- [37] LHCb Collaboration, A. Augusto Alves et al. “*The LHCb Detector at the LHC*”. In: *Journal of Instrumentation* 3(08):S080005 (2008).
- [38] D. Forkel-Wirth M. Brugger and S.Roesler. *SUMMARY OF INDIVIDUAL AND COLLECTIVE DOSES FOR INTERVENTIONS AT THE LHC BETATRON CLEANING INSERTION (IR7)*. Tech. rep. CERN–SC–2005–093–RP–TN.
- [39] S. Roesler M. Brugger D. Forkel-Wirth and P. Vojtyla. Effective Dose to the Public from Air Releases at LHC Point 7. Tech. rep. CERN–SC–2004–064–RP–TN.
- [40] M.Lazzaroni. Personal Communication.
- [41] Alessio Mereghetti. “*Shielding Data for 100-250 MeV Proton Accelerators: Double Differential Neutron Distributions and Attenuation in thick concrete, iron and concrete/iron shields*”. Master Thesis. Politecnico di Milano, 2007.

- [42] W. E. Meyerhof. Elements of Nuclear Physics. New York: McGraw-Hill, 1967.
- [43] K. Tanaka N. Nakao Y. Uwamino. “*Measurement of neutrons generated by 345MeV/u U-238 beam at RIKEN RIBF*”. In: *Proceedings of IPAC2014, Dresden, Germany* (2014).
- [44] N.Nakao et al. “*Measurement and calculation of high-energy neutron spectra behind shielding at the CERF 120 GeV/c hadron beam facility*”. In: *Nucl.Instr.Meth.B* Volume 266 (2008), pp. 93–106.
- [45] N. Nakao. Personal Communication. 2017.
- [46] H. W. Patterson and R. H. Thomas. Accelerator Health Physics. New York: Academic Press, 1973.
- [47] LINAC4 Project. Loading Assumptions for beam dumps of Linac4 PS Booster Injection. Tech. rep. L4-T-EP-0001 rev 3.2. 2014.
- [48] R. Froeschl, M. Magistris, F. Leite Pereira, C. Theis. Computation of radioactivity in particle accelerators and propagation of uncertainties with the JEREMY code. Tech. rep. Technical Report EDMS 1406467, 2014.
- [49] N. Walter R. Froeschl F.P. La Torre. The ActiWiz material composition catalogue. Tech. rep. CERN-RP-2012-002-REPORTS-TN.
- [50] P. Vojtyla R. Froeschl. Radiological Hazard Assessment of the Future PSB Beam Dump. Tech. rep. CERN-RP-2012-094-REPORTS-TN. 2012.
- [51] S. Roesler R. Froeschl M. Brugger. The CERN High Energy Accelerator Mixed Field (CHARM) facility in the CERN PS East Experimental Area. Tech. rep. Presentation given at the SATIF 12, on 28/04/2014. 2014.
- [52] R.Foeschl. *Radiation Protection Assessment of the Titanium Option for the future PSB H0 H- Injection dumps*. Tech. rep. CERN-RP-2014-007-REPORTS-TN. 2014.

- 
- [53] M.Caloz R.Foeschl. Comparison of Internal and External Exposure from Activated Air in various facilities at the Meyrin site. Tech. rep. CERN-RP-2014-007-REPORTS-TN. 2014.
- [54] M.Caloz R.Foeschl. *First Air Activation Assessment for the PS Booster after Linac4 Connection with the new Main Dump and the Future H0/H- Injection Dumps*. Tech. rep. CERN-RP-2014-053-REPORTS-TN. 2014.
- [55] R.Froeschl. *Assessment for operation of the EA Irradiation Facilities without ventilation system*. Tech. rep. Presentation given at the PS EAIRRAD working meeting on 20/05/2014. 2014.
- [56] P.Vojtyla R.Froeschl. *Air activation and releases of radioactive substances from the AD target area to the environment*. Tech. rep. CERN-RP-2013-003-REPORTS-TN. 2014.
- [57] G.R. Stevenson R.H. Thomas. “*Radiation Safety Aspects of the Operation of Proton Accelerators*”. In: *IAEA Technical Report Series No. 282, Vienna* (1988), Ch 4, Radiation Shielding, 223.
- [58] Radiation protection for particle accelerator facilities: recommendations of the National Council on Radiation Protection and Measurements. NCRP Reports 144. Bethesda, MD: NCRP, 2005.
- [59] Joao Pedro Saraiva. “*Radiological Characterization of TFA metallic tubes from CERN Accelerator Complex*”. Master Thesis. University of Coimbra, Portugal, 2012.
- [60] J. K. Shultis and R. E. Faw. Fundamentals of nuclear science and engineering. Abingdon: Dekker, 2002.
- [61] A.H. Sullivan. A Guide to Radiation and Radioactivity Levels near High Energy Particle Accelerators. Ashford, Kent, TN23 1JW: Nuclear Technology Publishing, 1992.



- [62] K. Tesch. “*A Simple Estimation of the Lateral Shielding for Proton Accelerators in the Energy Range 50-1000 MeV*”. In: *Radiat. Prot. Dosim*, 11(3) (1985), pp. 165–172.
- [63] P. Vojtyla. “*Calculation of the external effective dose from a radioactive plume by using Monte Carlo dose kernel integration*”. In: *Applied Modeling and Computations in Nuclear Science*. T.M., Pomme, S., Jerome, S.M. and Strom, D.J. Eds. A.C.S. Symposium Series 945 (Washington, DC: American Chemical Society) (2006), pp 104–114.
- [64] P. Vojtyla. Models for environmental impact assessments of releases of radioactive substances from CERN facilities. Tech. rep. CERN–SC–2005–005–IE.
- [65] Nick Walter. “*Development of an In-Situ Radiological Classification Technique for Material from CERN’s Accelerator Facilities*”. PhD Thesis. Technischen Universitat Munchen, 2015.
- [66] W. Weterings. *BI.BSW CHICANE MAGNETS for PSB injection*. Tech. rep. PBU–MKBSW–ES–0001.
- [67] G. P. Yost et al. “*Review of particle properties*”. In: *Physics Letters B* 204 (1988).

